EXPERIMENTS ON THE INTERNAL INTERMITTENCY IN TURBULENT FLOW

by

Albert Yi-shuong Kuo

A dissertation submitted to The Johns Hopkins University in conformity with the requirements for the degree of Doctor of Philosophy.

The Johns Hopkins University
Baltimore, Maryland
1970

ABSTRACT

Spatial "intermittency" in the velocity field fine-structure of fully turbulent flow regions was first observed by Batchelor and Townsend[1] in 1949. This phenomenon is studied further here, in particular in grid-generated, nearly isotropic turbulence and on the axis of a round jet. The "small eddies" concentrate in random domains occupying only a fairly small fraction of the fluid volume. Appropriately filtered hot-wire anemometer signals appear intermittent as the turbulent patterns are convected past the hot-wire by the mean flow. Measurements show the decrease in fine-structure volume as Reynolds number increases or as the size of the eddies studied decreases. The average linear dimension of these fine-structure regions turns out to be large compared with the sizes of the eddies with which they are active. This relative dimension decreases with increasing Reynolds number or with decreasing eddy size.

To study more about the statistical geometry of the fine-structure regions, two-probe coincidence functions for the occurrence of fine-structure were measured as functions of the relative positions of the two probes. Three possible categories of geometry were considered: (a) "blobs," (b) "rods," (c) "slabs," depending on whether the three mean orthogonal dimensions of the domains (a) are all of the same order, (b) show one an order larger than the other two, (c) show one an order smaller than the other two.

Highly idealized paradigms for these three categories were computed analytically. The coincidence functions were computed for the cases of (a) spheres or (b) circular cylinders or (c) plane slabs, each field having random sizes distributed randomly in space with a homogeneous and isotropic statistical distribution. Comparison of the actual turbulence data with these three paradigms suggests that the fine-structure regions are more likely to have random "rod-like" geometry than either of the other two.

The flatness factors and probability distributions of the first derivative, the second derivative, and band-pass signals of the velocity fluctuations were also measured in grid-generated turbulence and on the axes of round jets. The turbulence Reynolds numbers R_λ ranged from 12 to 830. The flatness factors of the velocity derivatives are sensitive to the high cut-off frequency of the electronic circuits. With high cut-off frequency set at Kolmogorov-scale frequency, the flatness factors of the first derivative vary with $R_\lambda^{0.2}$ for $R_\lambda < 200$, with $R_\lambda^{0.62}$ for $R_\lambda > 500$, and with a transition between these two ranges. Those of the second derivative vary with $R_\lambda^{0.25}$ for $R_\lambda < 100$ and with $R_\lambda^{0.75}$ for $R_\lambda > 300$. No sign of approaching asymptotic values was observed at R_λ up to order of one thousand; this is contrary to the conjecture of absolute constant values at high Reynolds number made by Batchelor and Townsend.[1,9]

The probability distributions of velocity fluctuations and large-scale signals are nearly normal, while the small-scale signals

are not. The deviation from normality increases as we examine smaller and smaller scales extracted from the complete signal by proper filtering. The flatness factor of the filtered band-pass signal of the velocity fluctuation increases with increasing frequency, while that of Gaussian noise is approximately 3.0 irrespective of the frequency. The flatness factor of a band-pass signal is dominated by the filter's smoothing (or averaging) effect if the filter bandwidth is very narrow. In the limit of infinitely narrow bandwidth, the application of the central limit theorem suggests that the band-pass signal is normal.

The square of the signal associated with large wave numbers may be approximated by a log-normal probability distribution except for very small and very large amplitude ranges.

ERRATA

(for thesis of A. Kuo)

page

45 Line 7 from bottom: replace "connected" by "convected".

56 Line 8: replace "that" by "than".

62 Line 14 should read "... in Figures 28, 29, and 30; ..."

93 The first line should read "of magnitude of the reciprocal of r.m.s. turbulent ..."

98 Line 2 from bottom: replace (f_m = 6 kHz) by (f_m = 6.3 kHz).

159 Add reference 36 at the bottom

36. Rice, S. O. "Mathematical Analysis of Random Noise." Bell System Tech. Jour. Vols. 23 and 24, 1944 and 1945. (Also in "Selected Papers on Noise and Stochastic Processes." edited by Nelson Wax. New York: Dover Pub. Inc., p. 133, 1954)

ACKNOWLEDGMENTS

I would like to express my indebtedness and gratitude to Dr. Stanley Corrsin, who suggested this subject and under whose guidance this investigation was carried out. I would also like to express my gratitude to Dr. O. M. Phillips for his critical review of this paper.

Thanks are due many of my colleagues, in particular, to W. George for his help in the laboratory during the early stage of this experiment, to J.-P. Cavelle and M. Cuneo for their help in numerical computations, to O. Guillon for assembling the electronic circuits, and to V. G. Harris, D. J. Shlien and others for valuable discussions and suggestions.

Also worthy of special mention are Dr. C. M. Sheih, of Penn State University, for his valuable discussions and information, and Mr. B. Neilson, of the Geography Department, the Johns Hopkins University, for his skill in preparing the final figures.

I also want to thank Mary Thuma and Jane Zee for typing the final manuscript and drafts.

This work was sponsored by the Engineering Divison of the National Science Foundation, with an assist from the Fluid Dynamics Branch of the Office of Naval Research. Their support is much appreciated.

Finally, I menion my wife, Shiow-chyn, for her patience and devotion during the years of my graduate studies.

TABLE OF CONTENTS

TABLE OF ILLUSTRATIONS

LIST OF SYMBOLS

$E(k)$	three-dimensional energy spectrum
$E_{11}(k_1)$	one-dimensional energy spectrum
$E_{\varepsilon\varepsilon}(k)$	spectrum of energy dissipation
F	flatness factor
f_c	filter cut-off frequency, -3db point
f_m	midband frequency of band-pass filter
$f^* \equiv \frac{U}{2\pi\eta}$	Kolmogorov-scale frequency
Δf	filter bandwidth between -3db points
$I(t)$	on-off signal at the output of intermittency circuit
k	wave-number magnitude
k_1	wave-number component in mean flow direction
$\mathcal{L}$	integral scale
ℓ_w	length of hot-wire
M	grid mesh size
n	average number of fine-structure regions detected by a probe per unit time

n_2	average number of fine-structure regions detected simultaneously by two probes per unit time
$P(e)$	probability density function
$\underline{r}(r_1, r_2, r_3)$	vector separation between two probes
$R_f(r_1, r_2, r_3, \tau)$	space-time correlation of the fine-structure signal
$R_I(r_1, r_2, r_3, \tau)$	space-time correlation of the signal $I(t)$
$R_\lambda \equiv \frac{u'\lambda}{\nu}$	Reynolds number based on Taylor microscale
S_f	Length scale of fine-structure signal chosen for geometric studies
S_k	skewness factor
t	time
U	mean flow velocity
u, v, w	fluctuating velocity components
u', v', w'	r.m.s. of u, v, w
W	linear dimension of fine-structure region
x, y, z	cartesian coordinates
ε	turbulent energy dissipation rate

η Kolmogorov microscale

λ Taylor microscale

γ intermittency factor

γ_2 fraction of time two probes register fine-structure simultaneously

ν kinematic viscosity

τ delay time

$\langle\ \rangle$ ensemble average

$\overline{}$ time average

I. INTRODUCTION

It has been suggested for some twenty years that the "fine-structure" of the random velocity field in a fully developed, high Reynolds number turbulent flow tends to be spatially localized. Since the viscous dissipation of turbulent kinetic energy occurs primarily in the fine-structure (small eddies), this implies that the regions in which most of the dissipation occurs may be scattered through the fluid in a rather "spotty" way. This spottiness of the fine-structure was first inferred by Batchelor and Townsend[1] from the intermittent occurrence, between very high and very low amplitude, of high frequency contributions in hot-wire anemometer signals.* They used essentially a high-pass filter (the effect of successive differentiations) to extract the fine-scale signals from hot-wires placed in grid-generated turbulent flows and in turbulent wakes behind cylinders. A quantitative measure of the intermittency was chosen as the amount by which the "flatness factor" of a variable $e(t)$ observed to be intermittent,

$$F \equiv \frac{\overline{e^4(t)}}{\left\{\overline{e^2(t)}\right\}^2} \tag{1.1}$$

exceeds the values 3.0, which is appropriate to a variable with normal ("Gaussian") probability density. They found that the flatness factors of velocity derivatives were greater than 3.0, and

---

*see discussion in Appendix A1.

increased with both the order of derivative and the Reynolds number of the turbulence. They therefore suggested that the energy associated with the fine-scale components is distributed very unevenly in space, and roughly confined to regions which become smaller as the eddy sizes decrease. Specifically, they said the following:

> "Thus the process of subdivision of the fluid into regions of strong and of weak activation will occur in a stepwise manner as the wave-number — or the order of the derivative of the velocity — increases. The various regions in which wave-numbers of order k_n are activated will all lie within regions in which wave-numbers k_{n-1} of an order of magnitude smaller than k_n are activated, and these in turn are enclosed by regions in which even smaller wave-numbers are activated."

They also suggested that the linear dimensions of these active regions are large compared with the eddy sizes with which they are active and that their mean separation is comparable with the integral scale of the turbulence.

Sanborn[2] showed that the fine-scale components of the turbulence in the fully turbulent part of a boundary layer also tend to be spotty. He used a band-pass filter to extract the fine-scale signals, the oscillograms of which appeared intermittent. Kennedy and Corrsin[3] also observed intermittency in the band-pass signals of a fully turbulent free shear layer. The flatness factors measured by Sandborn and Kennedy and Corrsin agreed qualitatively with those of Batchelor and Townsend. Pond and Stewart[4] measured the flatness factor of the first derivatives of the velocity fluctuations in the wind blowing over water and obtained a value as high as 20. Recently, Sheih[5] also observed that the first derivative

of the velocity fluctuations is intermittent in atmospheric turbulence. Stegen and Gibson[6] observed intermittency in the first derivatives of both velocity and temperature fluctuations in the wind over the ocean. The flatness factors of the derivatives measured by Sheih and Stegen and Gibson also were much larger than 3.0.

It was remarked by Kennedy and Corrsin[3] that although an intermittent variable is likely to have a high flatness factor, a high flatness factor does not necessarily imply intermittency. Therefore, the flatness factor can at most indicate the degree of intermittency of a variable already known to be intermittent by other observations. A more direct measurement is the "intermittency factor," γ , defined as the fraction of time the detection probe sees the variable at high amplitude state.* The intermittency factor of a variable can be inferred from the flatness factor only if its probability distributions during both states are known.

A fundamental theory of the fine-structure of turbulence is Kolmogorov's similarity hypothesis.[8,9] This theory postulates that, irrespective of the nature of the large-scale of turbulence, the small-scale components of the motion are isotropic, and have statistical properties which are uniquely determined by the two parameters ν , the kinematic viscosity, and $\langle \varepsilon \rangle$, the average energy dissipation rate.

Almost immediately after the proposal of this similarity hypothesis, Landau[10] raised doubt about its validity because of the

---

*First defined by Townsend[7] in his study of the boundary between a turbulent wake and a (potential flow) "free stream."

possible presence of large fluctuations in the instantaneous energy dissipation rate. However, no attention was paid to this doubt for several years. After the experimental observations of the strong localization of the fine-scale components, some analytical models designed to include this feature have been proposed. Up to now no experiment has been performed to evaluate them directly. Even indirect tests of these models are so rare that hardly any conclusion can yet be drawn about them.

Townsend[11] suggested that the smallest scale components (smaller than Kolmogorov microscale) arise from perturbations of vorticity superimposed on the main turbulent vorticity field. Under the action of the distortion due to the main vorticity field, perturbations are concentrated into lines or sheets of vorticity. These presumably reach an equilibrium condition in which the gain of energy from distortion is balanced by viscous diffusion and dissipation. He computed the spectra produced by random distributions of vortex "sheets" and by random distributions of vortex "lines." Better agreement with experiment was obtained from his vortex sheet model. Batchelor[12] raised some doubts about this Townsend's model after doing a similar analysis on turbulent mixing of scalar fields with very large Prandtl (or Schmidt) number.

In an attempt to modify the original Kolmogorov's similarity hypothesis, Oboukhov[13] and Kolmogorov[14] introduced the concept of "pure ensemble." Applied to the "structure function" of velocity fluctuations, i.e.,

$$\langle (\Delta u)^2 \rangle \equiv \langle [u(x+r, y, z, t) - u(x, y, z, t)]^2 \rangle$$

their similarity hypothesis for a pure ensemble states that if $\eta \ll r \ll \mathcal{L}$, then

$$\langle (\Delta u)^2 \rangle_{\tilde{\varepsilon}_r} = c\, \tilde{\varepsilon}_r^{2/3}\, r^{2/3} \tag{1.2}$$

where η is the Kolmogorov microscale, $\mathcal{L}$ is the integral scale, c is a universal constant, $\tilde{\varepsilon}_r$ is the average energy dissipation rate over a volume with linear dimension r, and $\langle (\Delta u)^2 \rangle_{\tilde{\varepsilon}_r}$ is the "pure ensemble" average on those occasions at which $\tilde{\varepsilon}_r$ takes a certain given value. In the sense of ordinary ensemble average, Equation (1.2) gives

$$\langle (\Delta u)^2 \rangle = c \langle \tilde{\varepsilon}_r^{2/3} \rangle\, r^{2/3} \tag{1.3}$$

In order to relate $\langle \tilde{\varepsilon}_r^{2/3} \rangle$ to $\langle \tilde{\varepsilon}_r \rangle$ or $\langle \varepsilon \rangle$, Kolmogorov assumed that the logarithm of $\tilde{\varepsilon}_r$ had a normal distribution with variance σ_r^2 given by

$$\sigma_r^2 = A + \mu \ln \mathcal{L}/r \tag{1.4}$$

where A depends on the macrostructure of the flow and μ is a universal constant. He thus derived a modified expression for the structure function as

$$\langle (\Delta u(r))^2 \rangle = A' \langle \varepsilon \rangle^{2/3} r^{2/3} \left(\frac{\ell}{r} \right)^{-\mu/9} \qquad (1.5)$$

He also derived a modified expression for the skewness factor

$$S_k(r) \equiv \frac{\langle (\Delta u)^3 \rangle}{\langle (\Delta u)^2 \rangle^{3/2}} = S_0 \left(\ell/r \right)^{\mu/6} \qquad (1.6)$$

A' and S_0 are constants depending on the macrostructure of the flow.

Novikov[15] used this concept of pure ensemble, in a somewhat different manner, to derive an energy spectrum shape. He concluded that the "five-thirds" law

$$E(k) \sim \langle \varepsilon \rangle^{2/3} k^{-5/3} \qquad (1.7)$$

remains valid for inertial subrange, but found no universal asymptotic behavior for higher wave-number ranges, unless a power-law behavior is assumed for the spectrum in pure ensemble.

Novikov and Stewart[16] proposed a model in which they divided a volume successively into numbers of smaller volumes. The turbulent energy dissipation was then assumed to be concentrated in a few of these small volumes. From this they predicted that the spectrum of energy dissipation can be described by a power-law with exponent lying between 0 and -1, for the wave number range

$$1/L_0 \leq k \ll 1/\ell_0$$

where L_o is the size of regions within which the conditions of local uniformity and isotropy hold, and l_o is the scale below which the viscosity is important. They claimed that l_o is smaller than the Kolmogorov microscale, and the power-law behavior of the energy dissipation spectrum can be applied in a wave-number range wider than the ordinary inertial subrange.

With Oboukhov's and Kolmogorov's modified similarity hypothesis and the assumption of a log-normal distribution for $\tilde{\varepsilon}_r$, Yaglom[17] obtained the spectra of the turbulent energy and energy dissipation in the inertial subrange as

$$E(k) = c_1 \langle \varepsilon \rangle^{2/3} k^{-5/3} (\mathcal{L} k)^{-\mu/9} \tag{1.8}$$

$$E_{\varepsilon\varepsilon}(k) = c_2 \langle \varepsilon \rangle^2 \mathcal{L} (\mathcal{L} k)^{-1+\mu} \tag{1.9}$$

where c_1 and c_2 are constants depending on the macrostructure of the flow. He estimated the universal constant μ to be 0.4 by comparing Equation (1.9) with the spectra of $\left(\frac{\partial w}{\partial t}\right)^2$ measured by Gurvich and Zubkovskii[18] (in the surface layer of the atmosphere) and of $\left(\frac{\partial u}{\partial t}\right)^2$ measured by Pond and Stewart.[4] Thus, he reached the conclusion that the large fluctuations of dissipation decreases the exponent in the "five-thirds" law by only 0.04, a magnitude which is hardly verifiable experimentally. It should be noted that the mention of energy dissipation in the inertial subrange seems like a paradox. In reality, it is not a paradox, since

the viscous energy dissipation is not zero even though the viscous force is negligibly small in comparison with the inertial force in the inertial subrange.

Using the idea of successive division of volume, Gurvich and Yaglom[19] have attempted to devise a more basic derivation of the log-normal law, by means of a mathematical description for the consequence of the cascade process of sequential breakdown of turbulent eddies. They assumed that the probability distribution for the ratio of typical value of turbulent fluctuations averaged over a small volume to those averaged over a surrounding larger volume was identical and mutually independent for different stages of volume subdivision, provided that the length scales of both volumes were much smaller than the integral scale and much larger than the Kolmogorov microscale. They reached the conclusion that any non-negative quantity governed by fine-scale components has a log-normal distribution with variance σ^2 given by

$$\sigma^2 = A + \mu \ln \mathcal{L}/\eta \qquad (1.10)$$

where A is a constant depending on the macrostructure of the flow and μ is a universal constant.

Corrsin[20] devised a very explicit model, with energy dissipation localized in randomly distributed thin sheets (or slabs). He assumed slab thickness on the order of Kolmogorov microscale and spacing on the order of the integral scale. His model predicts that the flatness factor of the first derivative of velocity fluctu-

ations increases with $R_\lambda^{3/2}$. Tennekes[21] modified this idea by suggesting a model of randomly distributed "vortex tubes," with diameter on the order of Kolmogorov microscale and spacing on the order of Taylor microscale λ . This predicts that the flatness factor increases linearly with R_λ .

The present investigation is experimental, and consists of two parts. The first is an attempt at unequivocal establishment of the phenomenon of fine-scale localization. Assuming the success of the first, the second is an attempt at preliminary categorizing the random geometry of these small regions in which the fine-scale structure is active. A knowledge of this statistical geometry, hopefully, will eventually help the understanding of the physical process of turbulent energy transfer across the wave-number spectrum, from spatially more evenly distributed large scales to unevenly distributed fine scales.

II. EXPERIMENTAL EQUIPMENT AND PROCEDURES

2.1 Aerodynamic Facilities

(1) Grid-generated Turbulence (R_λ = 12.6, 21.8)

The wind tunnel used to generate these two flow fields is that used by Bennett.[22] It has a 12 by 18 inch test section with a closed return. The grids are both of solidity about 0.34 with mesh sizes M = 1/6 and 1/2 inches. The 1/6 inch grid is of round wire, square mesh, single-plane construction. The 1/2 inch grid is of square rod, square mesh, bi-plane construction. Measurements were made at $\frac{x}{M}$ = 42 and mean speed U = 20.6 ft/sec. Reynolds numbers R_λ and Kolmogorove-scale frequencies f^* were evaluated from the turbulent energy decay rates and turbulent intensities measured by Bennett.

(2) Grid-generated Turbulence Strained by Slight Contraction ($R_\lambda = 39 \sim 150$)

The wind tunnel is that used by Comte-Bellot and Corrsin.[23] It has a closed circuit and a test section 32 feet long, 3 x 4 feet in cross section. The grids used are of square rod, square mesh, bi-plane construction. The mesh sizes are 1, 2 and 4 inches and the solidity 0.34. Measurements were made at $\frac{x}{M}$ equal to or greater than 42, and mean speed 26.3, 41.7 and 83.4 ft/sec. The turbulence decay and scales were reported by Comte-Bellot and Corrsin.

(3) Round Jet ($R_\lambda = 350 \sim 830$)

The jets were generated by two single-stage axial fan units in tandem exhausting directly through nozzles with diameters

6 and 2.53 inches, with contraction ratios 6.67:1 and 37.5:1. Measurements were made on the jet axes, fifty orifice diameters downstream from the nozzles. The mean speeds were 8.0, 10.0 and 19 ft/sec at the points of measurements. The turbulent characteristics at $R_\lambda = 830$ were measured by Gibson[24]. Cases with lower Reynolds numbers were obtained by decreasing mean speed and (or) reducing orifice diameter. Reynolds numbers and Kolmogorov-scale frequencies were evaluated from those at $R_\lambda = 830$ by assuming similarity and local isotropy of the turbulence in the jet.

2.2 Hot-Wire Anemometers and Probes

Velocity fluctuations in grid-generated turbulence were measured with Shapiro and Edwards constant current hot-wire anemometer units. The amplifier has separately adjustable low and high cut-off frequencies, and a built-in thermal compensation circuit. The compensation circuit settings were determined with square wave injection technique. Wire overheat ratios of 0.3 to 0.4 were used. Due to the small turbulence levels (about 2%), the amplifier output (A.C. coupled) is very nearly proportional to the velocity fluctuations, within the set frequency range.

For the measurements in jets, a Disa type 55D01 constant temperature anemometer was used in conjunction with a Disa type 55D10 linearizer. An overheat ratio of 0.7 and a linearizer exponent setting of 2.22 were used. These were found to yield a linear calibration curve.[25] The linearizer output was filtered by a Disa type 55D25 auxiliary unit, which is an amplifier with separately adjustable low

and high cut-off frequencies. The output of the auxiliary unit is then proportional to velocity fluctuations within its set frequency range.

Hot-wire probes were made of jeweler's broaches encased in Nu-Weld dental cement, with 1/4 inch stainless steel tube as main shafts. In case of two-wire measurements, one probe was bent up at an angle (see Figure 1) to minimize interference and to allow "meshing" of the two probes to aid in determining zero separation. The r_1 and r_2 separation distances were read on micrometers graduated in thousandths of an inch.

Only the streamwise turbulent velocity component was measured, with a single wire set normal to the mean flow. All data were taken with platinum-(10%)rhodium wire etched from Wollaston type after the silver coating had been soldered to the tips of the jeweler's broaches. Wires 0.00005 inches in diameter and 0.01 to 0.015 inch long were used, except the measurements of band-pass signals of grid-generated turbulence. There, in order to increase the signal-to-noise ratio of the band-pass signal with high mid-band frequencies, 0.000025 inch wires, 0.01 inch long, were used without thermal compensation. The reciprocal of the thermal time constant of this wire is about 6.5 kHz, which is higher than the Kolmogorov-scale frequency (5.9 kHz) of the particular turbulent flow field in which these wires were used.

2.3 Fine-structure Signal Acquisition Circuits

Three kinds of circuits were used to extract fine-scale

signals from the outputs of the anemometer amplifiers: differentiation circuit, band-pass filter, and high-pass filter.

An RCA CA3010A integrated circuit operational amplifier was used to obtain the first derivative. The output was differentiated again with a Disa type 55A06 differentiator with nominal time constant of 0.2 msec. In this experiment differentiation tends to reduce signal-to-noise ratio; a Krohn-Hite model 330-M filter with separately adjustable low and high cut-off frequencies and 24 db/octave cut-off at both ends was used to attenuate the unwanted high frequency signal and noise. A block diagram is shown in Figure 2. When first derivative was measured, the filter was connected directly to the output of CA3010A. The frequency responses are shown in Figure 3.

The Krohn-Hite filter was used to obtain band-pass signals with various mid-band frequencies f_m and bandwidths $\frac{\Delta f}{f_m}$ greater than 0.5. To realize a filter with bandwidth less than 0.5, a Dytronics Model 720 filter was used in cascade with the Krohn-Hite filter. The Dytronics filter has three constant-percentage bandwidth settings, all less than 0.5, the minimum bandwidth of Krohn-Hite filter. The cascade of the two filters is necessary because of the insufficient attenuation rate on the tails of the frequency response curve of the Dytronic filter.

For the two-wire detection of the statistical geometry of fine-scale structure, four identical four-pole Butterworth high-pass filters with amplifiers were built. A circuit diagram is shown in Figure 5. The last stage amplifier has a 6 db/octave high-frequency

cut-off to reduce the noise. The frequency response is shown in Figure 6.

2.4 Flatness Factor Measurements

Figure 7 shows the block diagram of the instruments to measure the flatness factor of a random variable $e(t)$. A Philbrick operational amplifier was used to raise the input signal $e(t)$ to a desirable level. The amplifier has a frequency response flat up to 20 kHz.(-1 db). The RC circuit at the output of amplifier is to eliminate any DC level due to drift and improper bias of the operational amplifier. A signal proportional to $e^2(t)$ was obtained through Philbrick Model Q3-M1P or GPS Model MU-405 multiplier, the frequency responses and static transfer characteristics of which are shown in Figures 8 and 9. The time average* was taken with a Kramer timer and SOS Model SI-100 integrator. The integrator output Q_1 was proportional to $\overline{e^2}$ and read with a Cubic Model V-46P digital voltmeter. With switches at positions 2, the multiplier output was squared and partially averaged by vacuum thermocouples, then amplified with Honeywell Model A20B DC amplifier to a desirable amplitude before entering the integrator. Thus the voltmeter would read a value proportional to $\overline{e^4}$. The flatness factor was then calculated by the formula

$$F = K \frac{Q_2}{Q_1} \tag{2.1}$$

---

*In this experiment, the random variables are stationary and time integral scales exist, which is a sufficient condition for an ergodic property.[26] Therefore, ensemble average may be computed as time average.

where the constant K was determined with the use of sine waves and Gaussian "noise" as $e(t)$. The flatness factors of sine wave and Gaussian noise are 1.5 and 3.0 respectively, and the constants K determined with them agree within 2%.

The vacuum thermocouple circuit consists of a variable protective resistor in series with five vacuum thermocouples with heaters connected in parallel and thermocouples connect in series. The use of multiple vacuum thermocouples not only increases the output capability but also helps to average out the randomly "imperfect" (non-square) characteristics of individual ones. The transfer characteristics is shown in Figure 10.

The Honeywell DC amplifier has a frequency response flat up to 20 kHz (-1 db) and DC drift negligible with respect to signal level.

The integrator has an inherent error voltage E_r across the input terminals, which depends on the output readings as shown in Figure 11. During the period of integration, this error voltage causes a current flow in the input circuit. This current gets integrated, to yield an error at the output, or a "drift" in cases when the output should be zero. The drift characteristics are also shown in Figure 11, with various sources and source impedences. Since the error voltage changes sign at the mid-scale of output reading, the error was minimized by setting the initial reading at such a magnitude that the initial (before integration) and the final (after integration) readings were roughly symmetric with respect to mid-scale. The net time integral was then obtained by subtracting initial reading from final reading.

Due to the finite ceiling to floor ratio of the multipliers' transfer characteristics, their input signal levels cannot be arbitrarily set. If the input signal is too high, portions of the signal will be clipped. If the input signal is too low, a large part of the signal will be smaller than the level above which the multipliers square properly. Figure 12 shows the effect, on the measured flatness factors, of the input amplitude by changing the gain of operational amplifier. The values of flatness factors at the level part of the curves were considered to have least errors and used as true flatness factors. These values were also obtained by setting the amplifier gains such that the multipliers' outputs were observed to be barely clipped on an oscilloscope. This "barely clipped" criterion was then used to set the gain of the amplifier.

2.5 Probability Measurements

The probability distribution functions were measured with a QTL Model 317 amplitude distribution analyzer, which measured the relative time duration an input signal exceeds some reference level. Numerical differentiations of the probability distributions were performed with I.B.M. Model 7094 computer to obtain probability density functions. Each set of experimental data was faired graphically with a smooth curve as shown in Figure 13. More than sixty points were taken from each curve as input data for the computer program. Every three adjacent points were fitted with a second order curve and the slope of its secant was evaluated. This

slope equals that of the tangent of the curve at the middle point. A test of this differentiation technique has been made on a normal distribution curve; the result is shown in Figure 14 and agrees with normal density quite well.

2.6 Intermittency Measurements

A technique of measuring an intermittent signal $e(t)$ was introduced by Townsend.[27] The technique involves generating a signal $I(t)$ that is a random square wave, equal to a constant (e.g. 1.0) when $e(t)$ is at its "higher state" and zero when $e(t)$ is at its "lower state." The time average of $I(t)$ is then called the "intermittency factor" of $e(t)$. The electronic circuits to generate the intermittent signal $I(t)$ have been developed and refined by several investigators, mainly in experiments to study the turbulent-nonturbulent interfaces at a "free" fluid boundary. A detailed historical account may be found in Kohan's[28] thesis.

Four identical intermittency circuits were built with the same principle of operation as those of previous investigators. A block diagram of the circuit indicating the operations on a hypothetical signal is given in Figure 15. The actual circuit is given in Figure 16. The incoming voltage $e(t)$ from the filter is rectified by the rectifier circuit.[29] The purpose of the variable resistor is to assure equal gain for both polarities of signal. To reduce noise, the rectified signal is made to work against a bias at the base of the transistor Q1, which works as an emitter follower. The pair of transistors Q2 and Q3 constitutes a level comparator, with

reference level controlled by the 20-turn trim pot R2.

The signal at the collector of Q2 is roughly a random square wave as shown at the output of the first level comparator in Figure 15, where the finite transition time between two states has been exaggerated. The finite transition time is due to the need of 0.15 volts excursion at the base voltage of the transistor Q2 in order to change it from cut-off to saturation, or vice versa. This signal also has a problem of "drop-out." During the period when $e(t)$ is at the "higher state," the magnitude of the rectified signal will fall below the comparator reference level at random times, giving break in the intermittent record. An RC circuit is used to smooth over the drop-out. The time constant of the RC circuit is set approximately at $1/2\pi f_p$, where f_p is the frequency at which the spectrum of $e(t)$ is maximum.

The DC level of the smoothed signal is then blocked by another RC circuit before the signal passes through emitter follower Q4 and the second level comparator. The smoothed signal is obtained from the connector S2 and displayed with $e(t)$ on a Hughes Model 104D dual trace storage oscilloscope. By comparing the traces of $e(t)$ and the signal from S2, it is possible to adjust R2 until the latter follows the former closely.

The transistors Q5 and Q6 constitute the second level comparator which transforms the smoothed signal into a random square wave. The smoothed signal has a sufficiently high magnitude so that the level comparator output can be taken to be a square wave with rise and fall times small compared to the typical period of an on-off cycle. The

transistor Q7 brings the two states of the random square wave to zero and about 3 volts. The signal from the connector S3 is then displayed with $e(t)$ on the storage oscilloscope; R4 is adjusted until the two correspond closely. Then the signal at S3 is $I(t)$

Two statistical properties of $I(t)$ were measured, average pulse frequency n and intermittency factor γ. The average pulse frequency was measured by counting the pulses of $I(t)$ with a CMC Model 226B universal counter-timer. To measure intermittency factor, a 500 kHz sine wave and $I(t)$ were fed to a NAND gate made of RCA 2205D integrated circuit. The average pulse frequency of the NAND gate output was measured with the counter, and its ratio to 500 kHz is the intermittency factor.

The measured γ and n depended on the settings of the reference levels of the level comparators. By careful comparison between the signals displayed on the storage oscilloscope, a repeatability within $\pm$ 5% was achieved for the high-pass signal from a Butterworth filter. A more detailed investigation was made on the particular case of the grid-generated turbulence with $R_\lambda = 110$. The reference levels yielding $\gamma = 0.30$ for its high-pass signal were checked to be optimum by the following experiment. After the reference levels were set according to visual comparison of the displayed signals, the turbulence-generating grid was removed from the wind tunnel, while the mean flow velocity and the settings of all instruments were kept unchanged. The output of the intermittency circuit became

identical to zero; this showed that the reference levels were large enough to eliminate all noise. Then the gain of the hot-wire anemometer amplifier was increased by one step (a factor of $\sqrt{2}$) and $I(t)$ was observed to be at its "on state" occasionally; this suggested that the reference levels were not too high, and hence optimum.

2.7. Coincidence Measurements

Figure 17 shows the block diagram of the instruments used to measure the probability that two hot-wires register fine-scale structure simultaneously. An AD YU Model 801 D1 delay line was used to delay the signal from one of the hot-wires. In order to match the impedences of the delay line and regain the attenuation through it, operational amplifier and emitter followers were used in conjunction with it as shown in Figure 18. Frequency response of the delay line circuit is shown in Figure 19. A performance check of the delay line circuit was made by measuring the ratios of the pulse frequencies and the intermittency factors of the random square waves at the input and output of the circuit. As shown in Figure 20, these values are quite close to unity and a reshaping of the wave form after the delay line was not necessary for the present investigation.

Two statistical quantities were measured for the probability of coincidence, the frequency, Π_2 , and the time fraction, γ_2 , that both hot-wires registered fine-scale signals. They were measusred in the same ways as Π and γ . In cases that one of the signals $I(t)$ was to be delayed, γ_2 may be measured more conveniently with PAR Model 100 correlation function computer. The computer

calculates the cross correlation of its inputs and an X-Y plotter can plot the cross correlation as a function of delay time τ . The cross correlation coefficient is just the ratio of γ_2 to γ .

III. IDENTIFICATION OF THE STATISTICAL GEOMETRY OF THE FINE-STRUCTURE REGIONS

The experimental evidence showed that the fine-scale components of turbulence localize in relatively small regions of the flow field. These small regions are presumably superimposed on the larger velocity fluctuation field and are strained by the general turbulence.

Let us consider a fluid element small enough that the instantaneous strain-rate is approximately uniform over it. If the strain-rate tensor of the fluid element is described in terms of its principal axes, it takes the form

$$\begin{Vmatrix} S_1 & 0 & 0 \\ 0 & S_2 & 0 \\ 0 & 0 & S_3 \end{Vmatrix}$$

where S_1, S_2, and S_3 are the principal rates of strain. In an incompressible turbulent fluid, S_1, S_2, and S_3 are random variables satisfying the following (mass balance) condition:

$$S_1 + S_2 + S_3 = 0$$

Therefore, S_1, S_2, and S_3 cannot be all of the same sign simultaneously. If the rotation of the principal axes relative to the fluid element is small enough during a time interval comparable to the Kolmogorov time scale, $t_k = \left(\nu/\langle\varepsilon\rangle\right)^{1/2} \simeq 1/(\text{r.m.s. vorticity})$, of the turbulence, the Lagrangian time average, $\widetilde{S}_1$, $\widetilde{S}_2$, and $\widetilde{S}_3$ may be

taken as the average strain-rate in fixed direction relative to the fluid element.* At the end of the time interval t_k, a fluid element, with three orthogonal dimensions of the same order of magnitude initially, will have the following shapes according to the signs of $\tilde{\varsigma}_1$, $\tilde{\varsigma}_2$, and $\tilde{\varsigma}_3$:

(a) "blob": $\ell_1 \simeq \ell_2 \simeq \ell_3$, if $\tilde{\varsigma}_1 \simeq \tilde{\varsigma}_2 \simeq \tilde{\varsigma}_3 \simeq 0$

(b) "rod": $\ell_1 \simeq \ell_2 \ll \ell_3$, if $\tilde{\varsigma}_1 \simeq \tilde{\varsigma}_2 < 0$, $\tilde{\varsigma}_3 > 0$

(c) "slab": $\ell_1 \ll \ell_2 \simeq \ell_3$, if $\tilde{\varsigma}_1 < 0$, $\tilde{\varsigma}_2 \simeq \tilde{\varsigma}_3 > 0$

(d) "ribbon": $\ell_1 \ll \ell_2 \ll \ell_3$,

if (1) $\tilde{\varsigma}_1 < \tilde{\varsigma}_2 < 0$, $\tilde{\varsigma}_3 > 0$

(2) $\tilde{\varsigma}_1 < 0$, $\tilde{\varsigma}_3 > \tilde{\varsigma}_2 > 0$

where ℓ_1, ℓ_2, and ℓ_3 are three orthogonal dimensions of the fluid element after being strained. The above four possible categories of geometry are the result of the straining of initially "blob-like" geometry. Since the detailed process of the generation of the fine-structure from the large-scale motions is pretty much unknown, we simply look at initially "blob-like" geometry having no initial preferred direction. The above four categories include all possible

---

*Rigorous proof for the persistence of the local straining motion has not yet been obtained. However, it is reasonable to expect that the direction of the principal axes relative to the fluid element changes relatively slowly, since both rotate roughly with the vorticity. The degree of persistence of local straining motion, particularly the principal rate of strain and the direction of the principal axes, has been discussed by Batchelor[12] and Batchelor and Townsend.[30] Some evidence on the persistence of any type of strain referred to axes rotating with the fluid element was demonstrated by Townsend[31] in measurements of cooling of heat spots in a turbulent fluid.

relationships among the relative magnitudes of ℓ_1 , ℓ_2 , and ℓ_3 . Any other type of initial geometry will introduce no new category after straining.

For simplicity in the preliminary investigation, we make no attempt to distinguish case (d). Case (d)-(1) is actually more or less the same as case (b), while case (d)-(2) is more or less the same as case (c). Therefore, case (d) will be considered as special case of (b) or (c), and only three possible categories of geometries will be analyzed and identified in this investigation.

In order to establish distinct differences in measurable statistical functions for the three geometric categories, we now analyzed three special kinds of random binary fields which may be considered as paradigms for the three categories: spheres as model "blobs," infinite circular cylinders as model "rods," and infinite plane slabs as model "slabs." We consider

(a) spheres with random diameters ℓ ,

(b) infinitely long circular cylinders with random diameters ℓ , or

(c) infinite plane slabs with random thicknesses ℓ ,

distributed randomly in space. ℓ is a random variable with probability function $g(\ell)$ defined as follows:

(a) spherical model: $g(\ell)\,d\ell$ is the average number of spheres, in unit volume of space, with diameters between ℓ and $\ell + d\ell$, so the average number of spheres in unit volume is $N = \int_0^\infty g(\ell)\,d\ell$

if the density of spheres is so small that the overlap effect is negligible;

(b) cylindrical model: $q(\ell)\,d\ell$ is the average length of cylinders, in unit volume of space, with diameters between ℓ and $\ell+d\ell$, so the total length of cylinders in unit volume is

$$L = \int_0^\infty q(\ell)\,d\ell$$

if the density of cylinders is so small that the overlap effect is negligible;

(c) slab model: $q(\ell)\,d\ell$ is the center-plane area, in unit volume of space, of slabs with thicknesses between ℓ and $\ell+d\ell$, so the total area of slabs in unit volume is

$$S = \int_0^\infty q(\ell)\,d\ell$$

if the density of slabs is so small that the overlap effect is negligible.

It is further assumed that the statistical distributions of these small regions are homogeneous and isotropic.

1. Single Hot-Wire Detection

As the fine-structure active regions are swept past by the mean flow, the hot-wire and the associated electronic circuits put out the signal I(t)

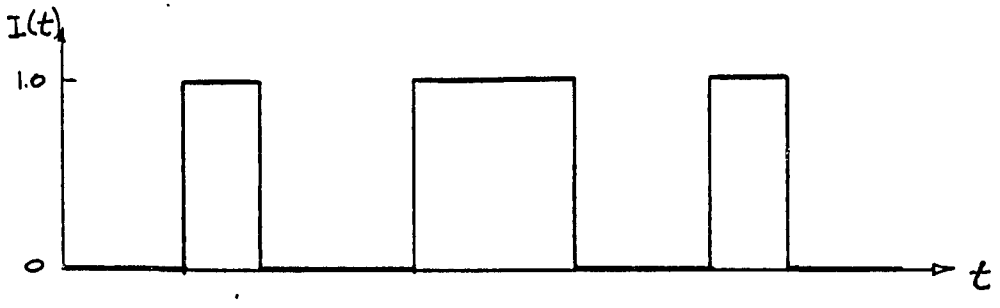

where the level 1.0 corresponds to times when the hot-wire is in a fine-structure region, and the level 0 corresponds to other times.

Two independent statistical quantities which may be easily obtained from the signal I(t) are

γ : intermittency factor, the fraction of time when I(t) is at the level 1.0;

n : the average number of "pulses" per unit time.

It can easily be shown that the intermittency factor γ equals γ_s, the fraction of space occupied by the fine-structure. If a straight line is drawn through the flow field at any instant, the length fraction that lies within fine-structure regions is γ_s, since for each point on the line the probability that it lies inside the regions is γ_s. γ of I(t) corresponds to what would be obtained by drawing a sampling line in the mean flow direction, if the "Taylor's hypothesis"* holds true.

γ and n may be related to statistical properties of the three special geometries assumed. Let

$m = n/U$: the average number of the fine-structure regions detected by the hot-wire per unit distance it traverses;

$\langle w \rangle = \gamma/m$: the average dimension of the fine-structure regions as measured by the hot-wire.

In all of the following analysis, consider these fine-structure regions in a cube of unit volume with one side parallel to the mean flow. As the cube is convected by the mean flow past the hot-wire,

---

*see Appendix A1.

the "expected" number of the fine-structure regions detected is m, and the sum of the linear dimensions W of these detected regions is γ, when length is measured in the same units as the "unit" cube. The coordinate system is so chosen that the hot-wire is at the origin and the mean flow is in the positive X-direction.

(1) Spherical Model

The probability that a sphere in the unit cube is detected by a point probe is the ratio of its projected area to the projected area of the unit cube on the y-z plane, i.e.

$$\frac{1}{4}\pi\ell^2 \Big/ \text{unit area} = \frac{1}{4}\pi\ell^2$$

Then, the expected number of spheres, of diameters between ℓ and $\ell+d\ell$, detected during the time when the unit cube is swept past the hot-wire, is

$$g(\ell)\ \frac{1}{4}\pi\ell^2 d\ell \tag{3.1}$$

Therefore

$$m = \int_0^\infty g(\ell)\ \frac{1}{4}\pi\ell^2 d\ell$$

$$= \frac{\pi}{4} N \langle \ell^2 \rangle \tag{3.2}$$

where $\langle\ \rangle$ means expectation value (i.e. ensemble average).

Let a sphere be carried along by the mean flow with its center at a distance y_c from the x-axis. The hot-wire

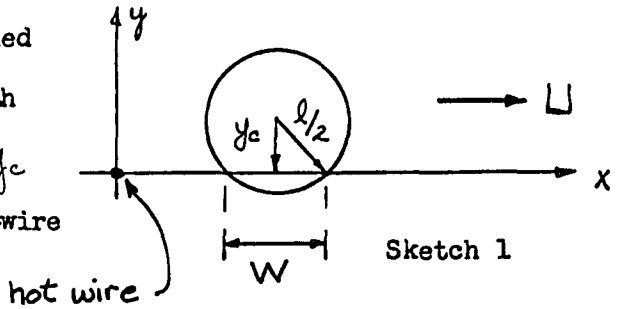

Sketch 1

will measure W as the dimension of the sphere,

$$W = \begin{cases} 2\sqrt{\left(\frac{\ell}{2}\right)^2 - y_c^2} & \text{if } y_c \le \ell/2 \\ 0 & \text{if } y_c \ge \ell/2 \end{cases}$$

The number of spheres, with diameters between ℓ and $\ell + d\ell$, detected by the hot-wire is given by Equation (3.1). Among these spheres, the probability that their centers lie at a distance $y_c \le y \le y_c + dy_c$ from the x-axis is

$$\frac{2\pi y_c}{\frac{1}{4}\pi \ell^2} dy_c$$

Therefore

$$\gamma = \int_0^\infty \int_0^{\ell/2} 2\sqrt{(\ell/2)^2 - y_c^2} \cdot 2\pi y_c \, g(\ell) \, dy_c \, d\ell$$

$$= \frac{\pi}{6} N \langle \ell^3 \rangle \qquad (3.3)$$

which is the total volume of spheres at all sizes, per unit volume of space. From Equations (3.2) and (3.3)

$$\langle W \rangle = \frac{\gamma}{m} = \frac{2}{3} \frac{\langle \ell^3 \rangle}{\langle \ell^2 \rangle} \qquad (3.4)$$

and the N has cancelled out.

(2) Cylindrical Model

The probability that unit length of a cylinder is detected by a point probe equals the ratio of its projected area to the projected area of the unit cube on the y-z plane, i.e.

$$\ell \sin\theta \cdot \text{unit length} / \text{unit area} = \ell \sin\theta$$

where Θ is the angle between the cylinder axis and the x-axis. Since the orientation of cylinders is assumed to be statistically isotropic, the probability density of Θ is the measure of relative solid angle giving Θ , i.e.

$$\begin{cases} \sin\Theta & 0 \le \Theta \le \frac{\pi}{2} \\ 0 & \text{otherwise} \end{cases}$$

Then the expected number of cylinders "hitting" the hot-wire and having diameters between ℓ and $\ell + d\ell$ with orientation angles between Θ and $\Theta + d\Theta$ is

$$g(\ell)\, \ell \sin^2\Theta \, d\Theta \, d\ell \tag{3.5}$$

for $\quad 0 \le \Theta \le \pi/2 \qquad 0 \le \ell < \infty$

Therefore

$$m = \int_0^\infty \int_0^{\frac{\pi}{2}} g(\ell)\, \ell \sin^2\Theta \, d\Theta \, d\ell$$

$$= \frac{\pi}{4} L \langle \ell \rangle \tag{3.6}$$

In Sketch 2, a cylinder is convected along the x-axis with its axis at an angle Θ to the x-axis. Choose the y-axis so that the x-y plane is parallel to the cylinder axis, and the distance between them is z_c.

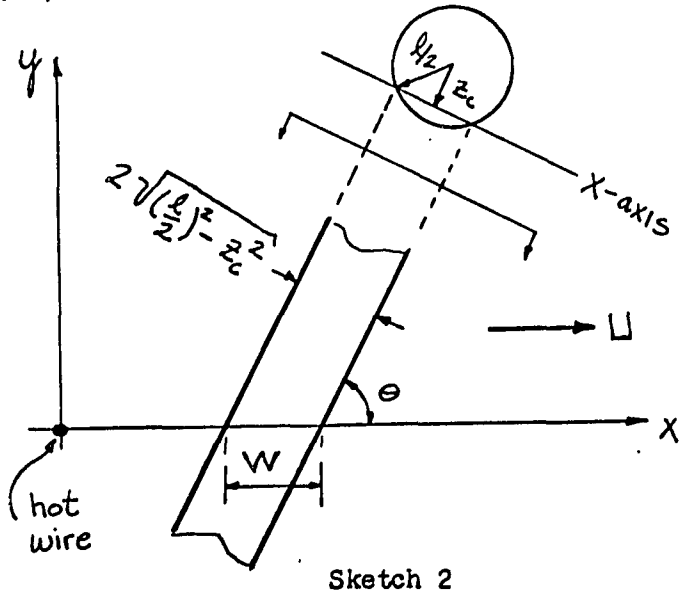

Sketch 2

The hot-wire will measure W as the dimension of the cylinder

$$W = \begin{cases} 2\sqrt{\left(\frac{\ell}{2}\right)^2 - z_c^2} \,/ \sin\theta & \text{if } |z_c| \le \ell/2 \\ 0 & \text{if } |z_c| \ge \ell/2 \end{cases}$$

Among those cylinders given by Equation (3.5), the probability of having their axes at a distance between z_c and $z_c + dz_c$ from the x-y plane is dz_c/ℓ

Therefore

$$\gamma = \int_0^\infty \int_0^{\pi/2} \int_{-\ell/2}^{\ell/2} \frac{2\sqrt{\left(\frac{\ell}{2}\right)^2 - z_c^2}}{\sin\theta} g(\ell) \sin^2\theta \, dz_c \, d\theta \, d\ell$$

$$= \int_0^\infty \int_0^{\pi/2} g(\ell) \sin\theta \left[z_c\sqrt{\left(\frac{\ell}{2}\right)^2 - z_c^2} + \left(\frac{\ell}{2}\right)^2 \sin^{-1} \frac{z_c}{\left(\frac{\ell}{2}\right)} \right]_{-\frac{\ell}{2}}^{\ell/2} d\theta \, d\ell$$

$$= \int_0^\infty g(\ell) \left(\frac{\ell}{2}\right)^2 \pi \, d\ell$$

$$= \frac{\pi}{4} L \langle \ell^2 \rangle \qquad (3.7)$$

which is the total volume of the cylinders in unit volume of space.

From Equations (3.6) and (3.7)

$$\langle W \rangle = \frac{\langle \ell^2 \rangle}{\langle \ell \rangle} \qquad (3.8)$$

and the L has cancelled out.

(3) Slab Model

The probability that a unit area of a thin slab is detected by a point probe equals the ratio of its projected area to the projected area of the unit cube on the y-z plane, i.e. $\cos\theta$

where θ is the angle between a normal to the surface and the x-axis. Since the distribution of the slabs is assumed to be statistically homogeneous and isotropic, the probability density of θ is the measure of relative solid angle giving θ , i.e.

$$\begin{cases} \sin\theta & 0 \leq \theta \leq \frac{\pi}{2} \\ 0 & \text{otherwise} \end{cases}$$

Then the expected number of slabs "hitting" the hot-wire and having thickness between ℓ and $\ell+d\ell$, with orientation angle between θ and $\theta+d\theta$, is

$$\sin\theta \cos\theta \; g(\ell)\, d\theta\, d\ell \qquad \text{for } 0 \leq \theta \leq \frac{\pi}{2}, \quad 0 \leq \ell < \infty \tag{3.9}$$

Therefore

$$m = \int_0^\infty \int_0^{\pi/2} \sin\theta \cos\theta \; g(\ell)\, d\theta\, d\ell$$

$$= \frac{1}{2} S \tag{3.10}$$

which is a particular result of Corrsin's Theorem.[32,33,34] In fact, Equations (3.2) and (3.6) may also be obtained by applying Corrsin's Theorem to randomly distributed spherical and cylindrical surfaces, respectively.

In Sketch 3, a plane slab is convected along the x-axis with its normal at angle θ to the x-axis. Choose the y-axis so that the x-y plane is normal to the slab surface. The hot-wire will

measure W as the dimension- of the slab,

$$W = \ell/\cos\theta .$$

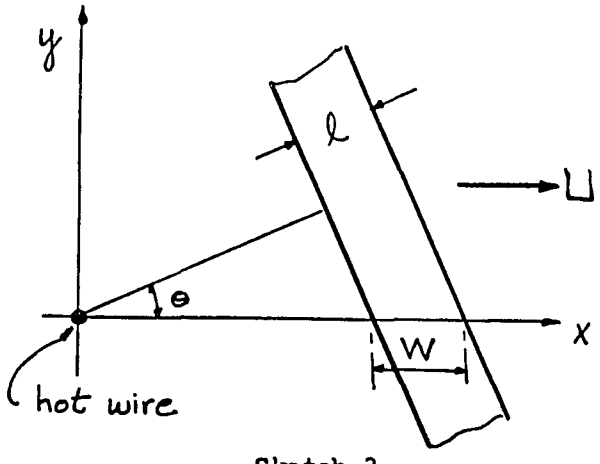

Sketch 3

Therefore, combining with Equation (3.9) gives

$$\gamma = \int_0^\infty \int_0^{\frac{\pi}{2}} \frac{\ell}{\cos\theta} \sin\theta \cos\theta \; g(\ell) \, d\theta \, d\ell$$

$$= S \langle \ell \rangle \qquad (3.11)$$

which is the average total volume of slabs per unit volume of space.

From Equations (3.10) and (3.11)

$$\langle W \rangle = 2 \langle \ell \rangle \qquad (3.12)$$

and the S has cancelled out.

The above analysis shows that γ and m, the two independent quantities most easily obtained from the single wire signal I(t), are simply related to lower order moments, i.e., $\langle \ell \rangle$, $\langle \ell^2 \rangle$, and $\langle \ell^3 \rangle$, of the characteristic length of the assumed geometries in the following ways:

(a) spherical model

$$m = \frac{\pi}{4} N \langle \ell^2 \rangle \qquad (3.2)$$

$$\gamma = \frac{\pi}{6} N \langle \ell^3 \rangle \qquad (3.3)$$

(b) cylindrical model

$$m = \frac{\pi}{4} L \langle \ell \rangle \tag{3.6}$$

$$\gamma = \frac{\pi}{4} L \langle \ell^2 \rangle \tag{3.7}$$

(c) slab model

$$m = \frac{1}{2} S \tag{3.10}$$

$$\gamma = S \langle \ell \rangle \tag{3.11}$$

If we were given a signal I(t) and were told only that it was generated by traversing a random field of spheres or of rods or of slabs, we could check the compatibility for each pair of the equations, and thus identify the field, from the measurements of γ , m , $\langle \ell \rangle$, $\langle \ell^2 \rangle$, and $\langle \ell^3 \rangle$. For example, the spherical model is possible only if the measured values of m , γ , $\langle \ell^2 \rangle$ and $\langle \ell^3 \rangle$ give the same value N from Equations (3.2) and (3.3). γ and m can be measured easily, but there is no direct way to measure $\langle \ell \rangle$, $\langle \ell^2 \rangle$, and $\langle \ell^3 \rangle$ from I(t). With only γ and m measured, solutions for $\langle \ell \rangle$, $\langle \ell^2 \rangle$, and $\langle \ell^3 \rangle$ always exist, and all three kinds of geometries are possible as far as γ and m are concerned.

In addition to γ and m , the pulse length moments $\langle W^K \rangle$ can be measured from I(t). We might hope that $\langle \ell \rangle$, $\langle \ell^2 \rangle$, and $\langle \ell^3 \rangle$ could be calculated from $\langle W^K \rangle$, with $K = 1, 2, 3, \ldots\ldots$ Unfortunately, the calculation is not determinate.

(a) spherical model

$$\langle W^K \rangle = \frac{2}{K+2} \frac{\langle \ell^{K+2} \rangle}{\langle \ell^2 \rangle} \qquad \text{for } K = 1, 2, 3, \ldots$$

(b) cylindrical model

$$\langle W \rangle = \frac{\langle \ell^2 \rangle}{\langle \ell \rangle}$$

$$\langle W^2 \rangle = \frac{4}{3} \frac{\langle \ell^3 \rangle}{\langle \ell \rangle}$$

$\langle W^K \rangle$ diverges for $K \geq 3$

(c) slab model

$$\langle W \rangle = 2 \langle \ell \rangle$$

$\langle W^K \rangle$ diverges for $K \geq 2$

In case (a) and (b), the system of equations is not closed, i.e., more unknowns $\langle \ell^K \rangle$ than the number of equations. In case (c), the result just serves to check Equation (3.12) and no new information is obtained. Therefore, a technique of double or multiple probe detection must be explored before the statistical geometry can be determined.

2. Two-Hot-Wire Detection

Since it is assumed that the statistical distribution of the fine-structure regions is homogeneous and isotropic, γ and n are the same for the signals from both hot-wires at different positions. Useful joint information is the probability that both hot-wires lie within a single fine-structure region. Let $I_c(t)$ be the signal which equals 1.0 during the time both wires are inside the same fine-structure region and equal zero otherwise. Define γ_2, m_2 and $\langle W_2 \rangle$ for $I_c(t)$ analogous to γ, m and $\langle W \rangle$ for $I(t)$.

(1) Spherical Model

(A) Two hot-wires separated in the x-direction with distance r_1 .

The probability that a sphere in the unit cube is detected by both hot-wires simultaneously equals the projected area, on the y-z plane, of that part of the sphere with dimension W in the x-direction greater than r_1 , i.e.

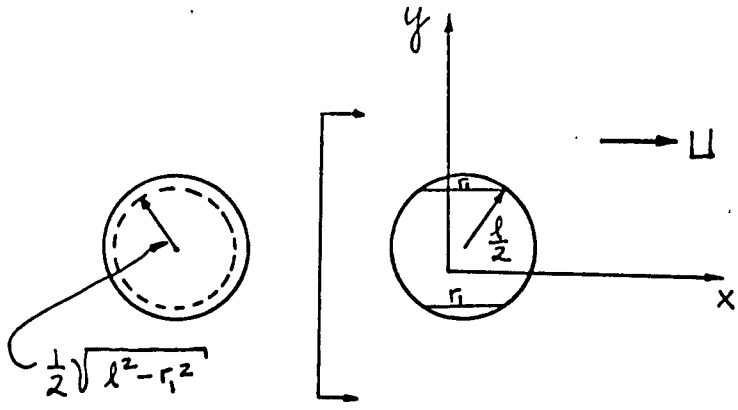

Sketch 4

$$\begin{cases} \pi \left[\left(\frac{l}{2}\right)^2 - \left(\frac{r_1}{2}\right)^2 \right] / \text{unit area} & \text{if } l \geq r_1 \\ 0 & \text{if } l \leq r_1 \end{cases}$$

the area of a circle with radius $\frac{1}{2}\sqrt{l^2-r_1^2}$, as shown in Sketch 4. Then, the expected number of spheres, of diameters between l and $l+dl$, detected by both wires simultaneously is

$$\begin{cases} \frac{\pi}{4} l^2 \left(1-\frac{r_1^2}{l^2}\right) g(l)\, dl & \text{if } l \geq r_1 \\ 0 & \text{if } l \leq r_1 \end{cases} \qquad (3.13)$$

Therefore, the expected number of "coincidence" events is

$$m_2 = \int_{r_1}^{\infty} \frac{\pi}{4} \ell^2 \left(1 - \frac{r_1^2}{\ell^2}\right) g(\ell)\, d\ell$$

$$= \int_0^{\infty} \frac{\pi}{4} \ell^2 \left(1 - \frac{r_1^2}{\ell^2}\right) g(\ell)\, d\ell - \int_0^{r_1} \frac{\pi}{4} \ell^2 \left(1 - \frac{r_1^2}{\ell^2}\right) g(\ell)\, d\ell$$

$$= \frac{\pi}{4} N \langle \ell^2 \rangle - \frac{\pi}{4} r_1^2 N + \frac{\pi}{4} N_{r_1} \left(r_1^2 - \langle \ell^2 \rangle_{r_1}\right)$$

and, with Equations (3.2) and (3.4)

$$\frac{m_2}{m} = 1 - \frac{r_1^2}{\langle \ell^2 \rangle} + \frac{N_{r_1} \left(r_1^2 - \langle \ell^2 \rangle_{r_1}\right)}{N \langle \ell^2 \rangle}$$

$$= 1 - \frac{4}{9} \frac{\langle \ell^3 \rangle^2}{\langle \ell^2 \rangle^3} \frac{r_1^2}{\langle w \rangle^2} + C_1(r_1) \qquad (3.14)$$

where N_{r_1} is the "distribution" function of ℓ

$$N_{r_1} = \int_0^{r_1} g(\ell)\, d\ell \quad = \quad \text{the number of spheres in unit volume with diameters } \ell \le r_1$$

and

$$\langle \ell^2 \rangle_{r_1} = \frac{1}{N_{r_1}} \int_0^{r_1} \ell^2 g(\ell)\, d\ell \quad = \quad \text{the average value of } \ell^2 \text{ for those spheres with diameters } \ell \le r_1 .$$

In Sketch 1, let the time when the hot-wire at (0,0,0) begins to register the sphere be t_o, then it will stay in the sphere up to time $t_o + \frac{W}{U}$. A wire at $(r_1, 0, 0)$ will register this sphere during the time interval $t_o + \frac{r_1}{U}$ to $t_o + \frac{r_1}{U} + \frac{W}{U}$. Then

both hot-wires will stay in this sphere during the time interval $t_o + \frac{r_1}{U}$ to $t_o + \frac{W}{U}$, if $\frac{W}{U} > \frac{r_1}{U}$. Therefore, the corresponding W_2 for both wires inside the sphere is

$$W_2 = \begin{cases} W - r_1 = 2\sqrt{(\frac{l}{2})^2 - y_c^2} - r_1 & \text{if } W \geq r_1 \\ 0 & \text{if } W \leq r_1 \end{cases}$$

Among those spheres given by Equation (3.13), the probability that their centers lie at a distance between y_c and $y_c + dy_c$ from the x-axis is

$$\frac{2\pi\, y_c\, dy_c}{\pi\left[(\frac{l}{2})^2 - (\frac{r_1}{2})^2\right]} \qquad \text{for } 0 \leq y_c \leq \tfrac{1}{2}\sqrt{l^2 - r_1^2}$$

Therefore

$$\gamma_2 = \int_{r_1}^{\infty} \int_{0}^{\frac{1}{2}\sqrt{l^2 - r_1^2}} \left(2\sqrt{(\tfrac{l}{2})^2 - y_c^2} - r_1\right) 2\pi\, y_c\, g(l)\, dy_c\, dl$$

$$= 2\pi \int_{r_1}^{\infty} g(l) \left(\frac{l^3}{12} - \frac{r_1^3}{12} - \frac{r_1 l^2}{8} + \frac{r_1^3}{8}\right) dl$$

$$= \pi \int_{0}^{\infty} g(l) \left(\frac{l^3}{6} - \frac{l^2 r_1}{4} + \frac{r_1^3}{12}\right) dl$$

$$- \pi \int_{0}^{r_1} g(l) \left(\frac{l^3}{6} - \frac{l^2 r_1}{4} + \frac{r_1^3}{12}\right) dl$$

$$= \frac{\pi}{6} N \langle l^3 \rangle \left(1 - \frac{3}{2}\frac{\langle l^2 \rangle}{\langle l^3 \rangle} r_1 + \frac{1}{2}\frac{r_1^3}{\langle l^3 \rangle}\right)$$

$$- \frac{\pi}{6} N_{r_1} \left(\langle l^3 \rangle_{r_1} - \frac{3}{2}\langle l^2 \rangle_{r_1} r_1 + \frac{1}{2} r_1^3\right)$$

and, with Equations (3.3) and (3.4)

$$\frac{\gamma_2}{\gamma} = 1 - \frac{r_1}{\langle W\rangle} + \frac{1}{2}\frac{r_1^3}{\langle l^3\rangle} - \frac{N r_1}{N}\,\frac{\frac{1}{2}r_1^3 - \frac{3}{2}r_1\langle l^2\rangle_{r_1} + \langle l^3\rangle_{r_1}}{\langle l^3\rangle}$$

$$= 1 - \frac{r_1}{\langle W\rangle} + \frac{1}{2}\frac{r_1^3}{\langle l^3\rangle} + C_2(r_1) \qquad (3.15)$$

(B) Two hot-wires separated in the y-direction with distance r_2 .

The probability, $\beta(l)$, of a sphere in the unit cube being detected by both wires simultaneously equals the area on the y-z plane in which the center of the sphere may go through and still hit both wires.

If $l \le r_2$, $\beta(l) = 0$.

If $l \ge r_2$, let the two hot-wires be at $(0, \frac{r_2}{2}, 0)$ and $(0, -\frac{r_2}{2}, 0)$, and a sphere pass through the y-z plane with its center at (y_c, z_c). As shown in Sketch 5 the sphere is cut by the x-y plane in a circle of radius

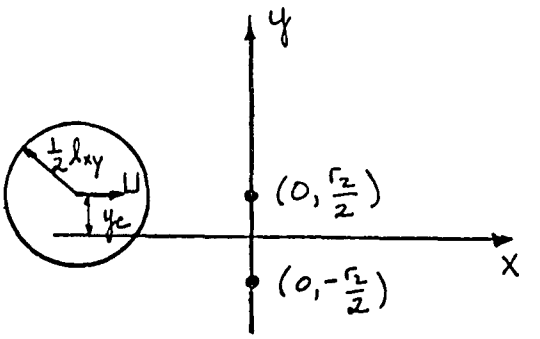

Sketch 5

$$\frac{1}{2}\,l_{xy} = \sqrt{\left(\frac{l}{2}\right)^2 - z_c^2}$$

To evaluate

$$\beta(l) = \iint_A dy_c\, dz_c \,/\, \text{unit area},$$

the limits of integration have to be determined. By letting

$$l_{xy} = r_2$$

the smallest circle in the x-y plane to hit both wires simultaneously, the limits on z_c may be found.

$$\ell_{xy} = 2\sqrt{\left(\frac{\ell}{2}\right)^2 - (z_c)_m^2} = r_2$$

$$(z_c)_m^2 = \left(\frac{\ell}{2}\right)^2 - \left(\frac{r_2}{2}\right)^2$$

$$\therefore \; -\sqrt{\left(\frac{\ell}{2}\right)^2-\left(\frac{r_2}{2}\right)^2} \le z_c \le \sqrt{\left(\frac{\ell}{2}\right)^2-\left(\frac{r_2}{2}\right)^2}$$

With given z_c in the range described above, the maximum of y_c is determined by the wire at $\left(0, -\frac{r_2}{2}\right)$ and the minimum by the wire at $\left(0, \frac{r_2}{2}\right)$, which give

$$-\left(\sqrt{\left(\frac{\ell}{2}\right)^2 - z_c^2} - \frac{r_2}{2}\right) \le y_c \le \left(\sqrt{\left(\frac{\ell}{2}\right)^2 - z_c^2} - \frac{r_2}{2}\right)$$

Therefore

$$\beta(\ell) = 4 \int_0^{\sqrt{\left(\frac{\ell}{2}\right)^2-\left(\frac{r_2}{2}\right)^2}} \int_0^{\sqrt{\left(\frac{\ell}{2}\right)^2-z_c^2}-\frac{r_2}{2}} dy_c \, dz_c$$

$$= 4 \int_0^{\sqrt{\left(\frac{\ell}{2}\right)^2-\left(\frac{r_2}{2}\right)^2}} \left(\sqrt{\left(\frac{\ell}{2}\right)^2 - z_c^2} - \frac{r_2}{2}\right) dz_c$$

$$= 2\left[\frac{r_2}{2}\sqrt{\left(\frac{\ell}{2}\right)^2-\left(\frac{r_2}{2}\right)^2} + \frac{\ell^2}{2}\sin^{-1}\left\{\sqrt{1-\left(\frac{r_2}{\ell}\right)^2}\right\} - r_2\sqrt{\left(\frac{\ell}{2}\right)^2-\left(\frac{r_2}{2}\right)^2}\right]$$

$$= \frac{\ell^2}{2}\sin^{-1}\left[1-\tfrac{1}{2}\left(\tfrac{r_2}{\ell}\right)^2 + O\left(\tfrac{r_2}{\ell}\right)^4\right] - r_2\frac{\ell}{2}\left[1-\tfrac{1}{2}\left(\tfrac{r_2}{\ell}\right)^2+O\left(\tfrac{r_2}{\ell}\right)^4\right]$$

$$= \frac{\ell^2}{2}\left[\frac{\pi}{2} - \frac{r_2}{\ell} - \frac{r_2}{\ell} + O\left(\frac{r_2}{\ell}\right)^3\right]$$

$$= \frac{\pi\ell^2}{4}\left[1 - \frac{4}{\pi}\frac{r_2}{\ell} + O\left(\frac{r_2}{\ell}\right)^3\right] \qquad (3.16)$$

Then the expected number of spheres, of diameters between ℓ and $\ell + d\ell$, detected by both wires simultaneously is

$$\beta(\ell)\, g(\ell)\, d\ell$$

and

$$m_2 = \int_{r_2}^{\infty} \beta(\ell)\, g(\ell)\, d\ell$$

$$= \int_{r_2}^{\infty} \frac{\pi}{4} \ell^2 \left[1 - \frac{4}{\pi}\frac{r_2}{\ell} + O\left(\frac{r_2}{\ell}\right)^3\right] g(\ell)\, d\ell$$

$$= \int_0^{\infty} \frac{\pi}{4}\ell^2 \left(1 - \frac{4}{\pi}\frac{r_2}{\ell}\right) g(\ell)\, d\ell - \int_0^{r_2} \frac{\pi}{4}\ell^2 \left(1 - \frac{4}{\pi}\frac{r_2}{\ell}\right) g(\ell)\, d\ell$$

$$+ \int_{r_2}^{\infty} O\left(\frac{r_2}{\ell}\right)^3 g(\ell)\, d\ell$$

$$= \frac{\pi}{4} N\left(\langle \ell^2\rangle - \frac{4}{\pi} r_2 \langle \ell\rangle\right) - \frac{\pi}{4} N_{r_2}\left(\langle \ell^2\rangle_{r_2} - \frac{4}{\pi} r_2 \langle \ell\rangle_{r_2}\right)$$

$$+ O\left(N^{r_2} r_2^{\,3} \left\langle \frac{1}{\ell}\right\rangle^{r_2}\right)$$

With Equations (3.2) and (3.4)

$$\frac{m_2}{m} = 1 - \frac{8}{3\pi} \frac{\langle \ell\rangle\langle \ell^3\rangle}{\langle \ell^2\rangle^2} \frac{r_2}{\langle W\rangle} + \frac{N_{r_2}\left(\frac{4}{\pi} r_2 \langle \ell\rangle_{r_2} - \langle \ell^2\rangle_{r_2}\right)}{N \langle \ell^2\rangle}$$

$$+ O\left(\frac{N^{r_2}}{N} \frac{r_2^{\,3}}{\langle \ell^2\rangle} \left\langle \frac{1}{\ell}\right\rangle^{r_2}\right)$$

$$= 1 - \frac{8}{3\pi} \frac{\langle \ell\rangle\langle \ell^3\rangle}{\langle \ell^2\rangle^2} \frac{r_2}{\langle W\rangle} + C_3(r_2) \qquad (3.17)$$

where

$$N^{r_2} = \int_{r_2}^{\infty} g(\ell)\, d\ell$$

$$\left\langle \frac{1}{\ell}\right\rangle^{r_2} = \frac{1}{N^{r_2}} \int_{r_2}^{\infty} \frac{1}{\ell}\, g(\ell)\, d\ell$$

The result of the analysis for $\gamma_2(r_2)$ shows that the dependence of γ_2 on r_2 is exactly the same as γ_2 on r_1. In fact, in any isotropic binary field, including blobs, rods, and slabs, γ_2 depends on the distance between the two probes only. Consider two probes at a distance r apart and at an angle θ to a reference direction. Place the pair at random in the field a large number of times; measure the number of times, N_2, they both lie in a single domain (e.g. a blob) and the number of times, N_1, a given probe lies in the domain. The value of N_2 is obviously independent of θ since the statistical distribution of the domains is assumed to be isotropic. N_2/N_1 in this "random placement" experiment is equivalent to γ_2/γ obtained by sweeping the two probes systematically over the field in a given direction.

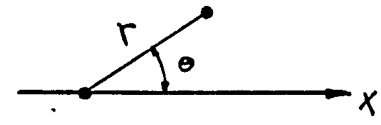

Sketch 6

(2) Cylindrical Model

(A) Two Hot-wires separated in the x-direction with distance r_1.

The probability that unit length of a cylinder is detected by both wires simultaneously equals the projected area, on the y-z plane, of that part of this unit section with dimension in the x-direction greater than r_1. Referring to Sketch 2, the projection is a rectangle with length $\sin\theta$ in the y-direction. Since the y-axis is chosen so that the cylinder is parallel to the x-y plane,

the cylinder is cut by the x-z plane in an ellipse, as shown in Sketch 7.

$$\frac{x'^2}{\left(\frac{l}{2\sin\theta}\right)^2} + \frac{z'^2}{\left(\frac{l}{2}\right)^2} = 1$$

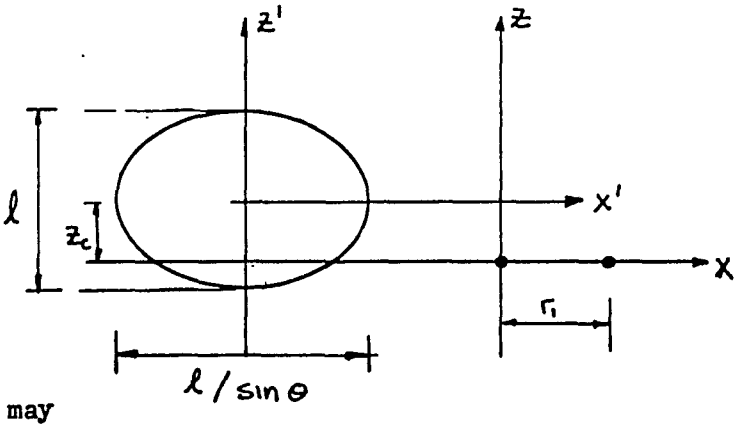

Sketch 7

The extreme values of z_c may be obtained by substituting $x' = \frac{r_1}{2}$ in the above equation, we get

$$(z_c)_m = \begin{cases} \pm\sqrt{\left(\frac{l}{2}\right)^2 - \left(\frac{r_1\sin\theta}{2}\right)^2} & \text{if } \begin{cases} l \geq r_1 \text{ or} \\ l \leq r_1,\ \theta \leq \sin^{-1}\left(\frac{l}{r_1}\right) \end{cases} \\ 0 & \text{if } l \leq r_1 \text{ and } \theta \geq \sin^{-1}\left(\frac{l}{r_1}\right) \end{cases}$$

Then the probability is

$$\text{unit length} \cdot 2\sin\theta\sqrt{\left(\frac{l}{2}\right)^2 - \left(\frac{r_1}{2}\sin\theta\right)^2} \Big/ \text{unit area}.$$

Since the orientation of cylinders is assumed to be statistically isotropic, the probability density of θ is the measure of relative solid angle giving θ, i.e.

$$\begin{cases} \sin\theta & 0 \leq \theta \leq \frac{\pi}{2} \\ 0 & \text{otherwise} \end{cases}$$

Then the expected number of cylinders hitting both wires simultaneously, with diameters between l and $l + dl$, orientation angles

between θ and $\theta + d\theta$, is

$$\begin{cases} g(\ell)\; 2\sin^2\theta \sqrt{\left(\frac{\ell}{2}\right)^2 - \left(\frac{r_1}{2}\sin\theta\right)^2}\, d\theta\, d\ell \\ \qquad \text{if} \quad \ell \geq r_1\,,\ 0 \leq \theta \leq \pi/2 \quad \text{or} \\ \qquad\qquad \ell \leq r_1\,,\ 0 \leq \theta \leq \sin^{-1}(\ell/r_1) \end{cases} \tag{3.18}$$

and $\quad 0 \qquad \text{if} \quad \ell < r_1\,, \quad \theta \geq \sin^{-1}(\ell/r_1)$

$$m_2 = \int_{r_1}^{\infty}\int_0^{\pi/2} 2\, g(\ell)\, \sin^2\theta \sqrt{\left(\frac{\ell}{2}\right)^2 - \left(\frac{r_1 \sin\theta}{2}\right)^2}\, d\theta\, d\ell$$
$$+ \int_0^{r_1}\int_0^{\sin^{-1}(\ell/r_1)} 2\, g(\ell)\, \sin^2\theta \sqrt{\left(\frac{\ell}{2}\right)^2 - \left(\frac{r_1\sin\theta}{2}\right)^2}\, d\theta\, d\ell$$

$$= \int_{r_1}^{\infty}\int_0^{\pi/2} \ell\, g(\ell)\, \sin^2\theta \left[1 - \tfrac{1}{2}\left(\frac{r_1}{\ell}\right)^2 \sin^2\theta + O\left(\frac{r_1\sin\theta}{\ell}\right)^4\right] d\theta\, d\ell$$
$$+ \int_0^{r_1}\int_0^{\sin^{-1}(\ell/r_1)} \ell\, g(\ell)\, \sin^2\theta \left[1 - \tfrac{1}{2}\left(\frac{r_1}{\ell}\right)^2 \sin^2\theta + O\left(\frac{r_1\sin\theta}{\ell}\right)^4\right] d\theta\, d\ell$$

$$= \int_{r_1}^{\infty} \ell\, g(\ell) \left[\frac{\pi}{4} - \frac{3\pi}{32}\left(\frac{r_1}{\ell}\right)^2 + O\left(\frac{r_1}{\ell}\right)^4\right] d\ell + \int_0^{r_1} \ell\, g(\ell) \left[\frac{1}{30}\left(\frac{\ell}{r_1}\right)^3 + O\left(\frac{\ell}{r_1}\right)^5\right] d\ell$$

$$= \frac{\pi}{4} L\langle\ell\rangle - \frac{3\pi}{32} r_1^2 L\left\langle\frac{1}{\ell}\right\rangle + O\left(L^{r_1} r_1^4 \left\langle\frac{1}{\ell^3}\right\rangle^{r_1}\right) +$$
$$\int_0^{r_1} \ell\, g(\ell) \left[-\frac{\pi}{4} + \frac{3\pi}{32}\left(\frac{r_1}{\ell}\right)^2 + \frac{1}{30}\left(\frac{\ell}{r_1}\right)^3 + O\left(\frac{\ell}{r_1}\right)^5\right] d\ell$$

$$= \frac{\pi}{4} L\langle\ell\rangle - \frac{3\pi}{32} L\left\langle\frac{1}{\ell}\right\rangle r_1^2 + O\left(L^{r_1} r_1^4 \left\langle\frac{1}{\ell^3}\right\rangle^{r_1}\right) + L_{r_1}\left[\frac{3\pi}{32} r_1^2 \left\langle\frac{1}{\ell}\right\rangle_{r_1} - \frac{\pi}{4}\langle\ell\rangle_{r_1} + O\left(\frac{\langle\ell^4\rangle_{r_1}}{r_1^3}\right)\right]$$

and, with Equations (3.6) and (3.8)

$$\frac{m_2}{m} = 1 - \frac{3}{8}\frac{r_1^2}{\langle\ell\rangle}\left\langle\frac{1}{\ell}\right\rangle + O\left(\frac{L^{r_1}}{L}\frac{r_1^4}{\langle\ell\rangle}\left\langle\frac{1}{\ell^3}\right\rangle^{r_1}\right)$$
$$+ \frac{L_{r_1}\left[\frac{3}{8} r_1^2 \left\langle\frac{1}{\ell}\right\rangle_{r_1} - \langle\ell\rangle_{r_1} + O\left(\frac{\langle\ell^4\rangle_{r_1}}{r_1^3}\right)\right]}{L\langle\ell\rangle}$$

$$= 1 - \frac{3}{8}\frac{\langle\ell^2\rangle^2}{\langle\ell^3\rangle}\left\langle\frac{1}{\ell}\right\rangle \frac{r_1^2}{\langle w\rangle^2} + C_4(r_1) \tag{3.19}$$

If another hot-wire is placed at $(r_1,0,0)$ in Sketch 2, analogous to the spherical model, the corresponding W_2 for both wires inside the cylinder is

$$W_2 = \begin{cases} W - r_1 = 2\dfrac{\sqrt{(\frac{\ell}{2})^2 - z_c^2}}{\sin\theta} - r_1 & \text{if } W \geq r_1 \\ 0 & \text{if } W \leq r_1 \end{cases}$$

Among those cylinders given by Equation (3.18), the probability that their axes are located at a distance between z_c and $z_c + dz_c$ from the x-y plane is

$$\begin{cases} \dfrac{dz_c}{2\sqrt{(\frac{\ell}{2})^2 - (\frac{r_1 \sin\theta}{2})^2}} & \text{if } |z_c| \leq \sqrt{(\frac{\ell}{2})^2 - (\frac{r_1\sin\theta}{2})^2} \\ 0 & \text{otherwise} \end{cases}$$

Therefore

$$\gamma_2 = 2\int_{r_1}^{\infty}\int_0^{\pi/2}\int_0^{\sqrt{(\frac{\ell}{2})^2-(\frac{r_1\sin\theta}{2})^2}} \left(\frac{2\sqrt{(\frac{\ell}{2})^2 - z_c^2}}{\sin\theta} - r_1\right) g(\ell)\sin^2\theta\, dz_c\, d\theta\, d\ell$$

$$+ 2\int_0^{r_1}\int_0^{\sin^{-1}\frac{\ell}{r_1}}\int_0^{\sqrt{(\frac{\ell}{2})^2-(\frac{r_1\sin\theta}{2})^2}} \left(\frac{2\sqrt{(\frac{\ell}{2})^2 - z_c^2}}{\sin\theta} - r_1\right) g(\ell)\sin^2\theta\, dz_c\, d\theta\, d\ell$$

$$= 2\int_{r_1}^{\infty}\int_0^{\pi/2} (\tfrac{\ell}{2})^2 g(\ell)\left[\sin\theta \sin^{-1}\sqrt{1-(\tfrac{r_1\sin\theta}{\ell})^2} - \tfrac{r_1}{\ell}\sin^2\theta\sqrt{1-(\tfrac{r_1\sin\theta}{\ell})^2}\right] d\theta\, d\ell$$

$$+ 2\int_0^{r_1}\int_0^{\sin^{-1}\frac{\ell}{r_1}} (\tfrac{\ell}{2})^2 g(\ell)\left[\sin\theta \sin^{-1}\sqrt{1-(\tfrac{r_1\sin\theta}{\ell})^2} - \tfrac{r_1}{\ell}\sin^2\theta\sqrt{1-(\tfrac{r_1\sin\theta}{\ell})^2}\right] d\theta\, d\ell$$

$$= \int_{r_1}^{\infty} \tfrac{\ell^2}{2} g(\ell)\left[\tfrac{\pi}{2} - \tfrac{\pi}{2}\tfrac{r_1}{\ell} + O(\tfrac{r_1}{\ell})^3\right] d\ell + \int_0^{r_1} \tfrac{\ell^2}{2} g(\ell)\left[(\tfrac{\pi}{4} - \tfrac{2}{3})(\tfrac{\ell}{r_1})^2 + O(\tfrac{\ell}{r_1})^4\right] d\ell$$

$$= \int_0^{\infty} \tfrac{\ell^2}{2} g(\ell)\left(\tfrac{\pi}{2} - \tfrac{\pi}{2}\tfrac{r_1}{\ell}\right) d\ell + O\left(L^{r_1} r_1^3 \langle\tfrac{1}{\ell}\rangle^{r_1}\right) +$$

$$+ \int_0^{r_1} \tfrac{\ell^2}{2} g(\ell)\left[-\tfrac{\pi}{2} + \tfrac{\pi}{2}\tfrac{r_1}{\ell} + O(\tfrac{\ell}{r_1})^2\right] d\ell$$

$$= \tfrac{\pi}{4} L\left(\langle\ell^2\rangle - r_1\langle\ell\rangle\right) + O\left(L^{r_1} r_1^3 \langle\tfrac{1}{\ell}\rangle^{r_1}\right)$$

$$+ \tfrac{\pi}{4} L_{r_1}\left[r_1\langle\ell\rangle_{r_1} - \langle\ell^2\rangle_{r_1} + O\left(\frac{\langle\ell^4\rangle_{r_1}}{r_1^2}\right)\right]$$

and with Equations (3.7) and (3.8)

$$\frac{\gamma_2}{\gamma} = 1 - \frac{r_1}{\langle w \rangle} + O\left(\frac{L^{r_1}}{L} \frac{r_1^3}{\langle l^2 \rangle} \left\langle \frac{1}{l} \right\rangle^{r_1} \right) + \frac{L_{r_1} \left[r_1 \langle l \rangle_{r_1} - \langle l^2 \rangle_{r_1} + O\left(\frac{\langle l^4 \rangle_{r_1}}{r_1^2} \right) \right]}{L \langle l^2 \rangle}$$

$$= 1 - \frac{r_1}{\langle w \rangle} + C_5(r_1) \qquad (3.20)$$

(B) Two hot-wires separated in y-direction with distance r_2.

As shown in Sketch 8, a cylinder is convected along the x-axis with its axis at an angle θ to the x-axis and its projection on the y-z plane at an angle φ to the y-axis. The cylinder is cut by the y-z plane in an ellipse as shown in Sketch 9. The ellipse will move along the line AB with velocity $U \tan\theta$ as the cylinder is convected with velocity U along the x-axis. The probability that unit length of this cylinder hits both wires simultaneously equals the area, on the y-z plane, in which the middle point of the axis of this

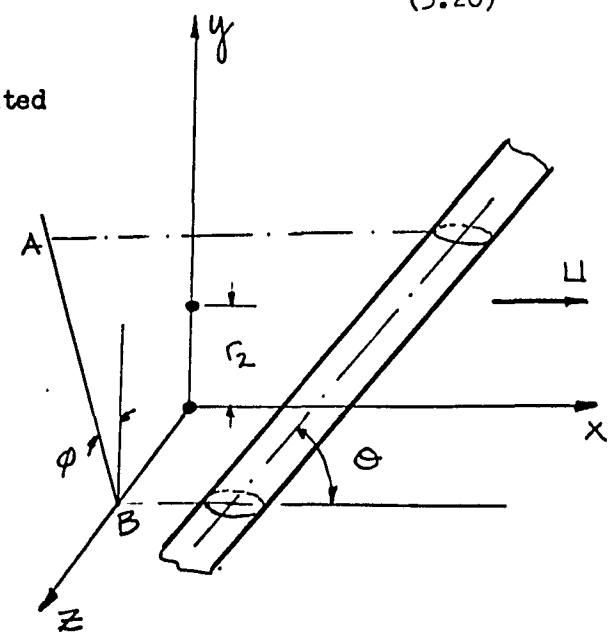

Sketch 8

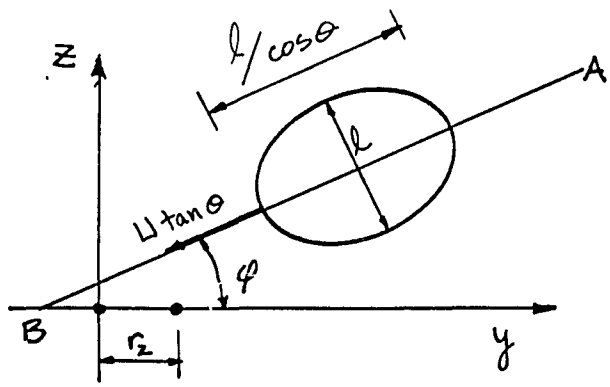

Sketch 9

section of the cylinder may go through and still hit both wires. This area is a rectangle of length $\sin\theta$ along AB direction and width $l - r_2\sin\varphi - E(\theta,\varphi,r_2,l)$. Then the probability is

$$\sin\theta\left[(l-r_2\sin\varphi) - E(\theta,\varphi,r_2,l)\right] \cdot \text{unit length/ unit area}$$

The width of $l-r_2\sin\varphi$ is the range in which the axis of the cylinder may shift in the direction perpendicular to AB and still hit both wires. The correction term E subtracts the end parts of $l-r_2\sin\varphi$, within which the cylinder axis may be located but such that the time intervals for each wire being inside the cylinder do not overlap, i.e., the cylinder hits both wires, but not simultaneously. E is a maximum at $\theta = 0$, $\varphi = 0$ or π, at which

$$E_{max} = O\left(l\,\frac{r_2^2}{l^2}\right)$$

and, for $\theta = 0$

$$E = 0$$

if $\varphi \geq \sin^{-1}\frac{r_2}{l}$

or $\pi-\varphi \geq \sin^{-1}\frac{r_2}{l}$

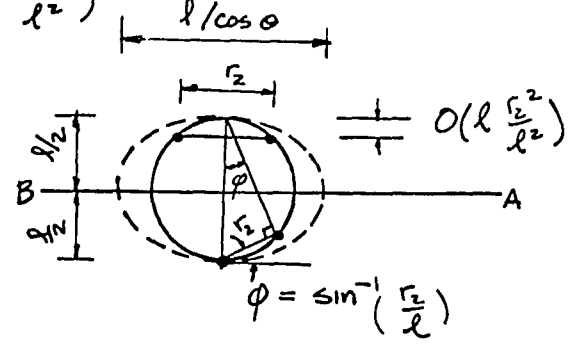

Sketch 10

Then the contribution from the integration of E is at least of the order of $\frac{r_2^3}{\langle l^2\rangle}$.

Since the orientation of cylinders is assumed to be statistically isotropic, the probability density of θ is

$$\begin{cases} \sin\theta & 0 \leq \theta \leq \pi/2 \\ 0 & \text{otherwise} \end{cases}$$

and the probability density of φ is

$$\begin{cases} 1/\pi & 0 \le \varphi \le \pi \\ 0 & \text{otherwise} \end{cases}$$

The expected number of cylinders hitting both wires simultaneously, with diameters between ℓ and $\ell+d\ell$, or orientation angles between θ and $\theta+d\theta$, φ and $\varphi+d\varphi$, is

$$\frac{1}{\pi} g(\ell) \sin^2\theta \,(\ell - r_2 \sin\varphi)\, d\varphi\, d\theta\, d\ell \quad + \text{higher order term}$$

for $0 \le \theta \le \frac{\pi}{2}$ and $\begin{cases} 0 \le \varphi \le \pi & \text{if } \ell \ge r_2 \\ \varphi \le \sin^{-1}\frac{\ell}{r_2} \text{ or } \pi-\varphi \le \sin^{-1}\frac{\ell}{r_2} & \text{if } \ell \le r_2 \end{cases}$

Therefore

$$m_2 = \int_{r_2}^{\infty}\int_0^{\pi}\int_0^{\pi/2} \frac{1}{\pi} g(\ell) \sin^2\theta\,(\ell - r_2\sin\varphi)\, d\theta\, d\varphi\, d\ell$$
$$+ 2\int_0^{r_2}\int_0^{\sin^{-1}\ell/r_2}\int_0^{\pi/2} \frac{1}{\pi} g(\ell)\sin^2\theta\,(\ell - r_2\sin\varphi)\, d\theta\, d\varphi\, d\ell + O\left(L\left\langle\frac{1}{\ell^2}\right\rangle r_2^3\right)$$

$$= \int_{r_2}^{\infty}\int_0^{\pi} \frac{1}{4} g(\ell)\,(\ell - r_2\sin\varphi)\, d\varphi\, d\ell$$
$$+ \frac{1}{2}\int_0^{r_2}\int_0^{\sin^{-1}\ell/r_2} g(\ell)\,(\ell - r_2\sin\varphi)\, d\varphi\, d\ell + O\left(L\left\langle\frac{1}{\ell^2}\right\rangle r_2^3\right)$$

$$= \frac{1}{4}\int_{r_2}^{\infty} g(\ell)\,(\pi\ell - 2r_2)\, d\ell$$
$$+ \frac{1}{2}\int_0^{r_2} g(\ell)\left[\ell \sin^{-1}\frac{\ell}{r_2} - r_2 + r_2\sqrt{1-\left(\frac{\ell}{r_2}\right)^2}\right] d\ell$$
$$+ O\left(L\left\langle\frac{1}{\ell^2}\right\rangle r_2^3\right)$$

$$m_2 = \frac{1}{4}\int_0^{\infty} g(\ell)(\pi\ell - 2r_2)\,d\ell + \frac{1}{2}\int_0^{r_2} g(\ell)\left[-\frac{1}{2}\pi\ell + r_2 + \frac{\ell^2}{r_2} - \frac{1}{2}\frac{\ell^2}{r_2} + O\left(\frac{\ell^4}{r_2^3}\right)\right]d\ell + O\left(L\left\langle\frac{1}{\ell^2}\right\rangle r_2^3\right)$$

$$= \frac{\pi}{4}L\langle\ell\rangle - \frac{r_2}{2}L + \frac{1}{4}L_{r_2}\left[2r_2 - \pi\langle\ell\rangle_{r_2} + O\left(\frac{\langle\ell^2\rangle_{r_2}}{r_2}\right)\right] + O\left(L\left\langle\frac{1}{\ell^2}\right\rangle r_2^3\right)$$

and with Equations (3.6) and (3.8)

$$\frac{m_2}{m} = 1 - \frac{2}{\pi}\frac{\langle\ell^2\rangle}{\langle\ell\rangle^2}\frac{r_2}{\langle W\rangle} + \frac{L_{r_2}\left[\frac{2}{\pi}r_2 - \langle\ell\rangle_{r_2} + O\left(\frac{\langle\ell^2\rangle_{r_2}}{r_2}\right)\right]}{L\langle\ell\rangle} + O\left(\left\langle\frac{1}{\ell^2}\right\rangle\frac{r_2^3}{\langle\ell\rangle}\right)$$

$$= 1 - \frac{2}{\pi}\frac{\langle\ell^2\rangle}{\langle\ell\rangle^2}\frac{r_2}{\langle W\rangle} + C_6(r_2) \qquad (3.21)$$

(3) Slab Model

(A) Two hot-wires separated in the x-direction with distance r_1 .

If a second hot-wire is placed at $(r_1,0,0)$ in Sketch 3, the probability that unit area of a slab is detected by both wires simultaneously equals the projected area. on the y-z plane, of that part of this unit slab with dimension in the x-direction greater than r_1 , i.e.

$$\begin{cases} \cos\theta & \text{if } w \geq r_1 \text{ i.e. } \begin{cases} \ell \geq r_1 \,, & 0 \leq \theta \leq \pi/2 \quad \text{or} \\ \ell \leq r_1 \,, & \cos^{-1}\frac{\ell}{r_1} \leq \theta \leq \frac{\pi}{2} \end{cases} \\ 0 & \text{otherwise} \end{cases}$$

Since the orientation of slabs is assumed to be statistically isotropic, the probability density of angle θ is the measure of relative solid angle giving θ, i.e.

$$\begin{cases} \sin\theta & 0 \leq \theta \leq \pi/2 \\ 0 & \text{otherwise} \end{cases}$$

Therefore

$$m_2 = \int_{r_1}^{\infty}\int_0^{\pi/2} \sin\theta\cos\theta\, g(\ell)\, d\theta\, d\ell + \int_0^{r_1}\int_{\cos^{-1}\frac{\ell}{r_1}}^{\pi/2} \sin\theta\cos\theta\, g(\ell)\, d\theta\, d\ell$$

$$= \int_{r_1}^{\infty} \tfrac{1}{2} g(\ell)\, d\ell + \int_0^{r_1} \tfrac{1}{2}\frac{\ell^2}{r_1^2} g(\ell)\, d\ell$$

$$= \int_0^{\infty} \tfrac{1}{2} g(\ell)\, d\ell + \int_0^{r_1} \tfrac{1}{2} g(\ell)\left[-1 + \frac{\ell^2}{r_1^2}\right] d\ell$$

$$= \tfrac{1}{2} S - \tfrac{1}{2} S_{r_1}\left(1 - \frac{\langle \ell^2 \rangle_{r_1}}{r_1^2}\right)$$

and, with Equation (3.10)

$$\frac{m_2}{m} = 1 - \frac{S_{r_1}}{S}\left(1 - \frac{\langle \ell^2 \rangle_{r_1}}{r_1^2}\right)$$

$$= 1 - C_7(r_1) \qquad (3.22)$$

Analogous to the spherical model, the corresponding W_2 for both hot-wires inside the slab is

$$W_2 = \begin{cases} W - r_1 = \dfrac{\ell}{\cos\theta} - r_1 & \text{if } \ell \geq r_1 \text{ or } \ell \leq r_1,\ \cos^{-1}\dfrac{\ell}{r_1} \leq \theta \leq \dfrac{\pi}{2} \\ 0 & \text{otherwise} \end{cases}$$

Therefore

$$\gamma_2 = \int_{r_1}^{\infty}\int_0^{\pi/2} \left(\frac{\ell}{\cos\theta} - r_1\right)\cos\theta\sin\theta\, g(\ell)\, d\theta\, d\ell + \int_0^{r_1}\int_{\cos^{-1}\frac{\ell}{r_1}}^{\pi/2} \left(\frac{\ell}{\cos\theta} - r_1\right)\cos\theta\sin\theta\, g(\ell)\, d\theta\, d\ell$$

$$= \int_{r_1}^{\infty} g(\ell)\left(\ell - \frac{r_1}{2}\right)d\ell + \int_0^{r_1} g(\ell)\left(\frac{\ell^2}{r_1} - \frac{1}{2}\frac{\ell^2}{r_1}\right)d\ell$$

$$= \int_0^{\infty} g(\ell)\left(\ell - \frac{r_1}{2}\right)d\ell + \int_0^{r_1} g(\ell)\left(-\ell + \frac{r_1}{2} + \frac{1}{2}\frac{\ell^2}{r_1}\right)d\ell$$

$$= S\langle\ell\rangle - \frac{r_1}{2}S + S_{r_1}\left(\frac{r_1}{2} - \langle\ell\rangle_{r_1} + \frac{1}{2}\frac{\langle\ell^2\rangle_{r_1}}{r_1}\right)$$

and, with Equations (3.11) and (3.12)

$$\frac{\gamma_2}{\gamma} = 1 - \frac{r_1}{\langle W\rangle} + \frac{S_{r_1}\left(\frac{r_1}{2} - \langle\ell\rangle_{r_1} + \frac{1}{2}\frac{\langle\ell^2\rangle_{r_1}}{r_1}\right)}{S\langle\ell\rangle}$$

$$= 1 - \frac{r_1}{\langle W\rangle} + C_8(r_1) \qquad (3.23)$$

(B) Two hot-wires separated in the y-direction

As shown in Sketch 11, a slab is convected along the x-axis with its normal at an angle θ to the x-axis and its projection on the y-z plane at an angle φ to the y-axis. The slab is cut in a strip by the y-z plane as shown in Sketch 12. If the slab hits the wire at origin, the probability that it hits both wires simultaneously is

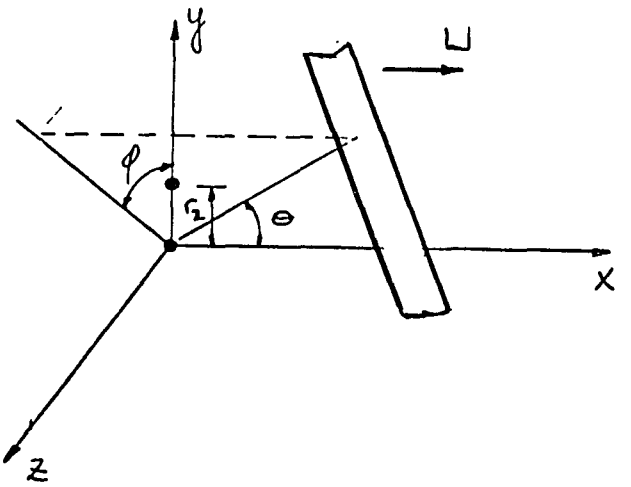

Sketch 11

$$\begin{cases} 1 & \text{if } \dfrac{\ell}{\sin\theta|\cos\varphi|} \geq r_2 \\ 0 & \text{if } \dfrac{\ell}{\sin\theta|\cos\varphi|} < r_2 \end{cases}$$

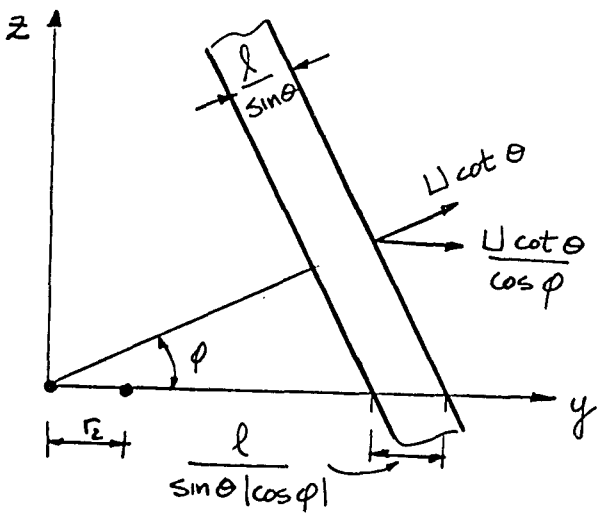

Sketch 12

i.e.,

$$\begin{cases} 1 & \text{if} \quad \text{(i)} \ \ell \geq r_2, \quad 0 \leq \theta \leq \frac{\pi}{2}, \quad 0 \leq \varphi \leq \pi \\ & \quad \text{(ii)} \ \ell < r_2, \quad 0 \leq \theta \leq \sin^{-1}\frac{\ell}{r_2}, \quad 0 \leq \varphi \leq \pi \\ & \quad \text{(iii)} \ \ell < r_2, \quad \theta > \sin^{-1}\ell/r_2, \quad \cos^{-1}\frac{\ell}{r_2\sin\theta} < \varphi < \pi - \cos^{-1}\frac{\ell}{r_2\sin\theta} \\ 0 & \quad \text{otherwise} \end{cases}$$

Similar to Equation (3.9), the expected number of slabs hitting one wire, with thickness between ℓ and $\ell + d\ell$, orientation angles between θ and $\theta + d\theta$, φ and $\varphi + d\varphi$, is

$$\frac{1}{\pi} \sin\theta \cos\theta \, g(\ell) \, d\varphi \, d\theta \, d\ell$$

Therefore

$$\begin{aligned} m_2 = & \int_{r_2}^{\infty} \int_0^{\pi/2} \int_0^{\pi} \frac{1}{\pi} \sin\theta \cos\theta \, g(\ell) \, d\varphi \, d\theta \, d\ell \\ & + \int_0^{r_2} \int_0^{\sin^{-1} \ell/r_2} \int_0^{\pi} \frac{1}{\pi} \sin\theta \cos\theta \, g(\ell) \, d\varphi \, d\theta \, d\ell \\ & + 2 \int_0^{r_2} \int_{\sin^{-1} \ell/r_2}^{\pi/2} \int_{\cos^{-1} \frac{\ell}{r_2 \sin\theta}}^{\pi/2} \frac{1}{\pi} \sin\theta \cos\theta \, g(\ell) \, d\varphi \, d\theta \, d\ell \end{aligned}$$

$$= \int_{r_2}^{\infty} \frac{1}{2} g(\ell) \, d\ell + \int_0^{r_2} \int_0^{\sin^{-1} \ell/r_2} \sin\theta \cos\theta \, g(\ell) \, d\theta \, d\ell$$
$$+ \int_0^{r_2} \int_{\sin^{-1} \ell/r_2}^{\pi/2} \frac{1}{\pi} g(\ell) \left[\pi - 2 \cos^{-1} \frac{\ell}{r_2 \sin\theta} \right] \sin\theta \cos\theta \, d\theta \, d\ell$$

$$= \int_0^{\infty} \frac{1}{2} g(\ell) \, d\ell - \int_0^{r_2} \frac{1}{2} g(\ell) \, d\ell + \int_0^{r_2} \frac{1}{2} \left(\frac{\ell}{r_2} \right)^2 g(\ell) \, d\ell$$
$$+ \int_0^{r_2} \int_{\sin^{-1} \frac{\ell}{r_2}}^{\pi/2} \frac{1}{\pi} g(\ell) \, 2 \left[\frac{\ell}{r_2 \sin\theta} + O\left(\frac{\ell}{r_2 \sin\theta} \right)^3 \right] \sin\theta \cos\theta \, d\theta \, d\ell$$

$$= \frac{1}{2} S - \frac{1}{2} \int_0^{r_2} g(\ell) \left[1 - \left(\frac{\ell}{r_2} \right)^2 \right] d\ell$$
$$+ \int_0^{r_2} \frac{2}{\pi} g(\ell) \, \frac{\ell}{r_2} \left[1 - \frac{\ell}{r_2} + O\left(\frac{\ell}{r_2} \right)^2 \right] d\ell$$

$$= \frac{1}{2} S - \frac{1}{2} S_{r_2} \left[1 - \frac{4}{\pi} \frac{\langle \ell \rangle_{r_2}}{r_2} + \left(\frac{4}{\pi} - 1 \right) \frac{\langle \ell^2 \rangle_{r_2}}{r_2^2} + O\left(\frac{\langle \ell^3 \rangle_{r_2}}{r_2^3} \right) \right.$$

and, with Equation (3.10)

$$\frac{m_2}{m} = 1 - \frac{S_{r_2}}{S}\left[1 - \frac{4}{\pi}\frac{\langle \ell \rangle_{r_2}}{r_2} + \left(\frac{4}{\pi} - 1\right)\frac{\langle \ell^2 \rangle_{r_2}}{r_2^2} + O\left(\frac{\langle \ell^3 \rangle_{r_2}}{r_2^3}\right)\right]$$

$$= 1 - C_q(r_2) \qquad (3.24)$$

IV. EXPERIMENTAL RESULTS

4.1 Visual Observation of Fine-Structure Intermittency

The direct visual observation of over-all turbulence structure has been somewhat successful in a smoke tunnel or water channel (with dye or tiny bubbles). Nevertheless, present flow-visualization techniques are inadequate for a study of the fine-scale structure of turbulent fluctuations, since these techniques fail to extract fine-scale components and reveal them. Also they have not yet proved viable at the relatively high speeds necessary to generate turbulence whose Reynolds number is large enough to have "internal intermittency" of the fine-structure. An indirect visualization may be achieved by electronically examining narrow-band frequency components of the over-all turbulent signal.

Figure 21 shows typical oscillograms of band-pass and high-pass signals from a hot-wire placed in a grid-generated turbulent flow field ($R_\lambda = 110$). The low frequency signal is more or less uniformly distributed in time, while the high frequency signals appear to be intermittent. With Taylor's hypothesis, frequency is proportional to wave number, so the high frequency signals correspond to the velocity fluctuations associated with the fine-scale components of motion, and the temporal variation of a signal from a fixed hot-wire as it is convected past the hot-wire by the mean flow corresponds to the spatial variation of the turbulence pattern. Therefore, the intermittency of high frequency signal in time domain implies the localization of the fine-structure in space domain. The

time interval when the high frequency signal is "zero" corresponds to the time when the hot-wire is in a spatial region in which the fine-scale components are negligible.

Figure 22 shows the oscillograms of the total turbulent signal and of its first and second time derivatives. The derivative signals emphasize the fine-scale components, and their crest factors appear to increase as the order of derivative increases. However, they do not appear intermittent as the high frequency signal does. This is because the Reynolds number of the turbulence is not high enough to remove the spectrum of derivative signals far away from energy containing eddies, which is more or less uniformly distributed in space. Since the viscous dissipation of turbulent kinetic energy occurs primarily in the fine-structure, the fine-structure intermittency implies that the energy dissipation (or the first derivative) will appear intermittent if the Reynolds number of the turbulent flow is high enough such that the spectrum of energy dissipation decouples itself from energy spectrum. See, for example, the high Reynolds number flows of Sheih[5], of Stegen and Gibson[6], and of Grant, Stewart and Moilliet.[35]

4.2 Flatness Factor

The flatness factor F of a random variable e is defined as

$$F \equiv \frac{\langle e^4 \rangle}{\langle e^2 \rangle^2} = \frac{\int_{-\infty}^{+\infty} e^4 P(e)\, de}{\left\{ \int_{-\infty}^{+\infty} e^2 P(e)\, de \right\}^2} \qquad (4.1)$$

where $P(e)$ is the probability density of e . Since the fourth moment depends heavily on the large values of e , the flatness factor is a measure of the relative extent of the skirts of the probability density curve. A random variable with normal density has a flatness factor of 3.0 and $(F-3.0)$ for an arbitrary random variable is termed the "kurtosis." The roughly normal variable whose probability density function is more peaked in the neighborhood of the mean than is a normal density of the same standard deviation will have positive kurtosis.

As seen in Equation (4.1), a probability density function will uniquely determine the flatness factor, but the converse is not true. Though an intermittent variable is likely to have a large flatness factor, a large flatness factor does not necessarily imply intermittency. Therefore, a flatness factor can be used to indicate the degree of intermittency of a random variable only if it is known by other observations that the variable is intermittent. Batchelor and Townsend[1] suggested a relation between flatness factor and intermittency factor

$$\gamma = \frac{3.0}{F} \tag{4.2}$$

by assuming the intermittent variable varies with a normal probability distribution for a fraction γ of the total time, and is zero for the remainder of the time.

Having observed the fine-structure intermittency on the oscillograms as described in the previous section, the flatness factors of the velocity derivatives and band-pass signals were measured to offer

an indication to the degree of intermittency and the degree of deviation from normal distribution. The flatness factors of the velocity fluctuations u were also measured and found to be quite close to 3.0 as were found before by other investigators.

The noise spectrum of a thermally compensated hot-wire signal increases with frequency, while the energy spectrum of the turbulence decreases sharply with increasing frequency in the high frequency range. Differentiation accentuates the high frequencies present in the total signal, so the differentiation tends to reduce the signal-to-noise ratio. Therefore some kind of low-pass filter is necessary to cut off the high frequencies at which the signal-to-noise ratio is smallest.

The effect of high cut-off frequency on the flatness factors of the first and the second derivatives of the signal are shown in Figures 23 and 24, respectively. The flatness factors tend to increase with increasing cut-off frequency, and the rate of increase is higher for the second derivative than for the first, and for the higher Reynolds number flow; both differentiation and R_λ increase give relatively more high frequency "energy." This tendency agrees with the fact that the flatness factors of band-pass signals increase with frequency, to be discussed later. If the cut-off frequency is too high, however, the output includes more additional noise than signal and the flatness factor begins to level off, since the noise is approximately normal. The flatness factor therefore will eventually decrease as the cut-off frequency is raised to the value where the filter output includes more and more noise, with its flatness

factor of about 3.0. This leveling-off tendency is observed particularly in the first derivative signals of lower Reynolds number flows, which have less high frequency "energy."

The flatness factors of the first and the second derivatives were measured and are shown in Figures 25 and 26 as functions of R_λ, which ranged from 12 in a grid-generated turbulence to 830 on the axis of a round jet. To be consistent for differing Reynolds number flows, the cut-off frequencies of the filters were set at the frequencies of the Kolmogorov microscales.* This cut-off frequency is much higher than the frequency at which the peak of the spectrum of the derivative signal is located. Some measurements by other investigators are included in Figures 25 and 26 for comparison. Since Batchelor and Townsend[1] did not give the cut-off frequency of their filter, an effort was made to discover their procedure and to adjust their second derivative data to the values consistent with cut-off at f.* Their first derivative data were not adjusted because the variation of the flatness factor is comparatively small for low Reynolds number flows, as shown by Figure 23. By repetition of their experiments, we established the strong likelihood that they used a single cut-off frequency for all cases. The present flatness factor data were plotted as a function of cut-off frequency, and the flatness factors at various cut-off fre-

---

*i.e., the frequency $f^* \equiv U/2\pi\eta$ corresponding to the convection of η-scale fine-structure past the hot-wire $\eta \equiv (\nu^3/\varepsilon)^{1/4}$.

quencies (for fixed R_λ's) were obtained by extrapolation or interpolation. The flatness factors as a function of R_λ , with various constant cut-off frequencies, were plotted and compared with the Batchelor and Townsend data. The one with cut-off frequency at 3.5 kHz was found to agree best with their data and is shown in Figure 27. The upper line is a plot of the "correction" factor, i.e., the ratio of the flatness factors with cut-off frequency at f* to those with cut-off at 3.5 kHz. The "corrected" Batchelor and Townsend data were obtained by multiplying their reported values by correction factors at the appropriate Reynolds numbers.

Batchelor and Townsend[1,9] inferred from the original Kolmogorov similarity hypothesis that the limiting values of the flatness factors of velocity derivatives are independent of the large-scale properties of the turbulence and should reach universal constant values at large enough Reynolds numbers. Figure 25 shows that the flatness factor of the first derivative behaves like $R_\lambda^{0.2}$ at Reynolds number below 200, followed by a transition zone up to $R_\lambda \simeq 500$, and then behaves like $R_\lambda^{0.62}$ instead of leveling off. In Figure 26, the flatness factor of the second derivative behaves like $R_\lambda^{0.25}$ up to $R_\lambda \simeq 100$, and like $R_\lambda^{0.75}$ for $R_\lambda \geq 300$. Apparently, the flatness factors of the derivatives show no sign of approaching constants at Reynolds numbers R_λ of the order of thousands, which is believed to be high enough for the universal similarity hypothesis to apply.

In fact, it is doubtful that the flatness factors of the derivatives are determined wholly by the large wave-number components of

the turbulence. Suppose we have a turbulence with large enough Reynolds number that the derivative signal appears intermittent (it was observed that the second derivative signal at $R_\lambda = 830$ appeared intermittent), then the flatness factor of this intermittent signal depends in part on the signal durations over which the signal is zero. But the statistics of these durations are associated with the scale of the energy-containing eddies, not the smallest eddies.

Corrsin[19] and Tennekes[20] explored some consequences of simple models which included intermittency of the fine-structure, and estimated the consequent dependence of the flatness factor of the first derivative on Reynolds number to be $\sim R_\lambda^{1.5}$ and $\sim R_\lambda$, respectively. The result of this experiment shows a weaker dependence.

The Yaglom and Gurvich[18] model with log-normal distribution of positive random variables predicts that

$$\frac{\langle \phi^K \rangle}{\langle \phi \rangle^K} \sim R_\lambda^{\frac{3}{4}\mu K(K-1)} \tag{4.3}$$

where ϕ is a non-negative quantity governed by fine-scale components, μ is a universal constant estimated to be 0.4 by Yaglom and Gurvich from measured spectra of $(\partial u/\partial t)^2$ and $(\partial w/\partial t)^2$. If we take $\phi = \left(\frac{\partial u}{\partial t}\right)^2$ and $K = 2$, we get the flatness factors of the derivatives proportional to $R_\lambda^{0.6}$, which agrees with the high Reynolds number data of the first derivative signal.

The flatness factors of band-pass signals were measured in the grid-generated turbulence at $R_\lambda = 110$ and 86.5. Figure 28 shows the effect of relative bandwidth on the flatness factors for a fixed mid-band frequency. The data were replotted in Figure 29 on a semi-log scale to accentuate the peakedness of the curves. All the curves peak around $\Delta f/f_m = 0.3$, and the higher the mid-band frequency, the more pronounced the peak is. For a given mid-band frequency, the flatness factor decreases as bandwidth increases from 0.3, since the greater bandwidth passes relatively more low frequency component which is essentially normal. When the bandwidth decreases from 0.3, its time constant increases up to a point where it is comparable with or larger than the time scale of the on-off cycle of the intermittent signal. In these cases, the filter performs some kind of weighted average on the signal and the flatness factor of the filter output decreases.* With a very narrow-band filter of bandwidth 6 Hz between -3db points, Hewlett Packard model 302A wave analyzer, it was found that the flatness factors of filtered signals were very close to 3.0 for all mid-band frequencies.

---

*It is generally found that any kind of "smoothing" of a non-normal stationary random variable tends to make it tend toward normality. In the limit of "infinite smoothing" this is analogous to the "Central Limit Theorem."[36] A more formal formulation of the "Central Limit Theorem" in this respect has been presented by J. L. Lumley in a seminar given in this Department of Mechanics on April 3, 1970.

To investigate the flatness factors of various frequency components, it is desirable to have a filter bandwidth as narrow as possible, but not so narrow that the time constant of the filter will play a smoothing role. It is seen in Figures 28 and 29 that the filter with bandwidth giving "peak" flatness factor plays a significant smoothing role. Therefore, we chose a slightly wider bandwidth, $\Delta f / f_m = 0.52$, which is the narrowest bandwidth of the Krohn-Hite filter. The flatness factors of fixed bandwidth band-passed signals are shown in Figure 30 as functions of mid-band frequency, f_m / f^* . The flatness factors start with 3.0 at low f_m and monotonically increase with f_m . The fall-off at very high f_m is due to the high noise-to-signal ratio at high frequency. The flatness factors of band-passed signals of normal (Gaussian) random noise are also shown in Figures 28 and 30; they are approximately 3.0, independent of both bandwidth and mid-band frequency.

4.3 Probability Density and Distribution Function

Let $P(e)$ be the probability density function of a random variable e ; then by definition,

$$\int_{-\infty}^{\infty} P(e)\, de = 1 \tag{4.4}$$

A conventional way to nondimensionalize the probability density is by transforming Equation (4.4) into

$$\int_{-\infty}^{\infty} \langle e^2 \rangle^{1/2} P(e)\, d\left(\frac{e}{\langle e^2 \rangle^{1/2}}\right) = \int_{-\infty}^{\infty} P_n(e_n)\, de_n = 1 \tag{4.5}$$

Thus, the suitable non-dimensional variables are

$$P_n(e_n) \equiv \langle e^2 \rangle^{1/2} P(e)$$

$$\text{and} \qquad e_n \equiv e / \langle e^2 \rangle^{1/2} \tag{4.6}$$

In Figures 31 and 32, the probability densities of u, $\frac{\partial u}{\partial t}$, and $\partial^2 u / \partial t^2$ in a grid-generated turbulence ($R_\lambda = 72$) and on the axis of a round jet ($R_\lambda = 830$) were plotted in these non-dimensional variables. The normal (Gaussian) density,

$$P_n(e_n) = \frac{1}{\sqrt{2\pi}} \exp\left(-\frac{e_n^2}{2}\right) , \tag{4.7}$$

was also plotted for comparison. We see that the higher the order of the derivative, the more its probability density deviates from the normal density, and that the deviation is more pronounced at higher Reynolds numbers. In all cases in which the probability densities deviate from normality, they all deviate in the same manner, tending to have higher probability than the normal curve in the neighborhood of zero e and at very large values of $e / \langle e^2 \rangle^{1/2}$, and to have lower probability at the intermediate values. This is a feature that an intermittent signal should have. If it were exactly zero during the "off" periods, there would be a Dirac function at $e = 0$.

Since the probability density was obtained by numerically differentiating the measured probability distribution, the accuracy is poor at large values of e, where the probability density is small.

It is difficult to calculate accurately the higher moments, which weigh heavily the large values of e. No report on the higher moments will be made based on the probability density data.

Since the directly measured data are the probability distributions, it is easier and more accurate to compare these with the normal distribution function. The probability distribution functions

$$\text{Prob}\,(e_n \leq a) \equiv \int_{-\infty}^{a} P_n(e_n)\, de_n \qquad (4.7)$$

were plotted in a normal probability scale, for which the normal distribution function would appear as a straight line.

The probability distributions of u, $\partial u/\partial t$ and $\partial^2 u/\partial t^2$ at $R_\lambda = 72$ and 830 are shown in Figures 33 and 34. We see that the u's are nearly normal, the derivatives less so. The higher order derivative deviates more from normality.

To demonstrate the variation with Reynolds number, probability distributions of $\partial^2 u/\partial t^2$ at various Reynolds numbers are shown in Figure 35. $\partial^2 u/\partial t^2$ deviates more and more from normality as Reynolds number increases.

Next the probability distribution of various frequency components (via band-pass filter) were measured in grid-generated turbulence at $R_\lambda = 110$. They are compared with normal distribution in Figure 36, which shows that the low frequency part of the signal has a normal distribution, while the higher frequency parts do not. The deviation from normality increases as frequency increases. The probability

distribution of the signal from a high-pass Butterworth filter* is shown in Figure 37, which does not agree with normal distribution at all.

To test Kolmogorov's[14] conjecture and Gurvich and Yaglom's[18] prediction that a non-negative quantity governed by the fine-structure of the motion has a log-normal distribution at large Reynolds number, the probability distribution of ϵ^2 was computed from that of ϵ, where ϵ is velocity fluctuations, velocity derivatives, or band-pass signals. If $P_n(\epsilon_n)$ is the probability density of ϵ_n, the probability density and distribution of ϵ_n^2 are respectively,

$$P_n'(\epsilon_n^2) = \left[P_n(-\epsilon_n) + P_n(\epsilon_n)\right] \frac{1}{2|\epsilon_n|} \tag{4.8}$$

and

$$\begin{aligned} \text{Prob}(\epsilon_n^2 \le a^2) &\equiv \int_0^{a^2} P_n'(\epsilon_n^2)\, d\epsilon_n^2 \\ &= \int_0^a \left[P_n(-\epsilon_n) + P_n(\epsilon_n)\right] d\epsilon_n \qquad (4.9) \\ &= \text{Prob}(\epsilon_n \le a) - \text{Prob}(\epsilon_n \le -a) \end{aligned}$$

where $a \ge 0$. The probability distribution

---

*Actually, the cascade of Butterworth filter with all the amplifiers constitutes a band-pass filter. But the high cut-off frequency is so high that the energy spectrum is negligibly small there. Therefore, the band-pass filter is essentially a high-pass filter.

$Prob\,(e_n^2 \leq a^2)$ was plotted on a normal probability scale against $\ln a^2$, so that log-normal distribution functions would appear as straight lines.

The probability distributions of u^2, $(\partial u/\partial t)^2$, and $(\partial^2 u/\partial t^2)^2$ at R_λ = 72 and 830 are shown in Figures 38 and 39. The results suggest that the higher the order of derivative, the better it agrees with log-normality. $(\partial^2 u/\partial t^2)^2$ agrees well over the distribution range 0.35 to 0.9.

To look for a variation with Reynolds number, the probability distributions of $(\partial^2 u/\partial t^2)^2$ at various Reynolds numbers are shown in Figure 40. Evidently the distribution of $(\partial^2 u/\partial t^2)^2$ is approximated better by a log-normal distribution as Reynolds number increases.

The probability distributions of the squares of band-pass signals are presented in Figure 41. The results suggest that with higher mid-band frequency, the agreement with a log-normal distribution improves. The band-pass signal of mid-band frequency 6.3 kHz agrees with log-normal distribution quite well at high amplitude range. When the amplitude $e/\langle e^2\rangle^{1/2}$ is smaller than $\frac{1}{\sqrt{33}}$ $\left(\simeq\sqrt{\exp[-3.5]}\right)$ i.e., for distribution function less than 0.3, the distribution departs from log-normality. It should be pointed out that in the low amplitude range, electronic noise may contribute appreciably, so the turbulence signal may be log-normal over a broader range of values than indicated by these measurements.

The probability distribution of the square of the high-pass signal from a Butterworth filter is shown in Figure 42. This too

agrees with a log-normal distribution except the low amplitude range.

4.4 Intermittency Characteristics

The intermittency characteristics of band-pass signals were measured in grid-generated turbulence and on the axes of round jets. Their dependences on Reynolds number were investigated. The bandwidth of the Krohn-Hite filter was set at $\Delta f / f_m = 0.52$ and the mid-band frequency at $f_m = f^*$. Two quantities were measured: γ, the intermittency factor, i.e., the fraction of space occupied by the fine-structure, and n, the average number of the fine-structure regions detected by the hot-wire per unit time. The average width $\langle W \rangle$ of the interception chord lines crossing fine-structure regions was calculated by the formula

$$\langle W \rangle = \frac{\gamma U}{n} \tag{4.10}$$

where U is the mean velocity. The intermittency factor γ and the ratio of $\langle W \rangle$ to the Kolmogorov microscale η are shown in Figure 43 as functions of R_λ. It is seen that both γ and $\langle W \rangle / \eta$ decrease monotonically with R_λ and seem to reach asymptotic values at R_λ of the order of several hundreds. This result implies that the relative volume of the fine-structure regions decreases with increasing Reynolds number.

In the grid-generated turbulence of $R_\lambda = 110$, the intermittency characteristics of band-pass signals were measured to investigate possible dependence on frequency, hence on wave-number, in the

light of the Taylor's hypothesis. The bandwidth of the filter was set at $\Delta f/f_m = 0.52$. The intermittency factor γ and the non-dimensional width $\langle W \rangle k_m$, where $k_m = 2\pi f_m/U$ are shown in Figure 44 as a function of f_m / f^*. $\langle W \rangle k_m$ is a measure of the ratio of an average linear dimension of these "narrow-band" fine-structure regions to the characteristic eddy sizes with which they are active. Both γ and $\langle W \rangle k_m$ decrease monotonically with increasing f_m / f^*. This means that the volume occupied by the eddies with size of the order of $1/k_m$ decreases as k_m increases, which is consistent with a suggestion by Batchelor and Townsend.*

Batchelor and Townsend[1] suggested Equation (4.2) for the relationship between the flatness factor and intermittency factor of an intermittent variable. γ and F of the band-pass signal ($\Delta f/f_m = 0.52$, $f_m = f^*$) from a grid-generated turbulence ($R_\lambda = 110$) were measured to be 0.58 and 13 respectively. This differs significantly from Equation (4.2) and suggests that the intermittent fine-structure signal does not vary with a normal distribution during the time interval when it is not zero.

4.5 Geometric Categorization of the Random Fine-Structure Regions

The flow field chosen for this study is a grid-generated turbulence homogeneously strained by a slight contraction to bring it closer to isotropy.[23] The grid is of 4-inch mesh size and the mean

---

*see Chapter I

velocity in the test section is 12.7 m/s. Measurements were made at 42 mesh lengths downstream of the grid, where the turbulent field has been found more or less isotropic and $R_\lambda = 110$. The measured one-dimensional spectrum function of u is shown in Figure 45.

To be able to infer the geometry of the fine-structure regions, a choice of fine-structure signal has to be made. A signal which is easy to obtain and has obvious physical meaning is the time derivative of the velocity fluctuations, which is related to strain-rate and energy dissipation. Unfortunately, a turbulent flow field with Reynolds number high enough to "decouple" the dissipation spectrum from the energy spectrum is not easy to obtain in the laboratory.*

In this investigation, four-pole Butterworth high-pass filters were used to extract the fine-structure signals. The filters have sharp enough low frequency cut-off (24 db/octave) to eliminate the large-scale signals from the output.

It is assumed in the analysis of Chapter III that both the overlap of the fine-structure regions and the probability that two separate regions hit two hot-wires simultaneously are negligible. To meet these assumptions it is desirable to have the fraction of space occupied by the fine-structure as small as possible, i.e., to have a filtered signal with small intermittency factor γ. If the intermittency factor is too small, however, the measurements of coincidence functions γ_2 and Γ_2 will be difficult and inaccurate. A compromise value of $\gamma = 0.2 \sim 0.4$ was chosen, and the cut-off

---

*see discussion in Section 4.1.

frequency of the high-ass filter was determined with the aid of the result of the intermittency measurements of band-pass signals described in Section 4.4. The energy spectrum of the filtered signal (Figure 46) has a peak at 3.5 kHz (Kolmogorov-scale frequency 5.9 kHz) which corresponds to a length scale $S_f = 2.26 \times 10^{-2}$ in.

The results of single probe measurements of the high-pass signal are

$$\gamma = 0.3 \qquad \Pi = 750/\text{sec}^{*} \qquad \langle W \rangle = 0.2 \text{ in}$$

A summary of the analytical results of Chapter III is the following:

(1) Single-Probe Analysis (Table 1)

	m	γ	$\langle W \rangle$
Spherical Model	$\frac{\pi}{4} N \langle \ell^2 \rangle$	$\frac{\pi}{6} N \langle \ell^3 \rangle$	$\frac{2}{3} \frac{\langle \ell^3 \rangle}{\langle \ell^2 \rangle}$
Cylindrical Model	$\frac{\pi}{4} L \langle \ell \rangle$	$\frac{\pi}{4} L \langle \ell^2 \rangle$	$\frac{\langle \ell^2 \rangle}{\langle \ell \rangle}$
Slab Model	$\frac{1}{2} S$	$S \langle \ell \rangle$	$2 \langle \ell \rangle$

(2) Two-Probe Analysis (Table 2)

	$\frac{m_2}{m} = \frac{n_2}{n}$	γ_2/γ
Spherical Model	$\begin{cases} 1 - \frac{4}{9} \frac{\langle \ell^3 \rangle^2}{\langle \ell^2 \rangle^3} \frac{r_1^2}{\langle W \rangle^2} + C_1(r_1) \\ 1 - \frac{8}{3\pi} \frac{\langle \ell \rangle \langle \ell^3 \rangle}{\langle \ell^2 \rangle^2} \frac{r_2}{\langle W \rangle} + C_3(r_2) \end{cases}$	$1 - \frac{r}{\langle W \rangle} + \frac{1}{2} \frac{r^3}{\langle \ell^3 \rangle} + C_2(r)$
Cylindrical Model	$\begin{cases} 1 - \frac{3}{8} \frac{\langle \ell^2 \rangle^2}{\langle \ell^3 \rangle} \langle \frac{1}{\ell} \rangle \frac{r_1^2}{\langle W \rangle^2} + C_4(r_1) \\ 1 - \frac{2}{\pi} \frac{\langle \ell^2 \rangle}{\langle \ell \rangle^2} \frac{r_2}{\langle W \rangle} + C_6(r_2) \end{cases}$	$1 - \frac{r}{\langle W \rangle} + C_5(r)$

*According to Corrsin's theorem,[32] for this value of Π the average surface area of the fine-structure regions inside a cubic inch of space is 6 in^2.

Slab Model $\begin{cases} 1 - C_7(r_1) \\ 1 - C_9(r_2) \end{cases}$ $\qquad 1 - \frac{r}{\langle W \rangle} + C_8(r)$

To compare these results with those of two-probe coincidence measurements, the restriction to $r < \langle \ell \rangle = O(\langle W \rangle)$ is necessary for the following reasons:

(1) to make the higher order terms of $r/\langle W \rangle$ in $C_i(r)$ negligible,

(2) to make terms in $C_i(r)$ involving the integration of $g(\ell)$ negligible; otherwise a specific functional form of $g(\ell)$ has to be known before the comparison can be made,

(3) to minimize the probability that two separate fine-structure regions hit two probes simultaneously.

A reasonable assumption for the behavior of $g(\ell)$ at small ℓ is

$$g(\ell) = 0 \quad , \quad \text{if } \ell \leq S_f \tag{4.11}$$

since it is necessary that the smallest dimension of fine-structure regions be at least as big as S_f, the size of eddies with which they are active. Therefore for $r \leq S_f$, those terms in $C_i(r)$ with factors N_r/N, L_r/L, or S_r/S are identically zero, and the coincidence functions may be well approximated by the first two terms of Equations in Table 2, except for the slab model, which gives 1.0.

Let us "normalize" $g(\ell)$ in the following form:

$$g(\ell) = \frac{A}{\langle \ell \rangle} f\left(\frac{\ell}{\langle \ell \rangle}\right) \quad . \tag{4.12}$$

where A is N, L, or S for spherical, cylindrical, or slab model, respectively. From the conditions that

$$\int_0^\infty g(\ell)\, d\ell = A \quad \text{and}$$

$$\frac{1}{A}\int_0^\infty \ell\, g(\ell)\, d\ell = \langle \ell \rangle \tag{4.13}$$

we have

$$\int_0^\infty f(x)\, dx = 1 \quad \text{and}$$

$$\int_0^\infty x\, f(x)\, dx = 1 \tag{4.14}$$

A more elaborate approximation than Equation (4.11) is to use the fact that $f(0) = 0$ and to approximate $f(x)$ with a Taylor series for small x, i.e.,

$$f(x) = \sum_{K=1}^{\infty} \frac{a_K}{K!}\, x^K \tag{4.15}$$

where $a_K = f^K(0)$. Equation (4.11) suggests that $a_K = 0$ for the first few K's. For the purpose of estimating the order of magnitude of the functions $C_i(r)$, a most conservative assumption is $0 < a_1 < 1$. Then, for small ℓ, $g(\ell) = \frac{a_1 A}{\langle \ell \rangle^2}\, \ell +$ higher order terms, and

$$\langle \ell^K \rangle_r = \frac{A}{A_r}\, \frac{a_1}{\langle \ell \rangle^2} \int_0^r \ell^{K+1}\, d\ell$$

$$\frac{A_r}{A} \langle \ell^K \rangle_r = \frac{a_1}{K+2}\, \frac{r^{K+2}}{\langle \ell \rangle^2}$$

Assuming $\langle \ell^K \rangle \langle \ell^m \rangle = O(\langle \ell \rangle^{K+m}) = O(\langle W \rangle^{K+m})$

we have

$$C_1(r_1) = O\left(\frac{r_1}{\langle W \rangle}\right)^4 \qquad C_2(r) = O\left(\frac{r}{\langle W \rangle}\right)^5$$

$$C_3(r_2) = O\left(\frac{r_2}{\langle W \rangle}\right)^3 \qquad C_4(r_1) = O\left(\frac{r_1}{\langle W \rangle}\right)^3$$

$$C_5(r) = O\left(\frac{r}{\langle W \rangle}\right)^3 \qquad C_6(r_2) = O\left(\frac{r_2}{\langle W \rangle}\right)^3 \quad (4.16)$$

$$C_7(r_1) = O\left(\frac{r_1}{\langle W \rangle}\right)^2 \qquad C_8(r) = O\left(\frac{r}{\langle W \rangle}\right)^3$$

$$C_9(r_2) = O\left(\frac{r_2}{\langle W \rangle}\right)^2$$

Substituting Equations (4.16) into equations in Table 2, we have the following for $r_1/\langle \ell \rangle < 1$, or $r_1/\langle W \rangle < 1$

Table 3

	$m_2/m = n_2/n$	γ_2/γ
Spherical Model	$\begin{cases} 1 - \frac{4}{9}\frac{\langle \ell^3 \rangle^2}{\langle \ell^2 \rangle^3}\frac{r_1^2}{\langle W \rangle^2} + O\left(\frac{r_1}{\langle W \rangle}\right)^4 \\ 1 - C_5\frac{r_2}{\langle W \rangle} + O\left(\frac{r_2}{\langle W \rangle}\right)^3 \end{cases}$	$1 - \frac{r}{\langle W \rangle} + O\left(\frac{r}{\langle W \rangle}\right)^3$
Cylindrical Model	$\begin{cases} 1 - \frac{3}{8}\frac{\langle \ell^2 \rangle^2}{\langle \ell \rangle^3}\left\langle \frac{1}{\ell} \right\rangle \frac{r_1^2}{\langle W \rangle^2} + O\left(\frac{r_1}{\langle W \rangle}\right)^3 \\ 1 - C_c\frac{r_2}{\langle W \rangle} + O\left(\frac{r_2}{\langle W \rangle}\right)^3 \end{cases}$	$1 - \frac{r}{\langle W \rangle} + O\left(\frac{r}{\langle W \rangle}\right)^3$
Slab Model	$\begin{cases} 1 - O\left(\frac{r_1}{\langle W \rangle}\right)^2 \\ 1 - O\left(\frac{r_2}{\langle W \rangle}\right)^2 \end{cases}$	$1 - \frac{r}{\langle W \rangle} + O\left(\frac{r}{\langle W \rangle}\right)^3$

where

$$C_S = \frac{8}{3\pi} \cdot \frac{\langle l \rangle \langle l^3 \rangle}{\langle l^2 \rangle^2} \quad \text{and} \quad C_c = \frac{2}{\pi} \frac{\langle l^2 \rangle}{\langle l \rangle^2}$$

The results of the measurements of the coincidence functions are shown in Figures 47, 48, 49 and 50. The dependence of γ_2/γ on $r_1/\langle w \rangle$ and $r_2/\langle w \rangle$ for small values of $r/\langle w \rangle$ agree well with the straight line $\gamma_2/\gamma = 1 - r/\langle w \rangle$, which was estimated for all three types of geometry. Although this result does not differentiate among the three geometric categories, it is extremely encouraging for our approach because there are no adjustable constants.

The data on $\frac{n_2}{n}(r_1)$ show a quadratic departure from 1.0, which agrees qualitatively with all three types of geometry. Since the value $1 - \frac{n_2}{n}(r_1)$ is so small for small r_1, and the coefficients of the quadratic terms in the analytical results are unknown, no distinction among the types of geometry can be made here either.

In Figure 50, the data for $\frac{n_2}{n}(r_2)$ follow the line $\frac{n_2}{n} = 1 - C\frac{r_2}{\langle w \rangle}$ for small values of r_2. This eliminates the possibility of the fine-structure regions being slabs, since the slab model predicts a quadratic departure from 1.0. Empirically, $C \approx 0.7$.

In order to differentiate between the spherical and cylindrical models, the constants C_S and C_c in the equations of Table 3 have to be estimated. First we can show that the quantities $\frac{\langle l^3 \rangle \langle l \rangle}{\langle l^2 \rangle^2}$ and $\langle l^2 \rangle / \langle l \rangle^2$ are each greater than or equal to 1.0:

$$\therefore \langle \ell^K \rangle = \frac{1}{A} \int_0^\infty \ell^K g(\ell)\, d\ell$$

$$\therefore A^2 \left(\langle \ell^3 \rangle \langle \ell \rangle - \langle \ell^2 \rangle^2 \right)$$

$$= \int_0^\infty \ell^3 g(\ell) d\ell \int_0^\infty \ell' g(\ell') d\ell' - \int_0^\infty \ell^2 g(\ell) d\ell \int_0^\infty \ell'^2 g(\ell')\, d\ell'$$

$$= \int_0^\infty \int_0^\infty (\ell^3 \ell' - \ell^2 \ell'^2)\, g(\ell)\, g(\ell')\, d\ell\, d\ell'$$

$$= \frac{1}{2} \int_0^\infty \int_0^\infty (\ell^3 \ell' + \ell \ell'^3 - 2\ell^2 \ell'^2)\, g(\ell) g(\ell')\, d\ell\, d\ell'$$

$$= \frac{1}{2} \int_0^\infty \int_0^\infty \ell \ell' (\ell - \ell')^2\, g(\ell)\, g(\ell')\, d\ell\, d\ell'$$

≥ 0 because $g \geq 0$ and $\ell, \ell' \geq 0$

$$\therefore \langle \ell^3 \rangle \langle \ell \rangle - \langle \ell^2 \rangle^2 \geq 0$$

and
$$\frac{\langle \ell^3 \rangle \langle \ell \rangle}{\langle \ell^2 \rangle^2} \geq 1 \qquad (4.17)$$

Schwarz's inequality states that

$$\frac{\langle \ell^2 \rangle}{\langle \ell \rangle^2} \geq 1 \qquad (4.18)$$

Therefore $$C_s \geq \frac{8}{3\pi} = 0.85$$

(4.19)*

and $$C_c \geq \frac{2}{\pi} = 0.64$$

The data in Figure 50 are shown in Figure 51 with amplified scale. The experimental result of $C \simeq 0.70$ disagrees with the behavior of the spherical model, which requires that the coincidence function fall below the straight line

$$\frac{n_2}{n} = 1 - 0.85 \frac{r_2}{\langle W \rangle} \tag{4.20}$$

On the other hand, the cylindrical model requires that the coincidence function fall below the straight line

$$\frac{n_2}{n} = 1 - 0.64 \frac{r_2}{\langle W \rangle} \tag{4.21}$$

---

*If we assume a functional form for $g(\ell)$ such that $f(x)$ in Equation (4.12) has the form

$$f(x) = a\, x^K \exp(-bx)$$

then

$$C_s = 0.85 \frac{K+3}{K+2}$$

$$C_c = 0.64 \frac{K+2}{K+1}$$

To fit the experimental result of $C = 0.70$, a value of $K = 9$ is required.

If we assume $$f(x) = a\, x^K \exp(-bx^2)$$

then $C_c = 0.70$ and $C_s = 0.94$ for $K = 4$.

We see that the measured coincidence rates are consistent with the random cylinder model. Therefore the statistical geometry of the fine-structure regions is more likely to be "rods" distributed randomly in the flow field than slabs or blobs.

Needless to say, the possibility of a mixture of rods and blobs, and the possibility of "elongated blobs," remain. For elaborate measurements will be required to decide among these alternatives.

V. DISCUSSION AND CONCLUSIONS

This investigation shows that in a fully developed turbulent flow, the fine-scale components of velocity localize in relatively small regions which are distributed randomly throughout the flow field, while the large-scale components cover the entire flow field. Two-probe coincidence measurements for the occurrence of fine-structure suggest that the fine-structure regions are likely to have random "rod-like" geometry, as contrasted to two other categories: "blob-like" and "slab-like." If we divide the flow field into two kinds of regions, one with fine-structure and the other without, then Figure 54 may represent a qualitative picture of the flow field. The "diameters" of the rods are large compared with the size of eddies of which they are composed, and is smaller for smaller eddies. The mean "rod separation" is fairly large compared with the rod thickness. The radius of curvature of the rod axis is presumably large compared with rod diameter, otherwise the rods would "look like" blobs.

Since we divide the flow field into two kinds of regions only, the geometry of the fine-structure regions must be related to that of the "no-fine-structure" regions. In fact, we could have done intermittency and coincidence measurements using absence of fine-structure as the significant event. Suppose that, instead of $I(t)$, we had obtained from the intermittency circuit a signal $I'(t)$ such that

$$I'(t) = \begin{cases} 1.0 & \text{when the hot-wire is in the no-fine-structure regions,} \\ 0 & \text{otherwise} \end{cases}$$

We could have defined and measured the statistical quantities γ', n' and the coincidence functions γ_2', n_2' for $I'(t)$ the same way as γ, n, γ_2, n_2 for $I(t)$. It can be shown that γ', n', γ_2', and n_2' are determined uniquely by γ, n, γ_2, and n_2.

(1) By definition, we have

$$I'(t) = 1 - I(t)$$

$$\gamma = \overline{I(t)}$$

$$\gamma' = \overline{I'(t)} \qquad n' = n$$

$$\therefore \quad \gamma' = \overline{1 - I(t)} = 1 - \gamma \tag{5.1}$$

Let $I_1'(t)$ and $I_2'(t)$ be the signals from two hot-wires separated by a distance r. Then

$$\gamma_2' = \overline{I_1'(t)\, I_2'(t)}$$

$$= \overline{[1 - I_1(t)][1 - I_2(t)]}$$

$$= 1 - 2\gamma + \gamma_2$$

$$\therefore \quad \frac{\gamma_2'}{\gamma'} = 1 - \frac{\gamma}{1-\gamma}\left(1 - \frac{\gamma_2}{\gamma}\right) \tag{5.2}$$

For the experimental results on $\gamma_2/\gamma(r)$, it is convenient to define a function $h\left(\frac{r}{\langle w \rangle}\right)$ such that

$$\frac{\gamma_2}{\gamma} \equiv 1 - h\left(\frac{r}{\langle w \rangle}\right) \tag{5.3}$$

and if we define the mean "pulse length" as

$$\langle w' \rangle \equiv \frac{\gamma' \sqcup}{n'} = \frac{(1-\gamma)\sqcup}{n} = \frac{1-\gamma}{\gamma}\langle w \rangle$$

then, by substituting (5.3) into (5.2) and changing the variable, we have

$$\frac{\gamma_2'}{\gamma'}\left(\frac{r}{\langle w'\rangle}\right) = 1 - \frac{\gamma}{1-\gamma}\, h\left(\frac{\langle w'\rangle}{\langle w\rangle}\,\frac{r}{\langle w'\rangle}\right)$$

$$= 1 - \frac{\gamma}{1-\gamma}\, h\left(\frac{1-\gamma}{\gamma}\,\frac{r}{\langle w'\rangle}\right) \qquad (5.4)$$

The experimental results in Figures 47 and 49 suggest that, for $r \ll \langle w\rangle$,

$$h\left(\frac{r}{\langle w\rangle}\right) \approx K\,\frac{r}{\langle w\rangle}$$

with $K \approx 1.0$.

Therefore, from Equation (5.4), we have

$$\frac{\gamma_2'}{\gamma'} \approx 1 - \frac{r}{\langle w'\rangle} \qquad \text{for } r \ll \langle w'\rangle \qquad (5.5)$$

(2) n_2' is the average number of pulses per unit time of the signal

$$I_1'(t)\, I_2'(t) = 1 - I_1(t) - I_2(t) + I_1(t)\, I_2(t)$$

We may determine n_2' by counting the rate of occurrence (per unit time) of time intervals for which

$$I_1'(t)\, I_2'(t) = 0$$

Whenever $I_1(t)$ is 1.0, $I_1'(t)\, I_2'(t)$ is 0, regardless of the value of $I_2(t)$; this contributes number n to n_2' , since n is the number of time intervals in which $I_1(t)$ is 1.0. When $I_2(t)$ is 1.0, it will add new time intervals to the event $I_1'(t)\, I_2'(t) = 0$ only if $I_1(t) = 0$ simultaneously. This contributes a number $n - n_2$

to n_2' .

$$\therefore \quad n_2' = 2n - n_2$$

$$\frac{n_2'}{n'} = 2 - \frac{n_2}{n} \tag{5.6}$$

For the experimental results on $\frac{n_2}{n}(r)$ it is convenient to define a function $h'\left(\frac{r}{\langle w \rangle}\right)$ such that

$$\frac{n_2}{n}\left(\frac{r}{\langle w \rangle}\right) \equiv 1 - h'\left(\frac{r}{\langle w \rangle}\right) \tag{5.7}$$

Then, by substituting (5.7) into (5.6), and changing the variable, we have

$$\frac{n_2'}{n'}\left(\frac{r}{\langle w' \rangle}\right) = 1 + h'\left[\frac{1-\gamma}{\gamma}\frac{r}{\langle w' \rangle}\right] \tag{5.8}$$

The experimental results in Figures 48 and 50 suggest that, for

$r \ll \langle w \rangle$ $\quad h'\left(\frac{r_1}{\langle w \rangle}\right) = c'\frac{r_1^2}{\langle w \rangle^2}, \qquad c' > 0$

$$h'\left(\frac{r_2}{\langle w \rangle}\right) = c\frac{r_2}{\langle w \rangle}, \qquad c \simeq 0.70$$

Therefore, from Equation (5.8), we have

$$\frac{n_2'}{n'}\left(\frac{r}{\langle w' \rangle}\right) = \begin{cases} 1 + c'\left(\frac{1-\gamma}{\gamma}\right)^2 \frac{r_1^2}{\langle w' \rangle^2} \\ 1 + c\left(\frac{1-\gamma}{\gamma}\right)\frac{r_1}{\langle w' \rangle} \end{cases} \tag{5.9}$$

Equations (5.5) and (5.9) could have described the experimental results for small r if two-probe coincidence measurements for the occurrence of no-fine-structure regions had been performed.

Equation (5.5) agrees with the analytical results of Chapter III for all three geometric categories [Equations (3.15), (3.20), (3.23)] , so no distinction can be drawn from this. Equation (5.9), on the other hand, is different from the analytical results for all three geometric categories.

At least two possible conclusions may be drawn: (1) the no-fine-structure regions cannot be described by any of the three geometric categories assumed in Chapter III; we can, however, infer that the fine-structure regions cannot be slabs, since that would imply that the no-fine-structure regions are blobs, whose prediction disagrees with Equation (5.9). (2) the volume fraction of the no-fine-structure regions is too large (0.7 in this experiment) for the analysis of Chapter III to be applicable.

The comparison of experimental and analytical results in Section 4.5 shows clearly that the fine-structure regions are not slabs. But the distinction between cylindrical and spherical models is not so clear cut. In Figure 51, the first quadrant of the $\frac{n_2}{n} - \frac{r_2}{\langle w \rangle}$ plane may be divided into three regions by the two straight lines

(a) $$\frac{n_2}{n} = 1 - 0.64\, r_2/\langle w \rangle$$

(b) $$\frac{n_2}{n} = 1 - 0.85\, r_2/\langle w \rangle$$

Line (a) is the upper limit for the cylindrical model. This upper limit occurs if all the cylinders have the same diameter, i.e., $g(\ell)$ is a Dirac function. Line (b) is the upper limit for the spherical model. This upper limit occurs if all the spheres have

the same diameter. If the n_2/n data for small r_2 fell above line (a), neither cylindrical nor spherical model would be correct. If the data fell below line (b), both the cylindrical and spherical models would be possible. The data actually fall in the region between lines (a) and (b), in which among the three geometric models only the cylindrical one is possible. But the cylindrical geometry alone does not predict the exact location of the data. The probability function $g(\ell)$ of the cylinder diameters determines the coefficient C_c in the equation of Table 2.

If the probability function $g(\ell)$ were known, then we could check the form of the coincidence function in detail. But we still have neither an experimental procedure for measuring it nor a theoretical basis for estimating it.

With $g(\ell)$ unknown, the experimental results also allow the possibility that the fine-structure regions are a mixture of rods and blobs or have a geometry between rod and blob, i.e., an elongated blob or finite length cylinder.

If the fine-structure regions are a mixture of spheres and cylinders, we can write the intermittency factor and the pulse rate of the signal $I(t)$ as

$$\gamma = \gamma_s + \gamma_c \tag{5.10}$$

and

$$n = n_s + n_c \tag{5.11}$$

where γ_s and γ_c are the fractions of time the detector is in a sphere and in a cylinder, respectively, n_s and n_c are the average

numbers per unit time, of spheres and cylinders hitting the hot-wire.

We may also define the average intersection chord lengths with spheres, with cylinders, and with the mixture as

$$\langle W_s \rangle = \frac{\sqcup \gamma_s}{n_s}$$

$$\langle W_c \rangle = \frac{\sqcup \gamma_c}{n_c}$$

$$\langle W \rangle = \frac{\sqcup \gamma}{n} = \frac{\sqcup (\gamma_s + \gamma_c)}{n_s + n_c}$$

If we place two detectors in the flow field and neglect the occasions on which they are in two different fine-structure domains, we can write

$$\frac{\gamma_2}{\gamma} = \frac{\gamma_{2s} + \gamma_{2c}}{\gamma_s + \gamma_c} \tag{5.12}$$

At $r \ll \langle W \rangle$, Equations (3.15) and (3.20) reduce to

$$\frac{\gamma_{2s}}{\gamma_s} = 1 - \frac{r}{\langle W_s \rangle} \tag{5.13}$$

$$\frac{\gamma_{2c}}{\gamma_c} = 1 - \frac{r}{\langle W_c \rangle} \tag{5.14}$$

Substituting (5.13) and (5.14) into (5.12), we have

$$\frac{\gamma_2}{\gamma} = 1 - \frac{r}{\langle W \rangle} \tag{5.15}$$

which agrees with experimental results regardless of the ratios γ_s/γ_c and n_s/n_c, the sphere-to-cylinder volume ratio and number ratio, respectively.

For the average number of fine-structure regions, per unit time, hitting both detectors simultaneously, we have

$$\frac{n_2}{n} = \frac{n_{2s} + n_{2c}}{n_s + n_c} \tag{5.16}$$

At $r_2 \ll \langle W \rangle$, Equations (3.17) and (3.21) reduce to

$$\frac{n_{2s}}{n_s} = 1 - C_s \frac{r_2}{\langle W_s \rangle} \; ; \quad C_s = \frac{8}{3\pi} \frac{\langle l_s \rangle \langle l_s^3 \rangle}{\langle l_s^2 \rangle^2} \tag{5.17}$$

$$\frac{n_{2c}}{n_c} = 1 - C_c \frac{r_2}{\langle W \rangle} \; ; \quad C_c = \frac{2}{\pi} \frac{\langle l_c^2 \rangle}{\langle l_c \rangle^2} \tag{5.18}$$

Substituting (5.17) and (5.18) into (5.16), we have

$$\frac{n_2}{n} = 1 - C_M \frac{r_2}{\langle W \rangle} \tag{5.19}$$

where

$$C_M = \frac{\gamma \left(\frac{C_s}{\gamma_s} n_s^2 + \frac{C_c}{\gamma_c} n_c^2 \right)}{n^2} \tag{5.20}$$

Write $\alpha = \gamma_s / \gamma_c$, $\beta = n_s / n_c$, $\rho = \frac{\alpha}{\beta}$

then

$$C_M = \frac{C_c + \beta \left(C_c \rho + \frac{C_s}{\rho} \right) + C_s \beta^2}{(1+\beta)^2} \tag{5.21}$$

From Equations (3.3) and (3.7)

$$\alpha = \frac{2 N \langle l_s^3 \rangle}{3 L \langle l_c^2 \rangle}$$

and from Equations (3.2) and (3.6)

$$\beta = \frac{N \langle l_s^2 \rangle}{L \langle l_c \rangle} \tag{5.22}$$

$$\therefore \quad \rho = \frac{2}{3} \frac{\langle l_s^3 \rangle \langle l_c \rangle}{\langle l_s^2 \rangle \langle l_c^2 \rangle}$$

The coefficients C_s and C_c in Equations (5.17) and (5.18) will attain their minimum values

$$(C_s)_m = 0.85$$

$$(C_c)_m = 0.64$$

if all the spheres are a single size and all the cylinders are a (possibly different) single size, i.e.,

$$l_s = \text{constant}$$

$$l_c = \text{constant}$$

For this case, Equation (5.21) gives

$$C_M = 0.64 \frac{1 + (\rho + \frac{1.33}{\rho})\beta + 1.33\beta^2}{(1+\beta)^2}$$

and, for given β, C_M has a minimum value $(C_M)_m$

$$(C_M)_m = 0.64 \frac{1 + 2.3\beta + 1.33\beta^2}{(1+\beta)^2} \tag{5.23}$$

when $\rho = 1.15$, i.e. $\frac{2}{3} \frac{l_s}{l_c} = 1.15$ (5.24)

Therefore, restricting to $r_2 \ll \langle W \rangle$, the straight line

$$\frac{n_2}{n} = 1 - (C_M)_m \frac{r_2}{\langle W \rangle} \tag{5.25}$$

is the upper limit for the "mixture" model. $(C_M)_m$ is a monotonically increasing function of β, the number ratio.

Since the experimental data lie on a straight line

$$\frac{n_2}{n} = 1 - 0.7 \frac{r_2}{\langle W \rangle} \quad \text{for} \quad r_2 \ll \langle W \rangle$$

the maximum permissible β will be the one such that $(C_M)_m = 0.7$, then

$$\beta_{max} = 0.41^* \text{ and}$$

$$\alpha_{max} = \rho \beta_{max} = 0.47$$

That is, the experimental data allow a maximum sphere volume of $\frac{0.47}{1+0.47} = 32\%$ of the total volume of the fine-structure regions. This maximum volume ratio occurs when, from Equation (5.24)

$$\ell_s = 1.73 \ \ell_c = \text{constant.} \tag{5.26}$$

If we make the more realistic assumptions that the diameters are distributedover some range, C_M will be greater than $(C_M)_m$ for the same value of β. Therefore the volume fraction of spheres has to be smaller than 32% in order to agree with the experimental results.

---

*The other solution for β is -0.91, which is physically impossible.

For example, the case that

$$\ell_s = \ell_c = \text{constant}$$

gives a volume ratio of 11%.

If we assume that the fine-structure regions are elongated blobs or finite length cylinders, we can expect that the upper limit of the coincidence function $\frac{n_2}{n}(r_2)$ (which happens when all the cylinders have the same diameter) will be a straight line between lines (a) and (b) in Figure 51. No analysis has been carried out for this model, but this line of upper limit will tend toward line (b) as the length-to-diameter ratio of the cylinder decreases, and will coincide with line (b) when the length-to-diameter ratio is of the order of unity. Since the experimental data lie closer to line (a) than line (b), it is expected that the length-to-diameter ratio would be at least appreciably greater than one for the special case that all the cylinders are of the same diameter. If the cylinder diameters distribute over some range, the length-to-diameter ratio will be even higher.

This experimental investigation of the statistical geometry of fine-structure regions has provided only a starting point for future work. A more detailed investigation by coincidence measurements with three or even more probes would be interesting. It would also be interesting to detect the geometry in a turbulent shear region, where the rod-like geometry would have a preferred direction.

The fine-scale components of temperature fluctuations have been observed to be intermittent in the wind over ocean.[6] Studies of the

statistical geometry of the fine-structure regions of such scalor fields are certainly worthwhile. Efforts might be made to correlate the fine-structure intermittency between scalor field and velocity field.

Finally, a theoretical attempt might be tried to relate the geometry by seeking the dominant signs* of the short-time-average principal strain rates following a fluid element in which the fine-structure exists. Betchov[37] has discussed the dominant signs of the average principal rates in an isotropic turbulent flow. But his results cannot be applied here since he talked about (ensemble) average fixed in space and time while the average we need is the "short" time average following a particular fine-structure region.

---

*see discussion at the beginning of Chapter III.

APPENDIX

A1. On the Application of Taylor's Hypothesis

In this experiment, Taylor's hypothesis[37] (or "approximation") has been applied on two occasions: (a) interpretation of hot-wire signal high frequency spectrum as turbulence high wave-number spectrum, i.e., fine-structure signal, (b) interpretation of a time-delayed signal as though it were the non-delayed signal from a hot-wire at a location directly downstream of the point of interest.

Taylor's hypothesis is based on the assumption that the spatial pattern of turbulent motion is convected past a fixed point by the mean flow without any essential change. Considering application to the fine-scale structure, we must consider not only the "self-convection" effect, but also the fact that the small eddies are carried about "within" the energy-containing (large) eddies, and thus are convected by the fluctuating velocity field of large-scale structure as well as by the mean velocity field. If u' and $\mathcal{L}$ are the velocity and length scales of the energy-containing eddies, the unsteadiness of convection velocity will be of the order of u' and the non-uniformity of the convection velocity across a small eddy of size $\frac{1}{k}$ will be $\frac{u'}{\mathcal{L}k}$.*

---

*In a mean-shear region there is, of course, a non-uniformity of convection velocity due to the mean velocity gradient, viz., $\frac{1}{k}\frac{\partial U}{\partial y}$, but the data reported here are recorded at positions where $\frac{\partial U}{\partial y} = 0$.

In a grid-generated turbulence, the mean velocity U is uniform and u'/U ($\simeq 0.02$) is small, hence the unsteadiness and non-uniformity of convection velocity are negligible; this justifies the interpretation of frequency spectrum as wave-number spectrum. Good agreements between theory and experiment in grid-generated turbulence have been reported by Taylor[37] and others.

The first extensive and good experimental check of Taylor's hypothesis was made by Farre, Gaviglio, and Dumas[38] in a turbulent boundary layer.

The applicability of (a) at large turbulence levels as on the axis of a round jet or in other shear flows has been discussed by Lin.[39] Fisher and Davies,[40] and Lumley.[41] A correction form for the wave-number spectrum has been suggested by Lumley.

Application (b) of Taylor's hypothesis permits us to interpret a time varying signal from a hot-wire fixed in space as an instantaneous function of spatial coordinate along the path of mean flow. The intermittency of a high frequency signal in the time domain may be interpreted as an indication of localization of the fine-structure in the space domain. The time intervals when the high frequency signal is zero correspond to the hot-wire sweeping through spatial regions in which the fine-scale components of motion do not exist.

In the two-probe coincidence measurements for the occurrence of the fine-structure, the flow disturbance due to one hot-wire prohibits the placement of the second one in its wake. The Taylor's hypothesis, however, allows us to measure the coincidence functions

$\frac{\gamma_2}{\gamma}(r_1)$ and $\frac{\eta_2}{\eta}(r_1)$ with a single wire plus a signal delay line. The delayed signal from the hot-wire is interpreted as the signal from a fictitious hot-wire at a location directly downstream, with separation

$$r_1 = U\tau \tag{A1.1}$$

where U is the mean velocity and τ is the delay time.

If t_s is the time scale of the fine-structure whose presence we seek, then the approximation is good only for $\tau \ll t_s$. In the investigation of the geometry of fine-structure regions, the fine-structure signal is a high-pass signal from a grid-generated turbulence with $R_\lambda \doteq 110$. This high-pass signal has a spectrum peaked at 3.5 kHz (see Figure 46), which corresponds to wave-number $k_1 = 17.3/\text{cm}$. The eddies of this wave-number have a characteristic length $1/k_1$ and a characteristic velocity $(k_1 E_{11})^{1/2}$, where $E_{11}(k_1)$ is the one-dimensional energy spectrum. Therefore, a characteristic inertial time scale (essentially the Onsager time scale), is

$$t_s = \left[k_1^3 E_{11}(k_1)\right]^{-1/2} \tag{A1.2}*$$

which is about 84 ms at $k_1 = 17.3/\text{cm}$. A more conservative estimate of time scale is the Kolmogorov time scale, actually the order

---

*Strictly speaking, the "three-dimensional spectrum" and the wave-number magnitude $|k|$ are more appropriate here, but their values are not available here.

of magnitude of r.m.s. turbulent strain rate and vorticity:

$$t_k = \left(\frac{\langle \varepsilon \rangle}{\nu} \right)^{-1/2} \qquad \text{(A1.3)}$$

which is 7.9 ms for the grid-generated turbulence with $R_\lambda = 110$.

As shown in Figures 47 and 48, both $\gamma_2/\gamma(r_1)$ and $\eta_2/\eta(r_1)$ approach asymptotic values within $r_1/\langle w \rangle \leq 4$, which corresponds to $\tau = 1.6$ ms, only one-fifth of the smaller time scale, t_k. This comparison of t_k with τ assures that the simulation of two hot-wires separated in the mean flow direction by a single hot-wire plus its delayed signal is satisfactory, at least for the range $r_1/\langle w \rangle < 1$, where the data are compared with analytical results.

In fact, the signal which was delayed is the on-off binary signal which distinguishes the fine-structure regions from the rest of the fluid. As long as the shape change of the fine-structure domains is small during the time interval τ, the delayed signal is still a good approximation, even if the fine-scale components inside the domains change appreciably. This probably means that $\tau \ll t_s$ is sufficient.

As an experimental check on the validity of application (b), the space-time correlation of high-pass signals and of on-off binary signals from two hot-wires separated in both r_1 and r_2 directions were measured. The r_2 -separation keeps the downstream wire out of the wake of the upstream one. For two hot-wires fixed in

space, the correlation was measured as a function of τ, the delay time of the signal from the upstream wire. τ_m was plotted as function of r_1 in Figures 52 and 53, where τ_m is the delay time at which the correlation is maximum. The figures show that the data agree quite well with a straight line of slope 0.5 in/ms, which is the mean speed of the flow field. This is in agreement with Taylor's hypothesis.

A2. Some Properties of Log-Normal Probability Distribution

In order to take into account the variation of turbulent energy dissipation rate, Oboukhov[13] and Kolmogorov[14] proposed a modified version of the original universal similarity hypothesis.[8,9] The modification involved the assumption that the logarithm of the energy dissipation rate has a normal distribution. Gurvich and Yaglom[19] presented a theoretical treatment leading to the prediction that any non-negative quantity (e.g., energy dissipation rate) governed by fine-scale components has a log-normal probability distribution.

The prediction of log-normality has been tested experimentally by several investigators,[19,5,42,44] but no unique way of curve fitting has been used up to now. Furthermore, no detailed discussion of the behavior of a log-normal density function has been given. In this section, themethod used in Section 4.3 to try to fit the data with log-normal distribution functions is discussed in detail, and some moments of the log-normal density are compared with direct measurements. The behavior of a log-normal density function is dis-

cussed, in particular, its implication for intermittency.

By log-normal probability distribution, it is meant that the logarithm of a non-negative random variable ε has a normal probability distribution, i.e.,

$$P_{\ln\varepsilon}(y) = \frac{1}{\sqrt{2\pi}\,\beta} \exp\left[-\frac{(y-m)^2}{2\beta^2}\right] \tag{A2.1}$$

where $m = \langle \ln \varepsilon \rangle$ and

$$\beta^2 = \langle (\ln\varepsilon - m)^2 \rangle$$

We can compute arbitrary moments:

Write $y = \ln\varepsilon$; then $\frac{dy}{d\varepsilon} = \frac{1}{\varepsilon}$ and

$$P(\varepsilon) = P_{\ln\varepsilon}(y)\,\frac{dy}{d\varepsilon} \tag{A2.2}$$

$$= \frac{1}{\sqrt{2\pi}\,\beta\,\varepsilon} \exp\left[-\frac{(\ln\varepsilon - m)^2}{2\beta^2}\right]$$

The K^{th} moment of ε

$$\langle \varepsilon^K \rangle = \int_0^\infty \frac{1}{\sqrt{2\pi}\,\beta\,\varepsilon}\, \varepsilon^K \exp\left[-\frac{(\ln\varepsilon - m)^2}{2\beta^2}\right] d\varepsilon \tag{A2.3}$$

$$= \exp\left(mK + \tfrac{1}{2}K^2\beta^2\right)$$

In particular,

$$\langle \varepsilon \rangle = \exp\left(m + \tfrac{1}{2}\beta^2\right)$$

Write $\varepsilon_n = \varepsilon / \langle \varepsilon \rangle$;

then the p.d.f. of this normalized variable is

$$P_n(\varepsilon_n) \equiv \langle \varepsilon \rangle P(\varepsilon_n < \langle \varepsilon \rangle)$$

$$= \frac{1}{\sqrt{2\pi}\,\beta\varepsilon_n} \exp\left[-\frac{(\ln\varepsilon_n + \frac{\beta^2}{2})^2}{2\beta^2}\right] \qquad \text{(A2.4)}$$

The distribution function is

$$\text{Prob}(\varepsilon_n \le a^2) = \int_0^{a^2} \frac{1}{\sqrt{2\pi}\,\beta\varepsilon_n} \exp\left[-\frac{(\ln\varepsilon_n + \frac{\beta^2}{2})^2}{2\beta^2}\right] d\varepsilon_n$$

$$= \int_{-\infty}^{\ln a^2} \frac{1}{\sqrt{2\pi}\,\beta} \exp\left[-\frac{(y_n + \frac{\beta^2}{2})^2}{2\beta^2}\right] dy_n \qquad \text{(A2.5)}$$

where

$$y_n = \ln \varepsilon_n$$

If Equation (A2.5) is plotted on normal probability paper with $\ln a^2$ as amplitude variable, we will have a family of straight lines because we have a normal distribution for $\ln \varepsilon_n$, with parameter β. This normal distribution has a mean of $-\beta^2/2$ and a variance of β. A way to see how closely a set of probability distribution data may be approximated by a log-normal distribution is to try to fit these data with a straight line on a normal probability paper with amplitude plotted in a logarithmic scale. There are two parameters to be adjusted in choosing the best fitted straight lines:

(a) β, which determines the slope of the straight line, if there is a straight line;

$$2\beta = (\ln a^2_{0.84}) - (\ln a^2_{0.16})$$

where $a^2_{0.16}$ and $a^2_{0.84}$ are the values such that

$$\text{Prob.}\left(\varepsilon_n \leq a^2_{0.16}\right) = 0.16$$

$$\text{Prob.}\left(\varepsilon_n \leq a^2_{0.84}\right) = 0.84$$

(b) $\langle \varepsilon \rangle$, which determines the location of the straight line. Different choices of $\langle \varepsilon \rangle$ only add a constant to $\ln \varepsilon_n$ and shift the straight line parallel to itself.

In the actual curve fitting for Chapter IV, β was chosen so that the straight line would fit as many data points as possible. The mean $\langle e^2 \rangle$ of the non-negative random variable was used as $\langle \varepsilon \rangle$ to non-dimensionalize the variable e^2 for convenience; no attempt was made to determine the best $\langle \varepsilon \rangle$, since different choices of $\langle \varepsilon \rangle$ only translate the straight line horizontally. If the data were truly log-normally distributed, then

$$\langle e^2 \rangle = \langle \varepsilon \rangle$$

and $\langle e^2 \rangle$ would be the best choice for $\langle \varepsilon \rangle$; the straight line would be one of the family with $\ln \varepsilon_n$ having a mean of $-\frac{\beta^2}{2}$ and a variance of β .

In Figure 42, the straight line corresponds to a log-normal distribution with $\beta = 2.1$. Then, according to Equation (A2.5),

$$\ln \frac{e_m^2}{\langle \varepsilon \rangle} = \ln a^2_{0.5} = -\beta^2/2 = -2.2$$

where e^2_m is the median of e^2 . But the high-pass signal e^2 is non-dimensionalized by $\langle e^2 \rangle$ in Figure 42, and the straight line has

$$\ln \frac{e_m^2}{\langle e^2 \rangle} = \ln a^2_{0.5} = -0.16$$

$$\therefore \ln \frac{\langle \varepsilon \rangle}{\langle e^2 \rangle} = 0.6 \qquad \text{(A2.6)}$$

or $$\langle \varepsilon \rangle = 1.82 \langle e^2 \rangle$$

Similarly, the probability distribution of the band-pass signal with $\Delta f / f_m = 0.52$ and $f_m = 6.3$ kHz in Figure 41 shows

$$\langle \varepsilon \rangle = 1.68 \langle e^2 \rangle \qquad \text{(A2.7)}$$

We observe that both of these ratios $\langle \varepsilon \rangle / \langle e^2 \rangle$ depart appreciably from 1.0, the value required for a log-normal distribution.

Furthermore, for the probability distribution of a log-normal random variable e^2, then the flatness factor of e would be

$$F \equiv \frac{\langle e^4 \rangle}{\langle e^2 \rangle^2} = \frac{\langle \varepsilon^2 \rangle}{\langle \varepsilon \rangle^2} \qquad \text{(A2.8)}$$

$$= \frac{\exp(2m + 2\beta^2)}{\exp(2m + \beta^2)} = \exp(\beta^2)$$

The band-pass signal data in Figure 41 would give F equal to about 80 ~ 100 ($f_m = 6.3$ kHz). The direct measurement of the flatness factor of this band-pass signal gave a value of 16.*

---

*A similar comparison between the moments computed from log-normal density and direct measurements was published[43] after this Appendix was written.

The fact that the log-normal distribution predicts much higher values for the second and fourth moments of a high frequency signal $e(t)$ cannot be explained by the departure from the log-normal form at small values of e^2. Since the higher order moments weigh more heavily on the large amplitude range, the figures and the numbers suggest that the large values of e^2 are less probable than would be predicted by a log-normal distribution. This deviation at large amplitude was also reported by Stewart, Wilson, and Burling.[42,43]

To see how a log-normally distributed random variable may appear intermittent, some features of the probability density function (A2.4) have to be examined. The peak may be located by setting

$$\frac{dP_n(\varepsilon_n)}{d\varepsilon_n} = 0 \qquad \text{(A2.9)}$$

Substituting Equation (A2.4), we have

$$(\varepsilon_n)_{max.} = \exp\left(-\frac{3}{2}\beta^2\right) \qquad \text{(A2.10)}$$

and

$$P_n\left[(\varepsilon_n)_{max.}\right] = \frac{1}{\sqrt{2\pi}\,\beta}\exp(\beta^2) \qquad \text{(A2.11)}$$

where $(\varepsilon_n)_{max}$ is the location at which $P_n(\varepsilon)$ is maximum. Equations (A2.10) and (A2.11) indicate that the peak of the probability density function will increase and its ε-location will move toward zero as β increases.

A more detailed examination of the variation of $P_n(\varepsilon_n)$ with

β may be achieved by checking the sign of $\frac{\partial P_n}{\partial \beta}$. From Equation (A2.4)

$$\frac{\partial P_n}{\partial \beta} = \frac{1}{\sqrt{2\pi}\,\varepsilon_n} \exp\left[-\frac{(\ln \varepsilon_n + \frac{\beta^2}{2})^2}{2\beta^2}\right]\left[-\frac{1}{\beta^2} - \frac{1}{4} + \frac{(\ln \varepsilon_n)^2}{\beta^4}\right]$$

$$\therefore \quad \frac{\partial P_n}{\partial \beta} > 0 \qquad \text{if}$$

$$(\ln \varepsilon_n)^2 > \frac{\beta^4}{4} + \beta^2 , \quad \text{i.e. if}$$

$$\begin{cases} \varepsilon_n > \exp\left(\sqrt{\beta^4/4 + \beta^2}\right) & \text{or} \\ \varepsilon_n < \exp\left(-\sqrt{\beta^4/4 + \beta^2}\right) \end{cases}$$

and $\frac{\partial P_n}{\partial \beta} < 0$ if

$$\exp\left(-\sqrt{\frac{\beta^4}{4} + \beta^2}\right) < \varepsilon_n < \exp\left(\sqrt{\beta^4/4 + \beta^2}\right)$$

Therefore, as β increases, the probability density at very large and very small values of ε_n will increase and that at intermediate values of ε_n will decrease. Some log-normal probability density curves with various β are shown in Figure 55 and they suggest that the random variable will appear intermittent if β is large enough.

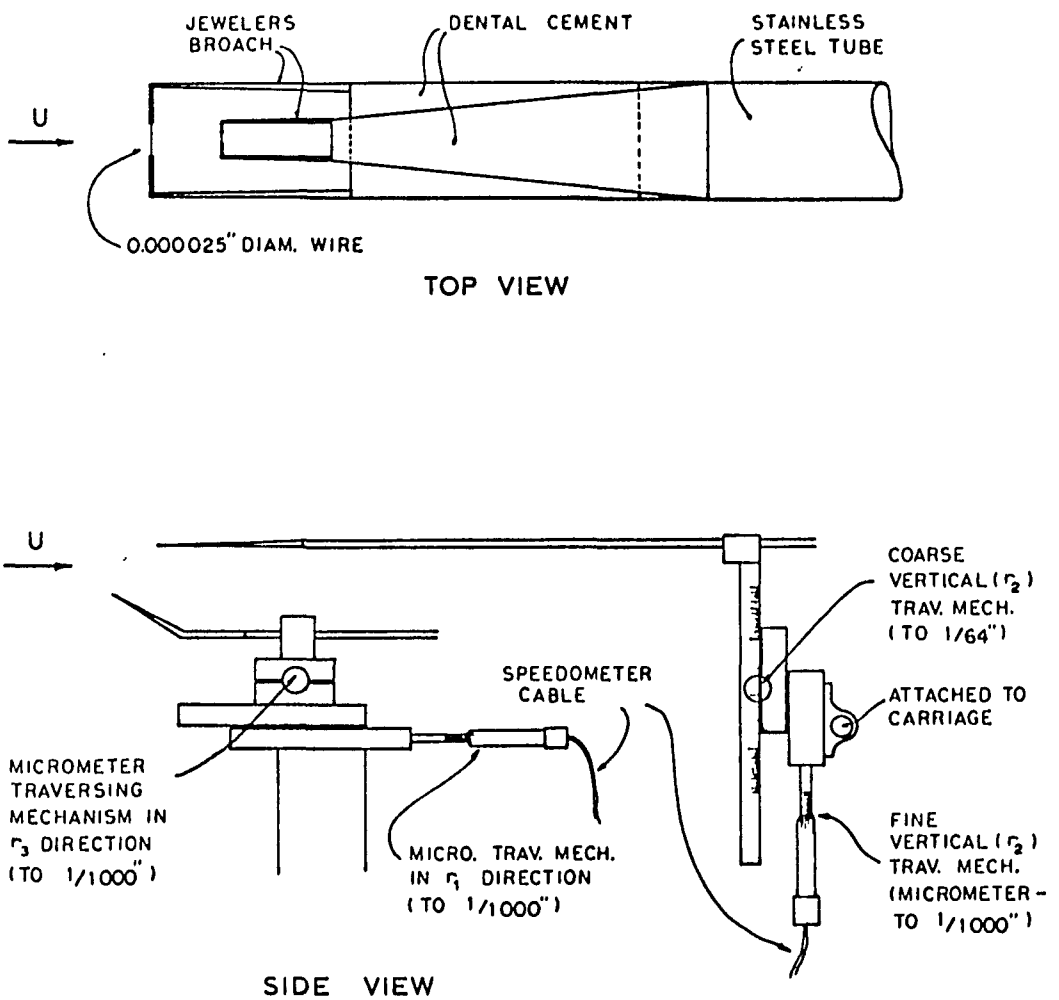

Figure 1. Sketch of Hot-wire Probe Configuration and Traversing Mechanism

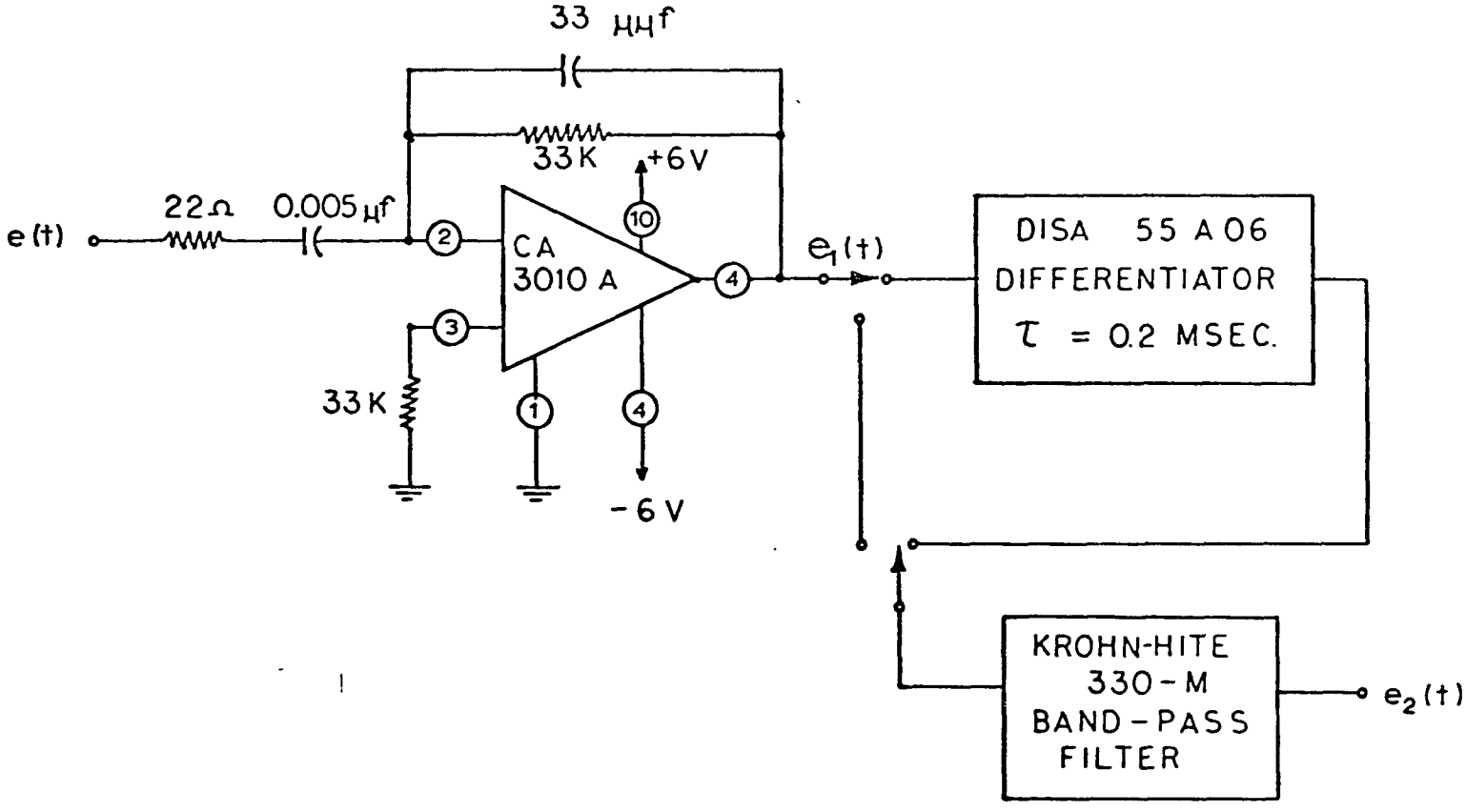

Figure 2. Differentiation Circuit

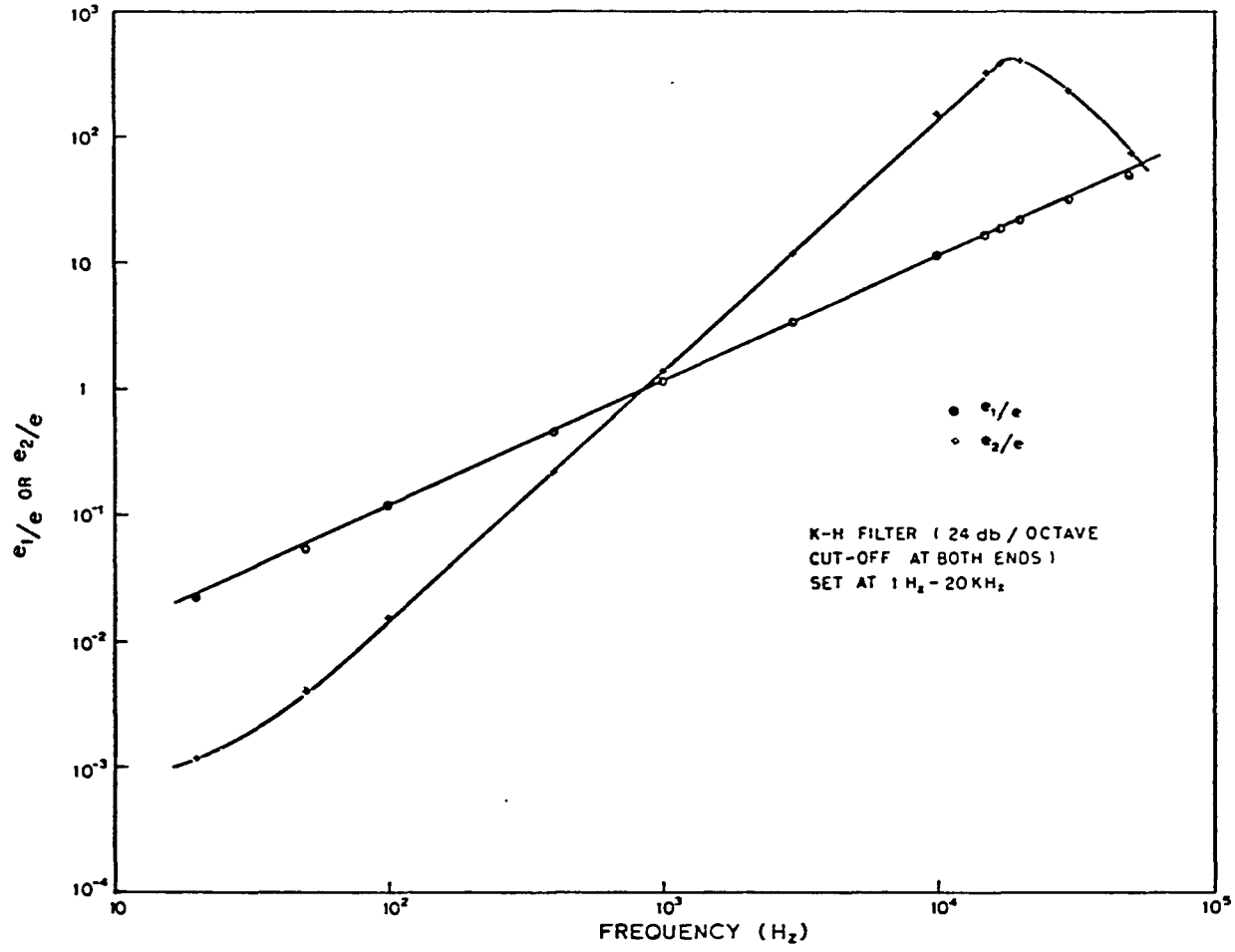

Figure 3. Frequency Response of Differentiation Circuit

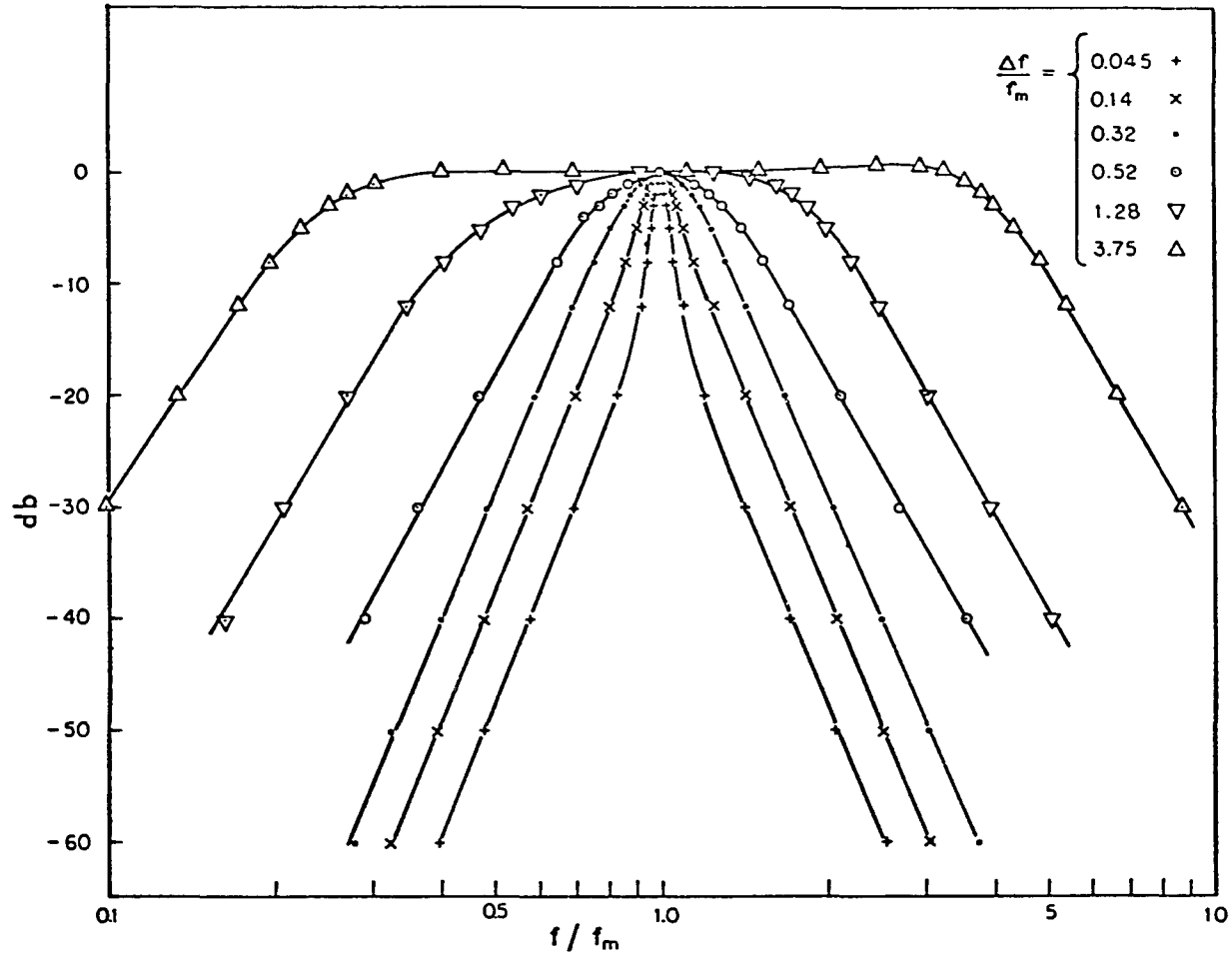

Figure 4. Frequency Response of Band-pass Filter

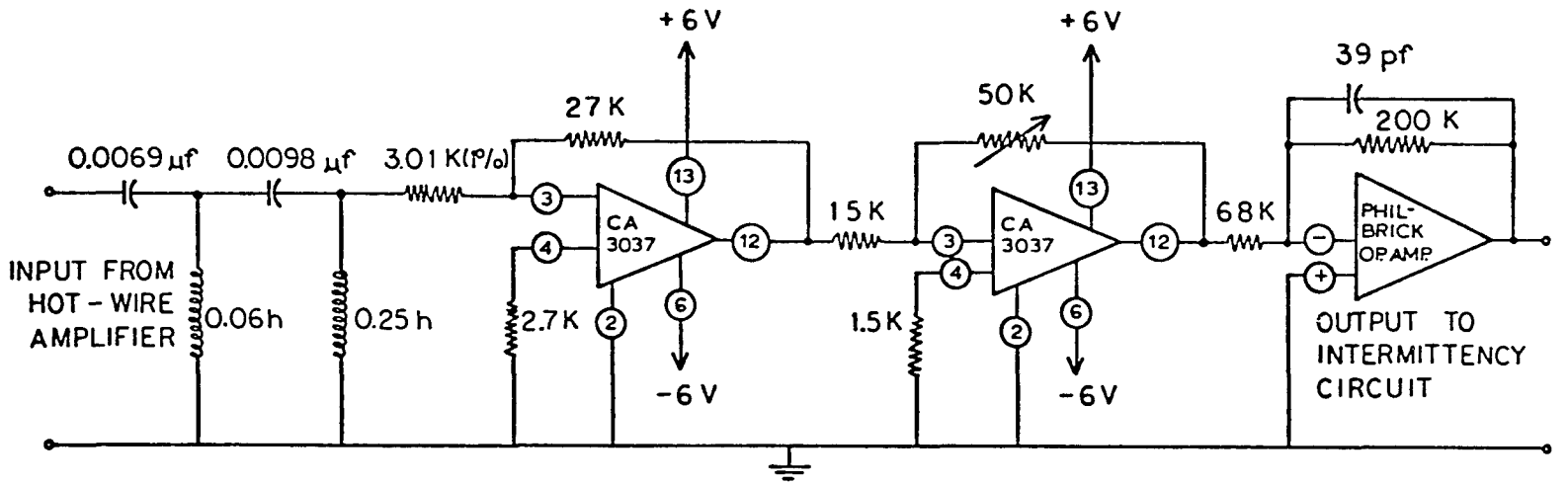

Figure 5. High-pass Butterworth Filter with Amplifiers

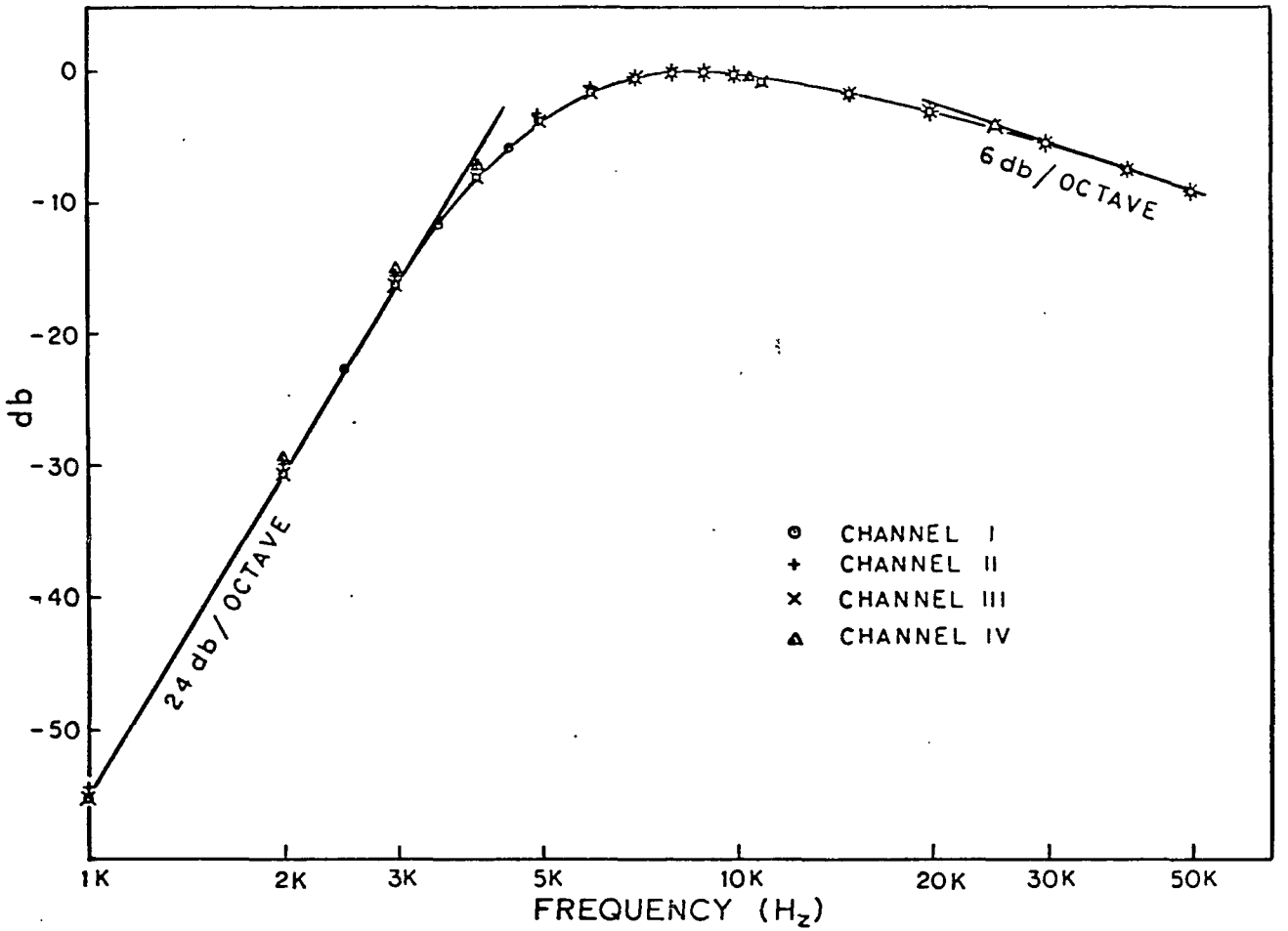

Figure 6. Frequency Response of High-pass Butterworth Filter with Amplifiers

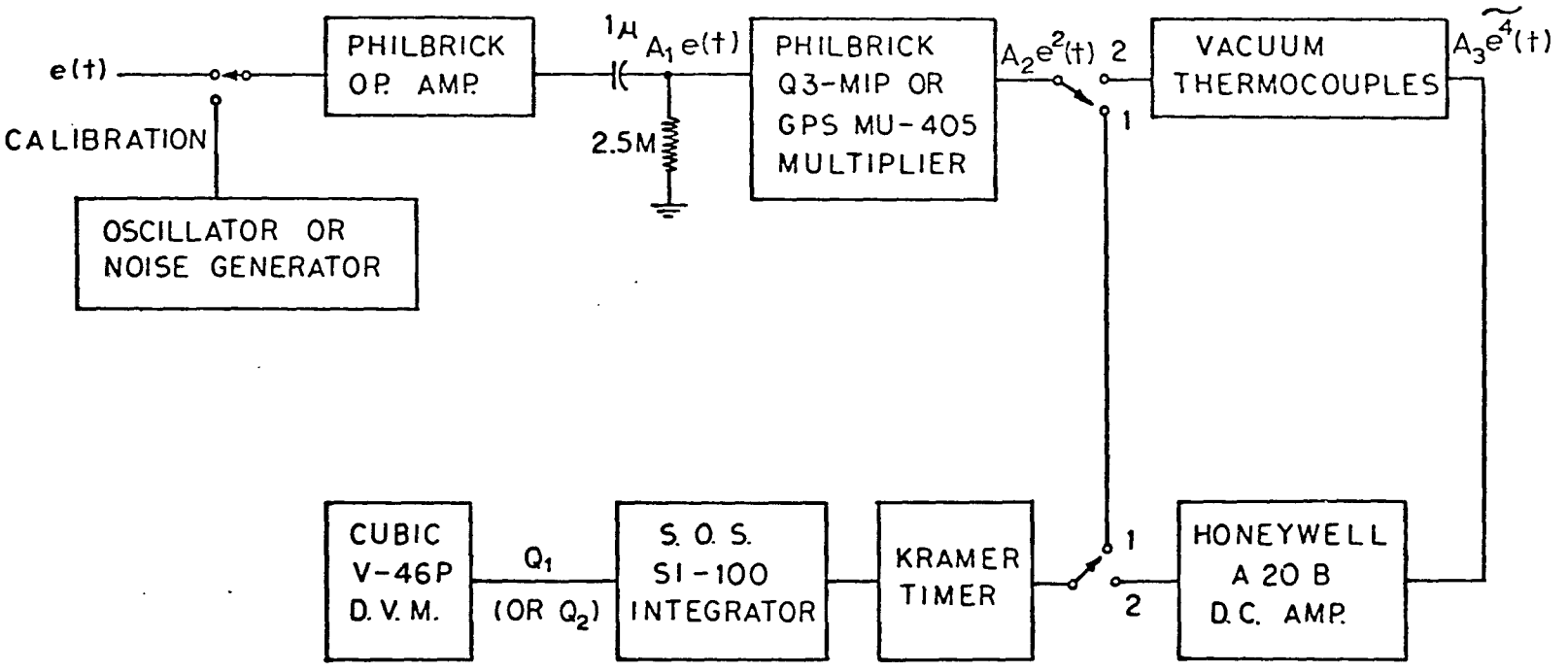

Figure 7. Block Diagram of the Flatness Factor Measuring Devices
(~ means short time average, which is due to the small time constant of vacuum thermocouples)

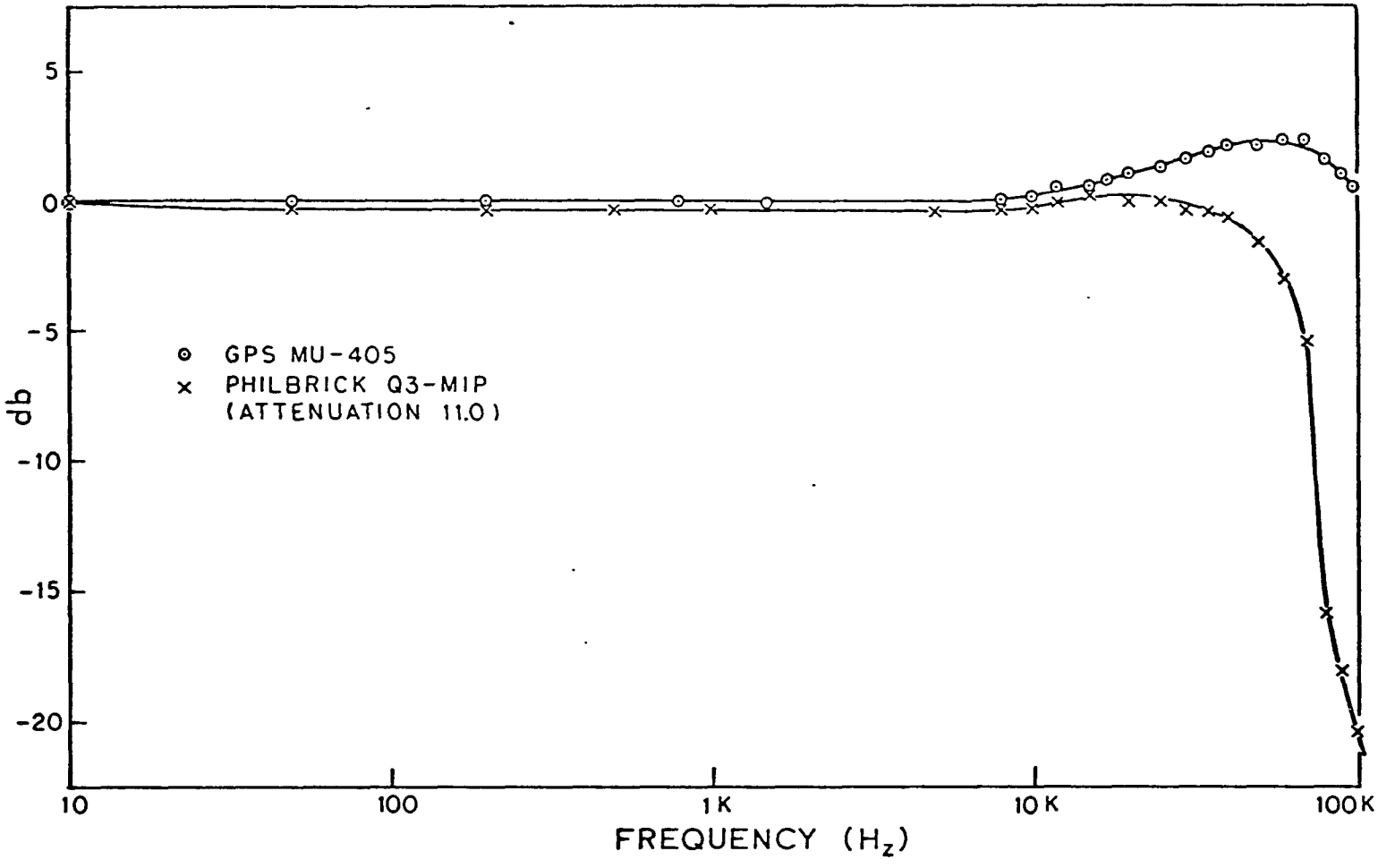

Figure 8. Frequency Response of Multipliers Used as Squaring Circuits

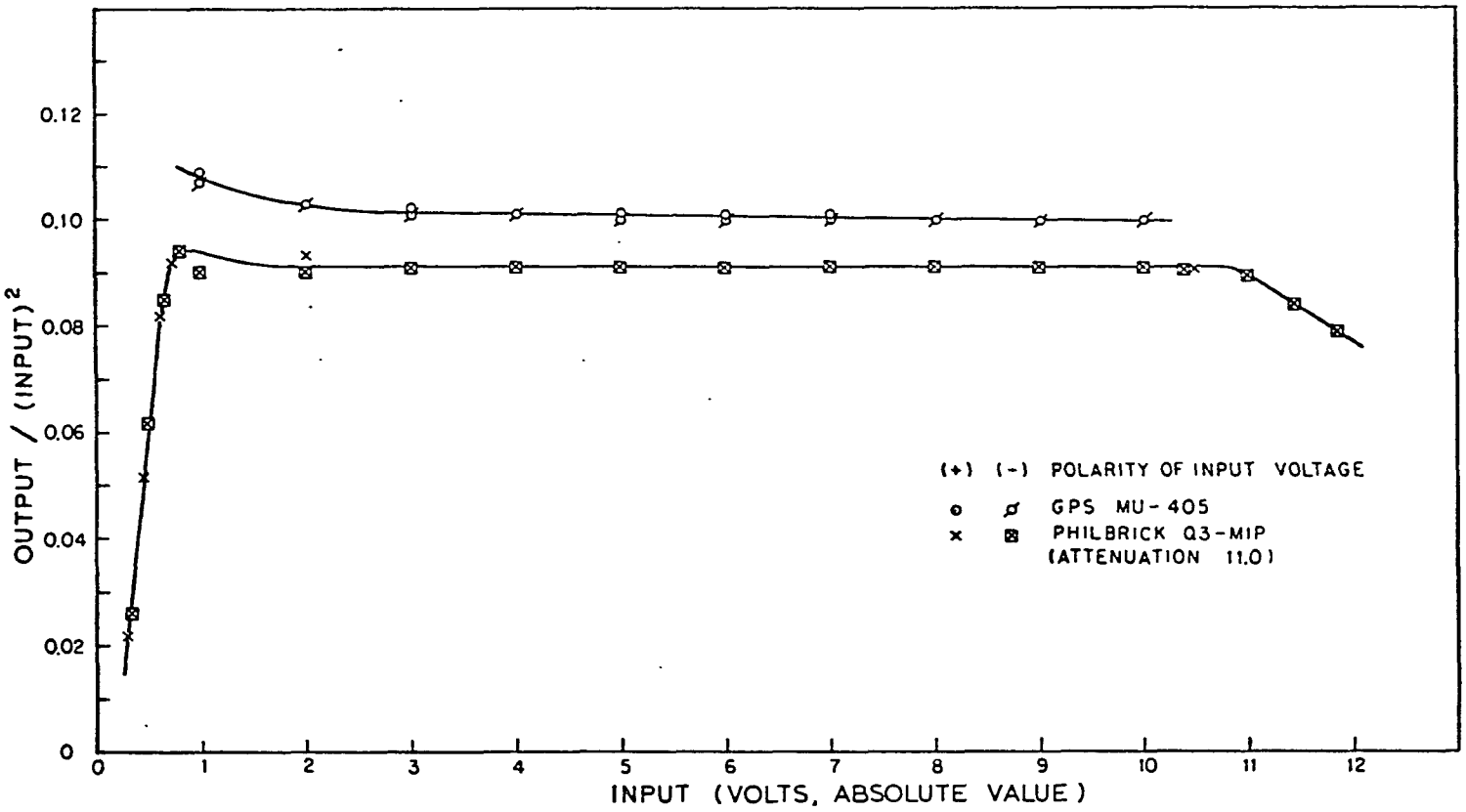

Figure 9. Static Transfer Characteristics of Multipliers Used as Squaring Circuits

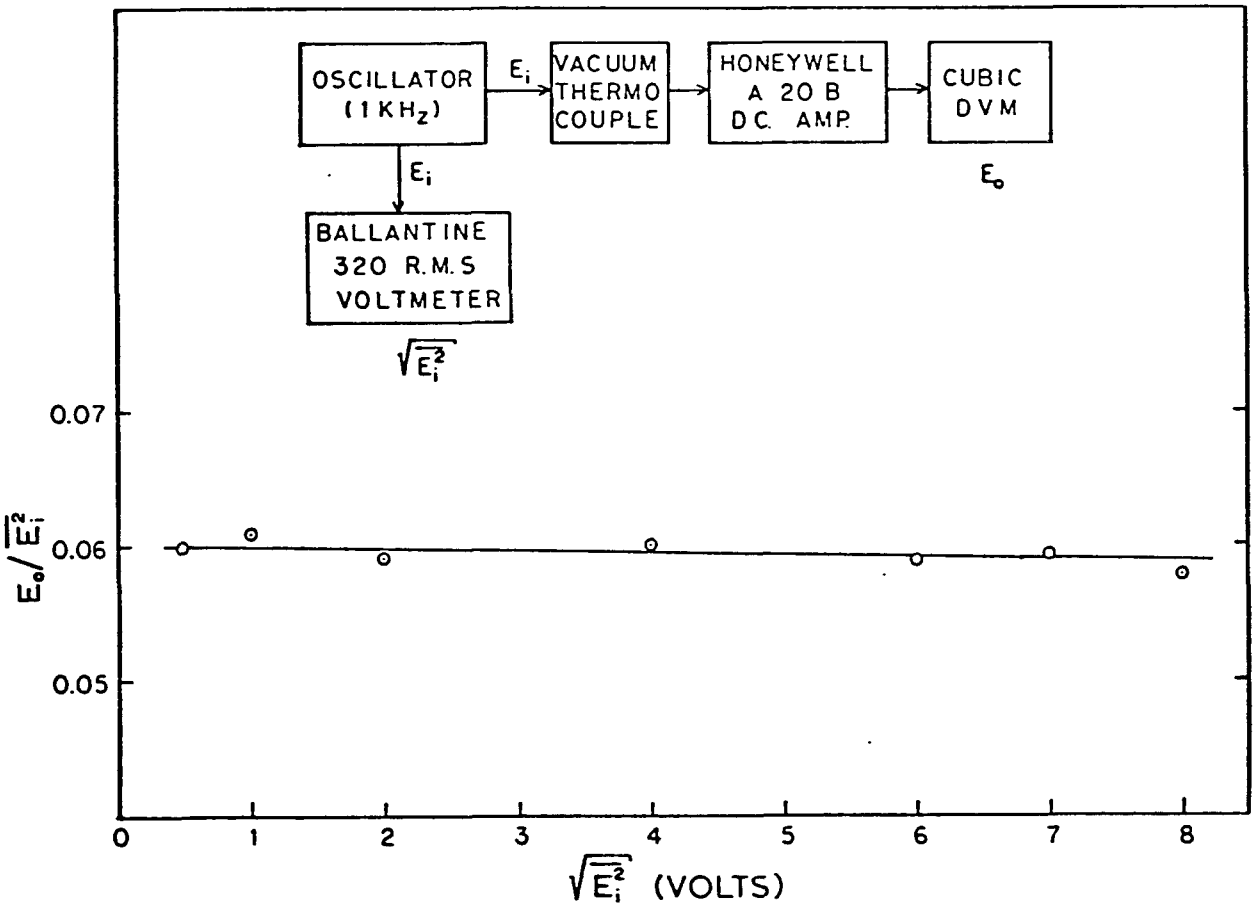

Figure 10. Transfer Characteristics of Vacuum Thermocouples

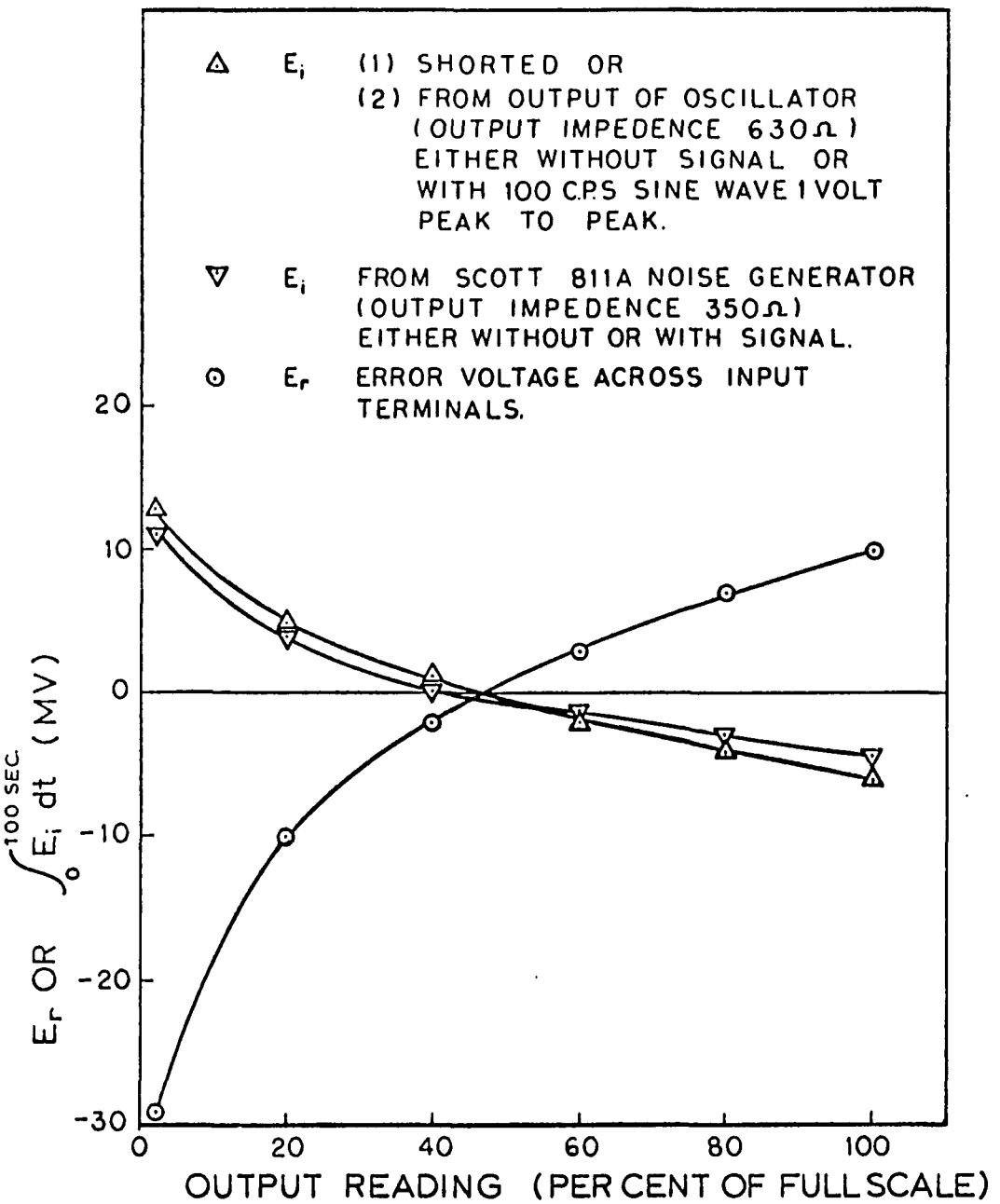

Figure 11. Drift Characteristics of Integrator

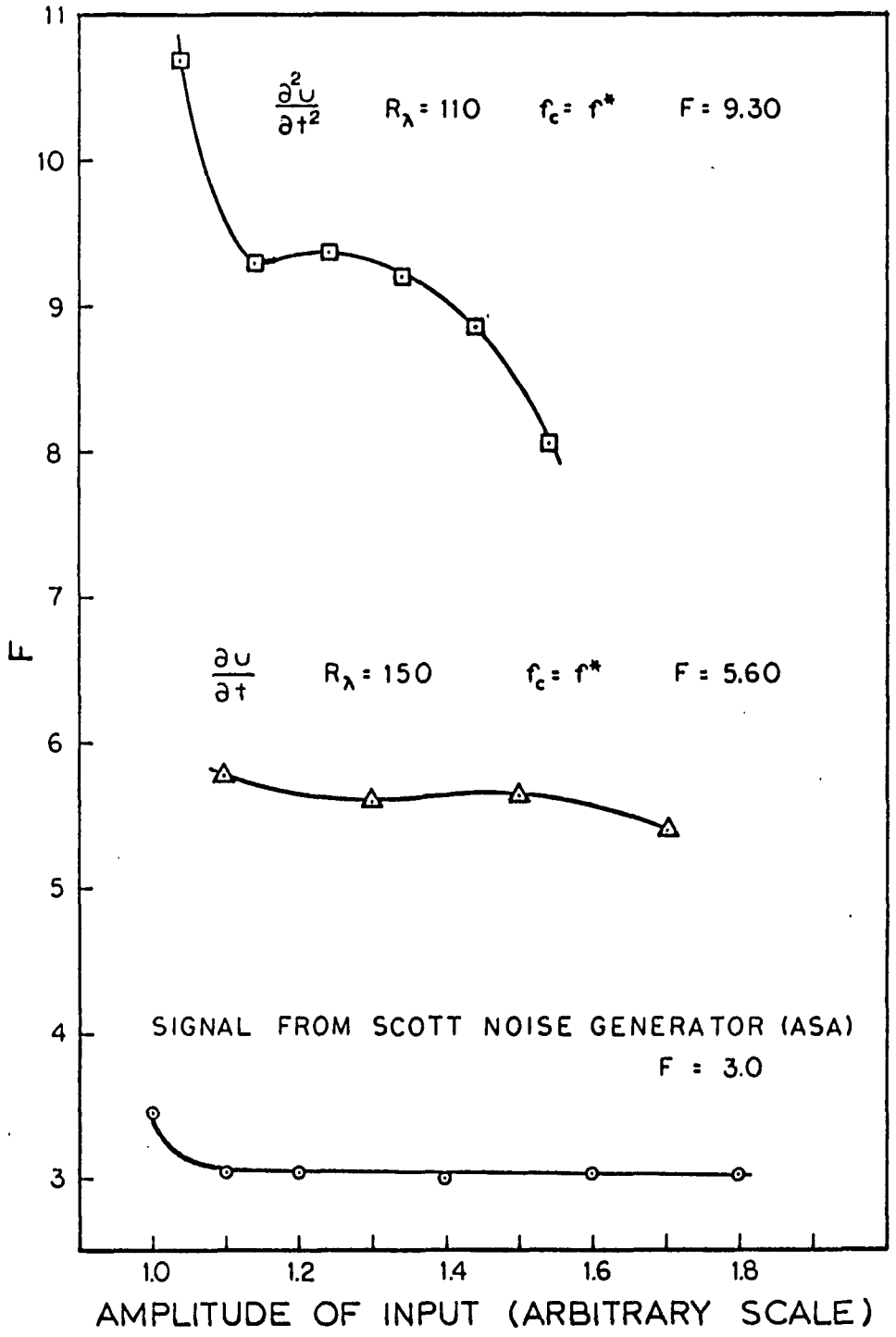

Figure 12. Apparent Flatness Factor vs. Amplitude of Input.

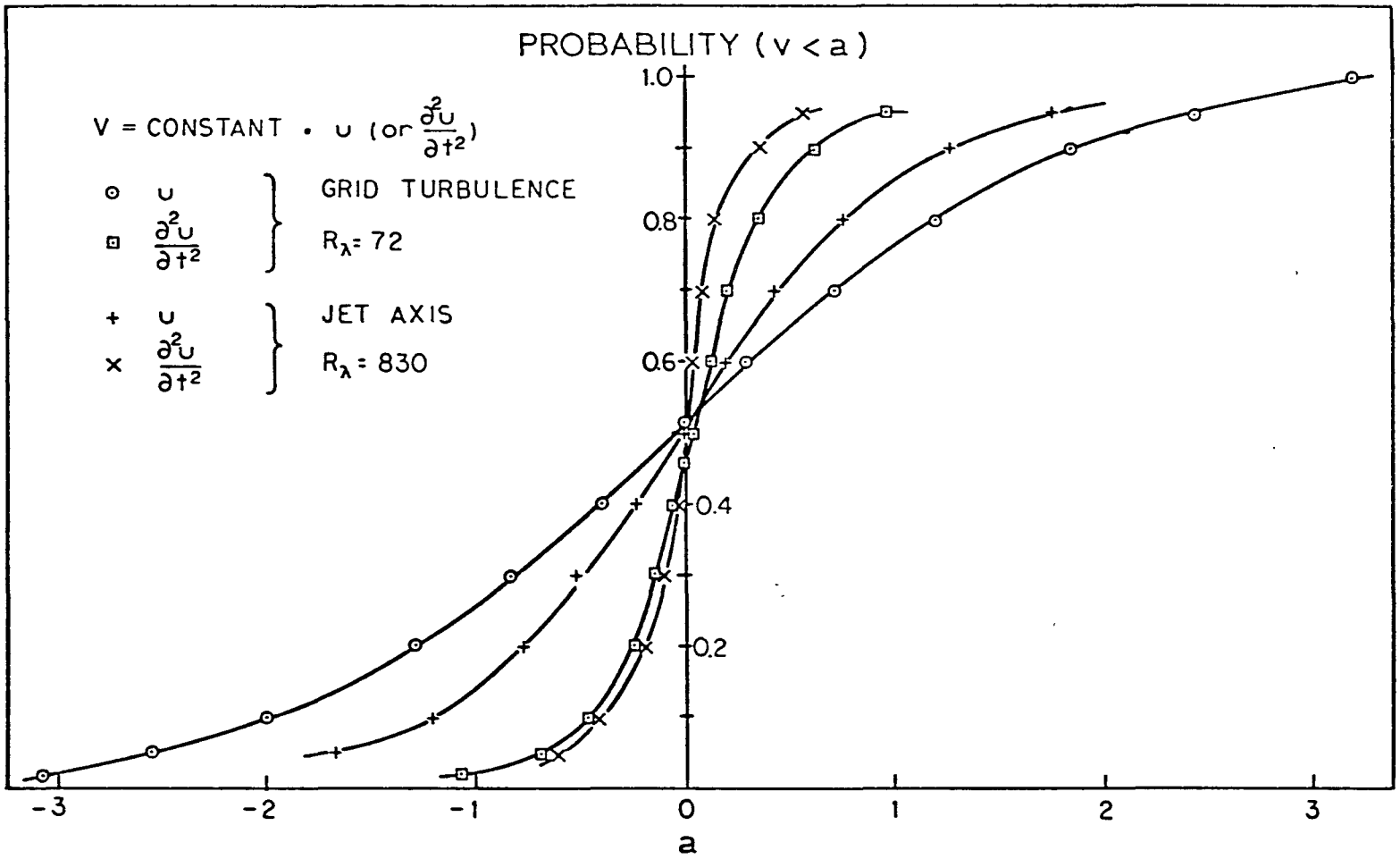

Figure 13. Some Samples of the Data of Probability Distribution

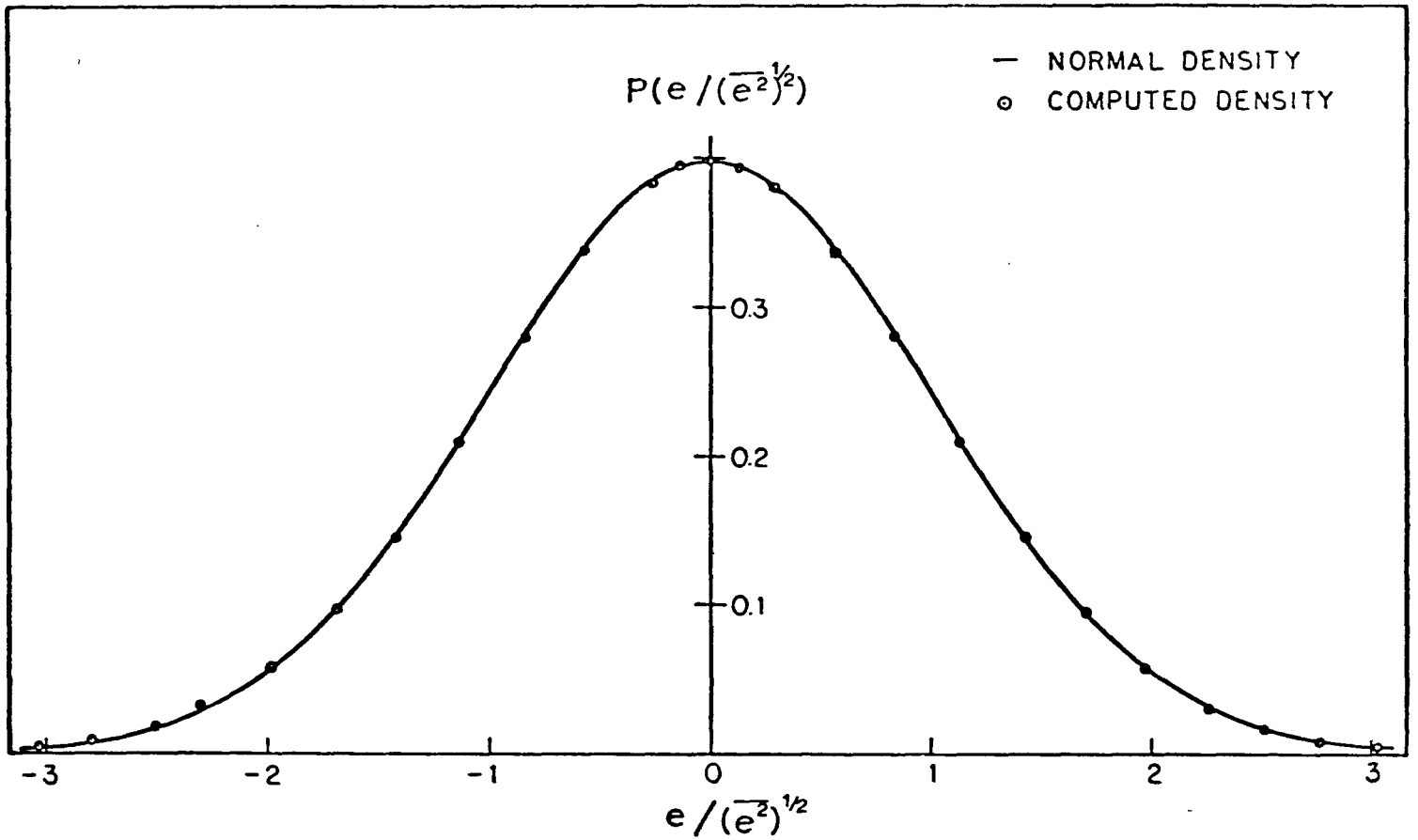

Figure 14. Computed Probability Density from Normal Distribution

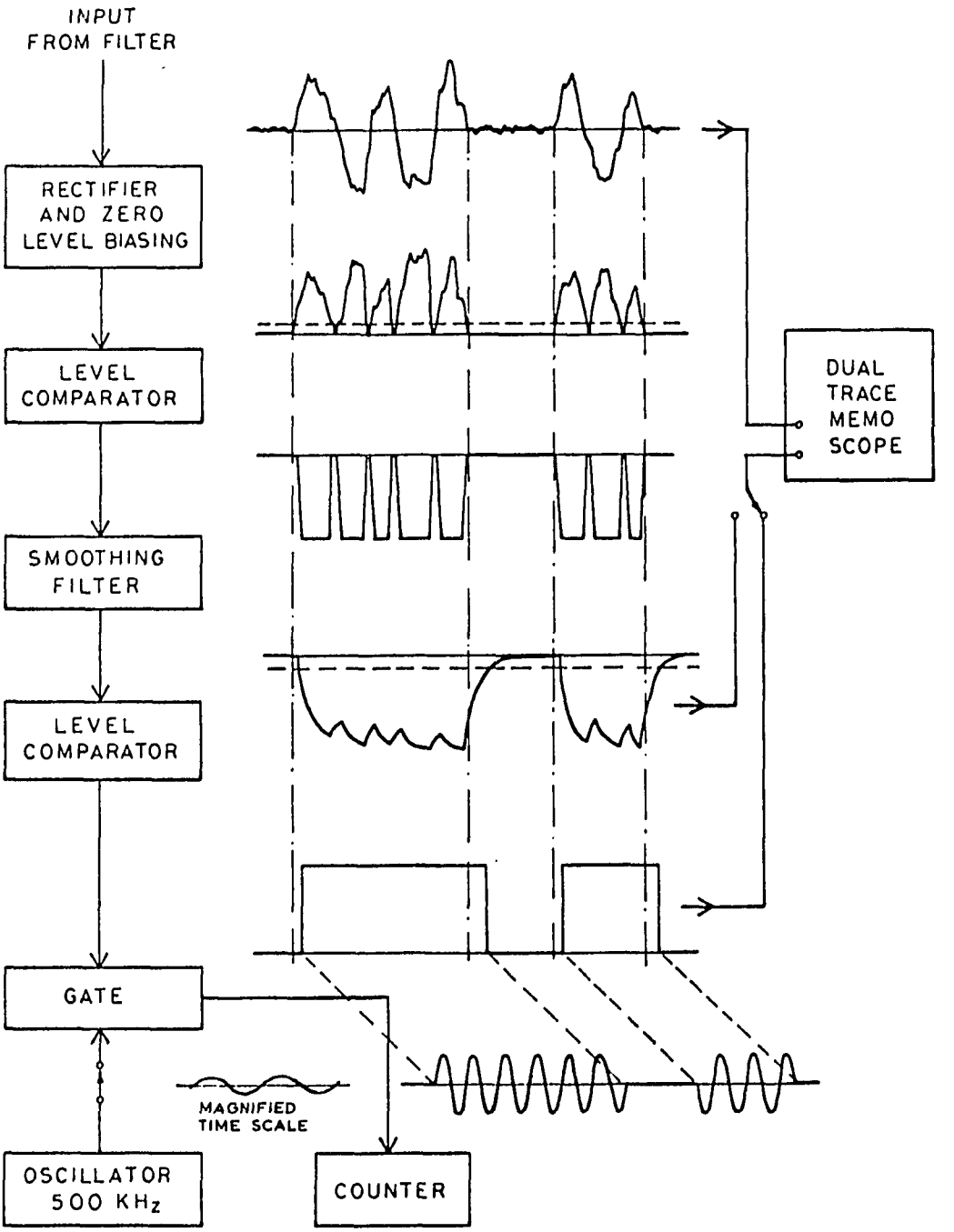

Figure 15. Block Diagram of Intermittency-Measuring Device and Operations on a Hypothetical Signal

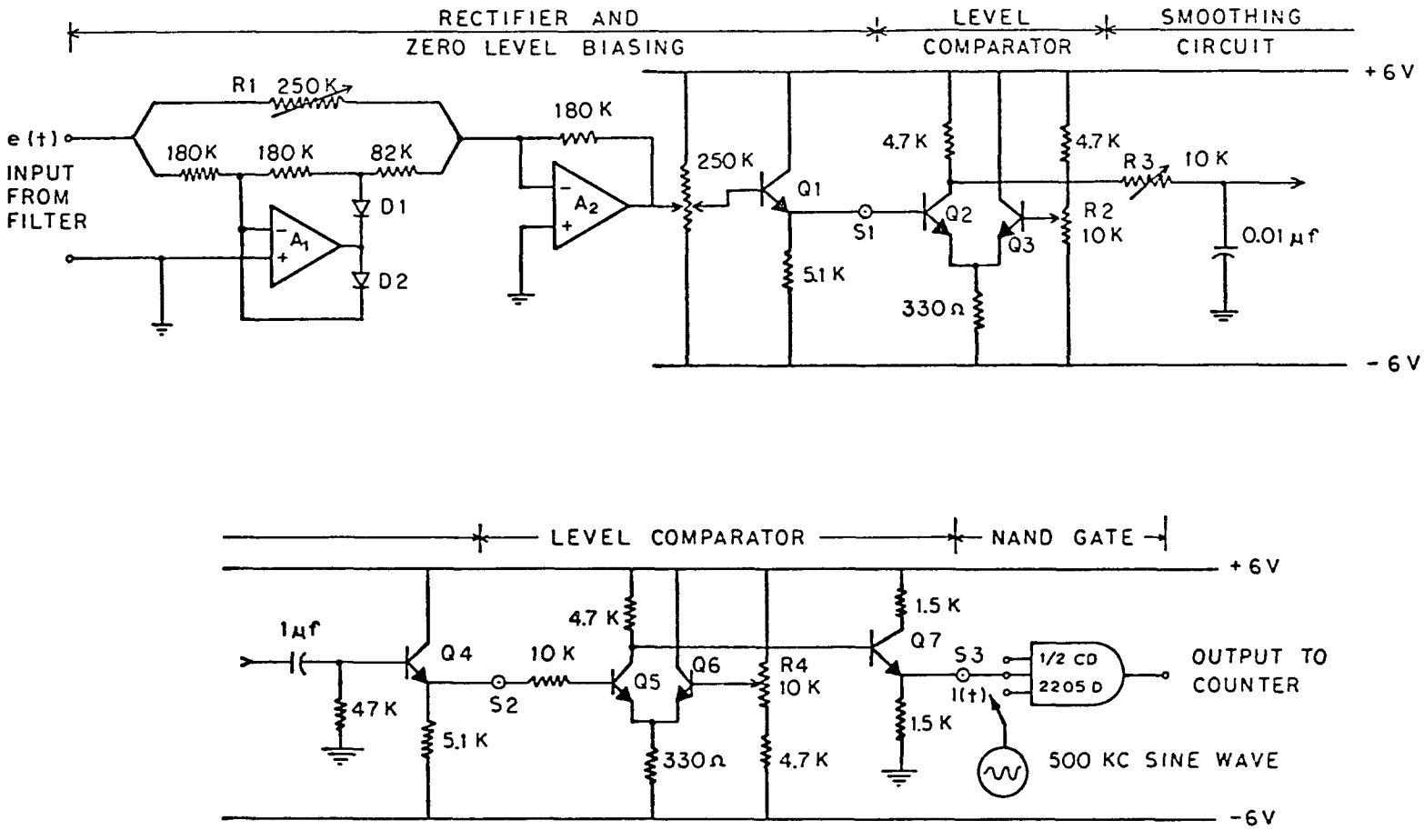

Figure 16. Circuit Diagram of Intermittency-Measuring Device

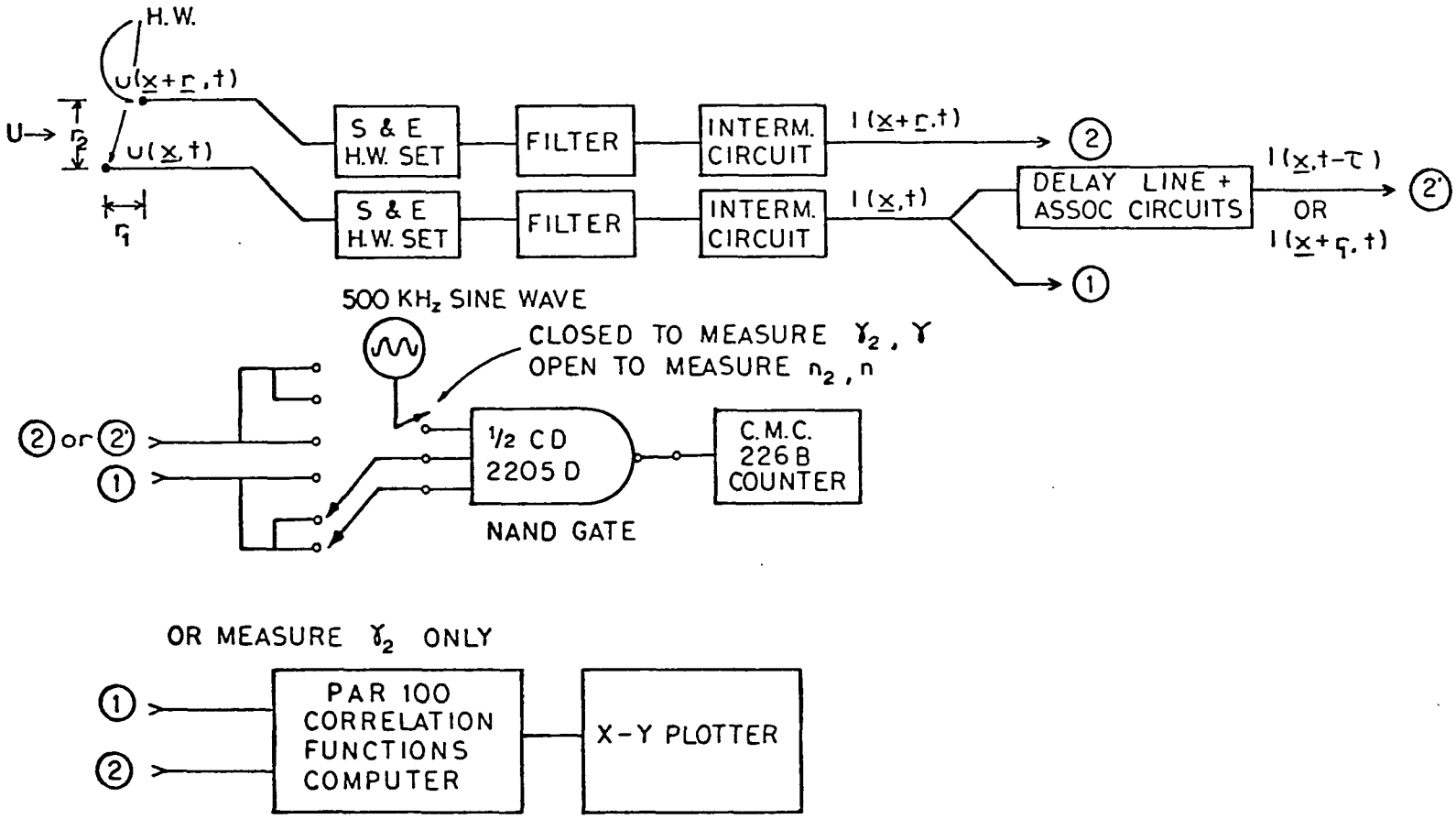

Figure 17. Block Diagram of Instruments to Measure n_2 and γ_2

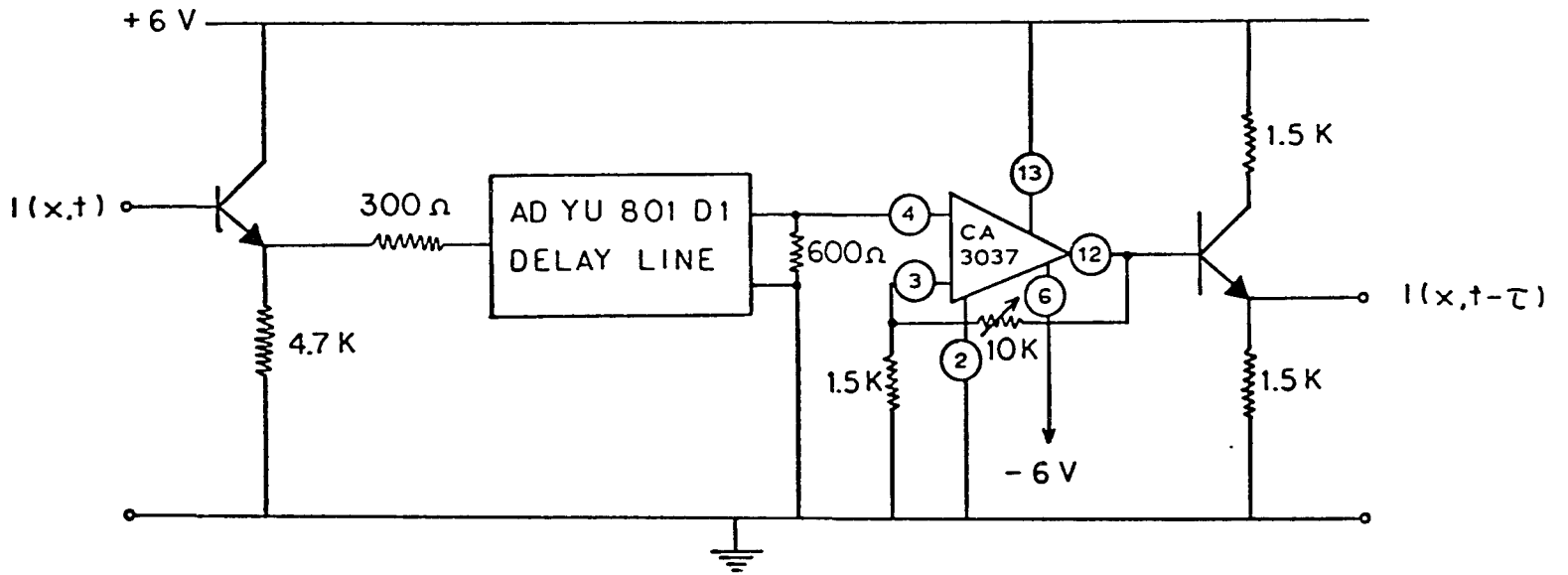

Figure 18. Delay Line and Associated Circuits

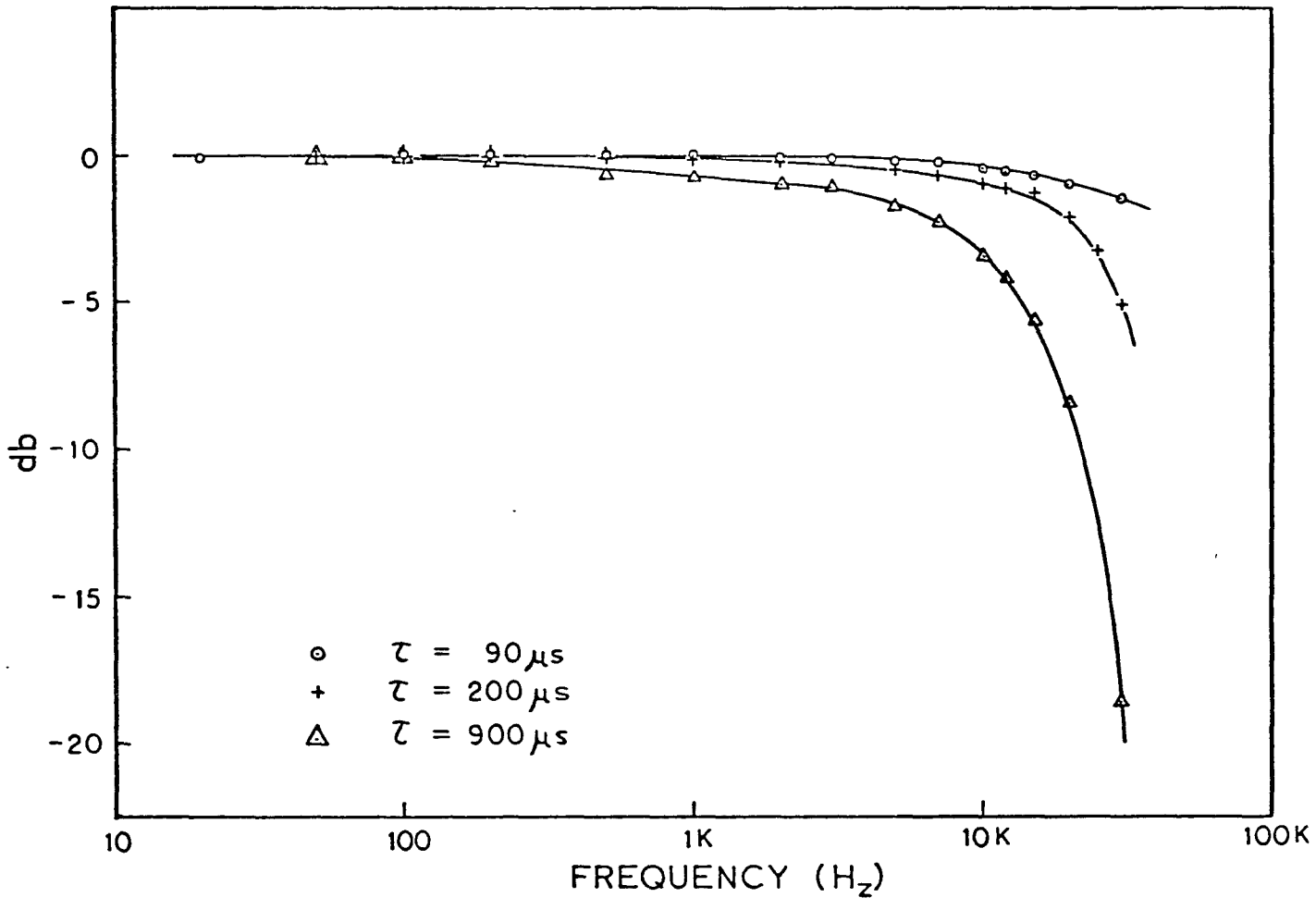

Figure 19. Frequency Response of Delay Line

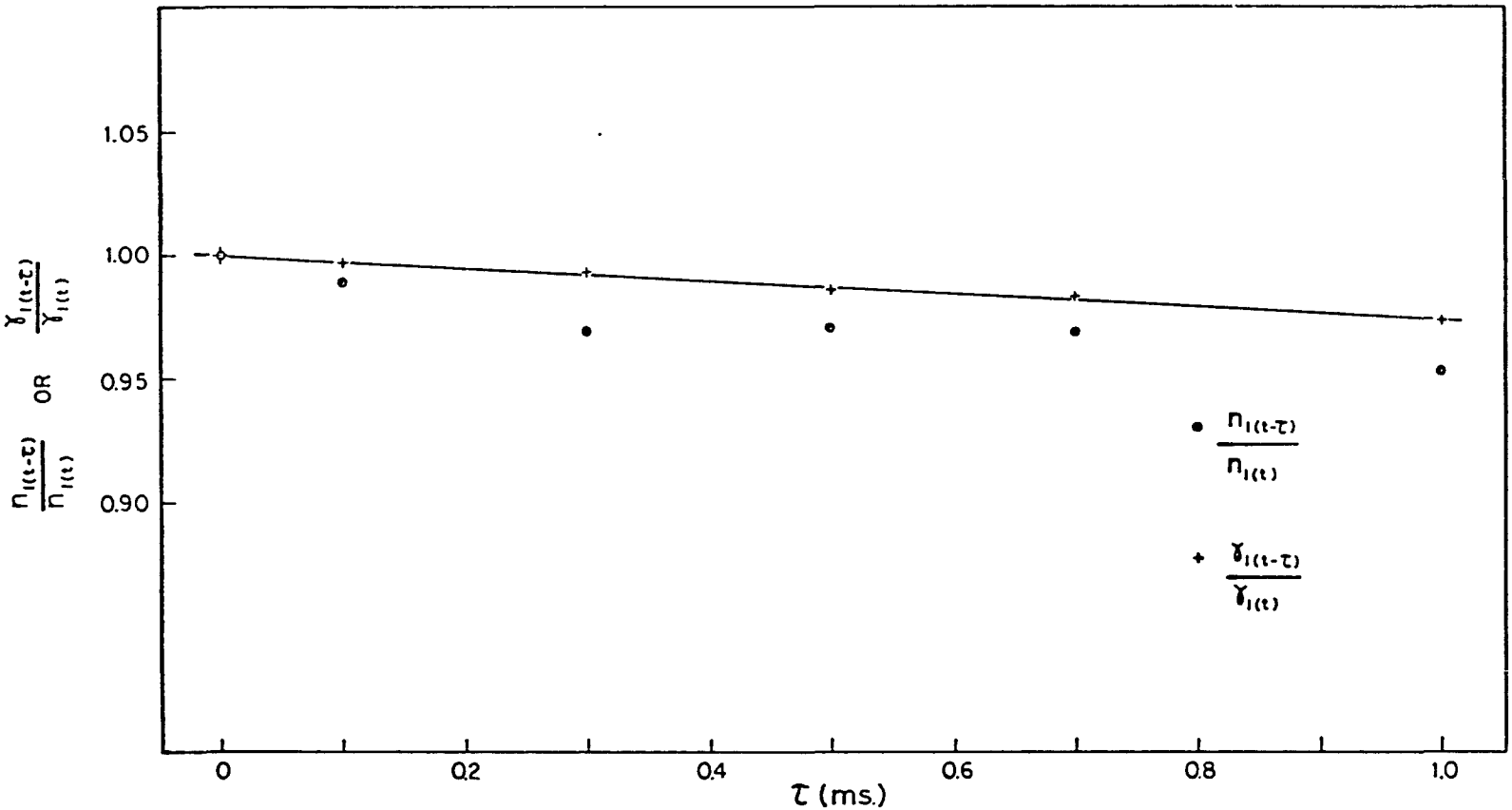

Figure 20. A Performance Check of Delay Line Circuit

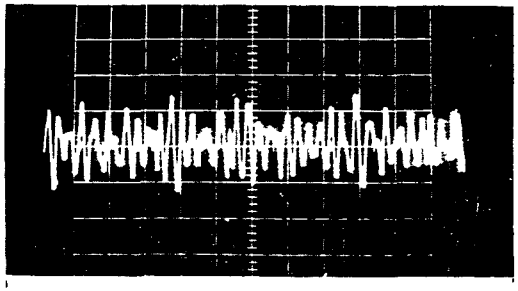

f_m = 200 Hz, $\Delta f/f_m$ = 0.52

Horizontal Scale 20 ms/division

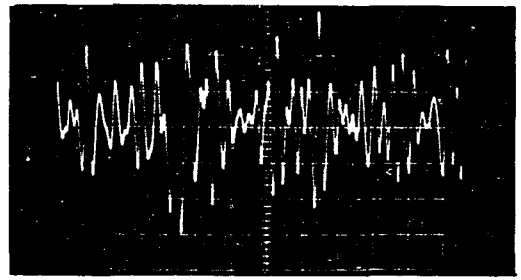

f_m = 1 kHz, $\Delta f/f_m$ = 0.52

Horizontal Scale 4 ms/division

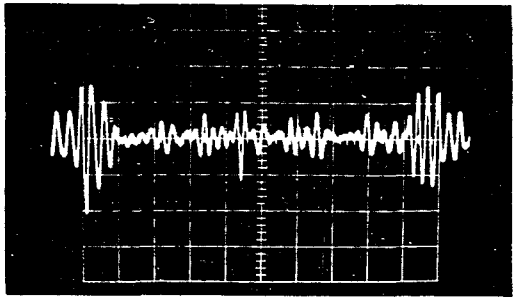

f_m = 6 kHz, $\Delta f/f_m$ = 0.52

Horizontal Scale 1 ms/division

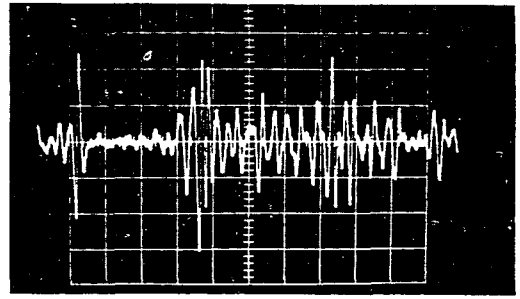

High-Pass Signal, f_c = 5 kHz

Horizontal Scale 1 ms/division

Figure 21. Oscillograms of Band-Pass and High-Pass Signals from a Hot-Wire in a Grid-Generated Turbulence R_λ = 110, f* = 5.9 kHz

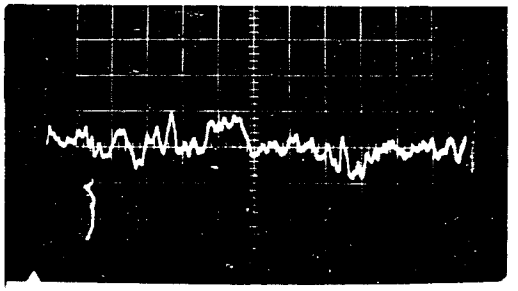

$u(t)$

Horizontal Scale 4 ms/division

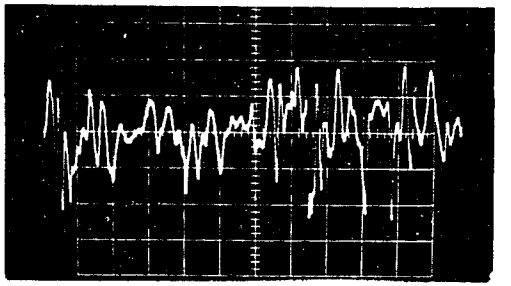

$\frac{\partial u}{\partial t}$

Horizontal Scale 2 ms/division

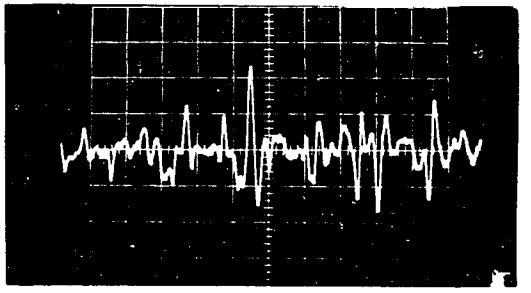

$\frac{\partial^2 u}{\partial t^2}$

Horizontal Scale 1 ms/division

Figure 22. Oscillograms of Velocity Fluctuation and Time Derivatives in a Grid-Generated Turbulence $R_\lambda = 110$, $f^* = 5.9$ kHz

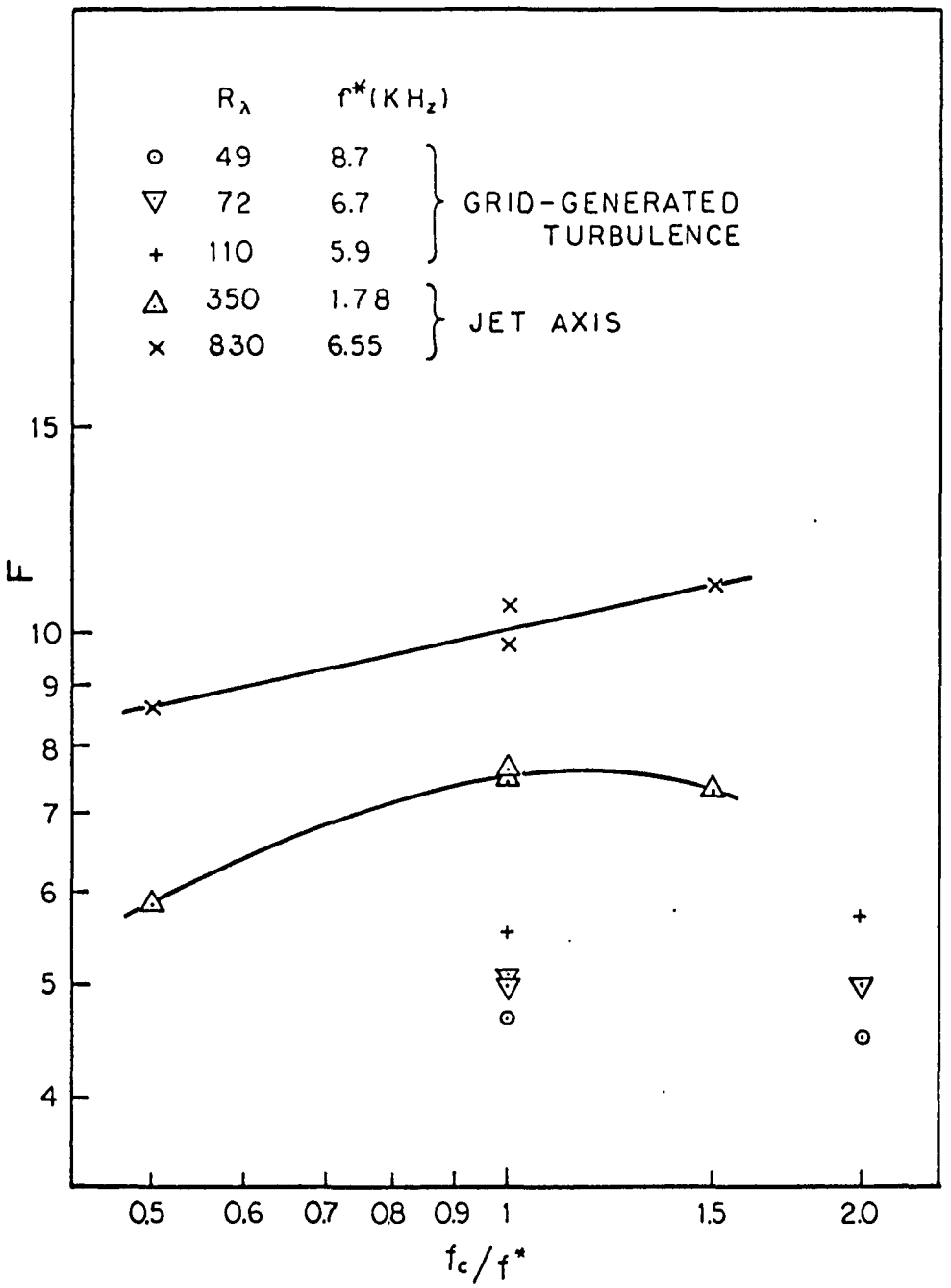

Figure 23. Flatness Factor of $\frac{\partial u}{\partial t}$ as a Function of High Cut-off Frequency f_c/f^*.

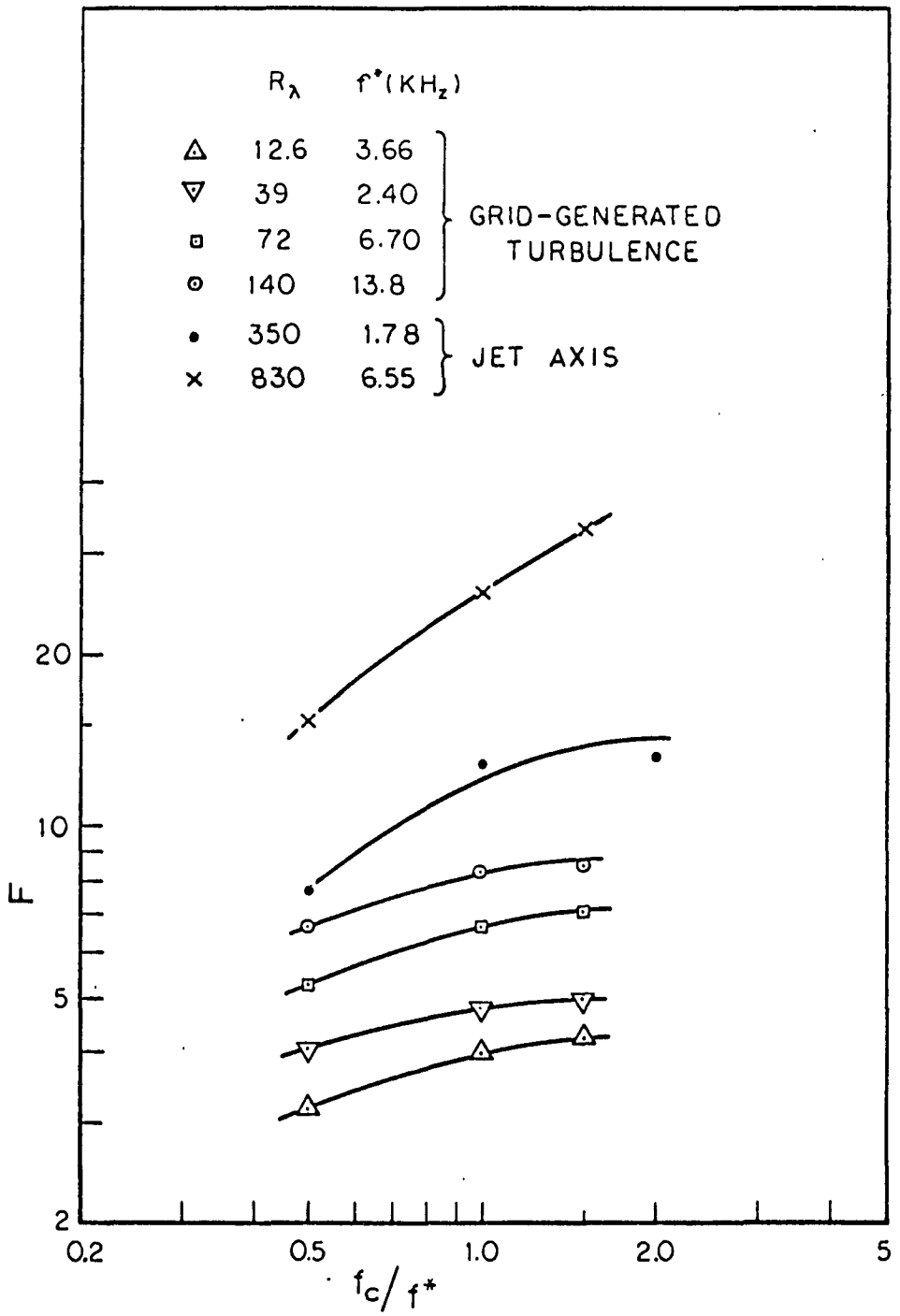

Figure 24. Flatness Factor of $\frac{\partial^2 u}{\partial t^2}$ as a Function of High Cut-off Frequency $\frac{f_c}{f^*}$.

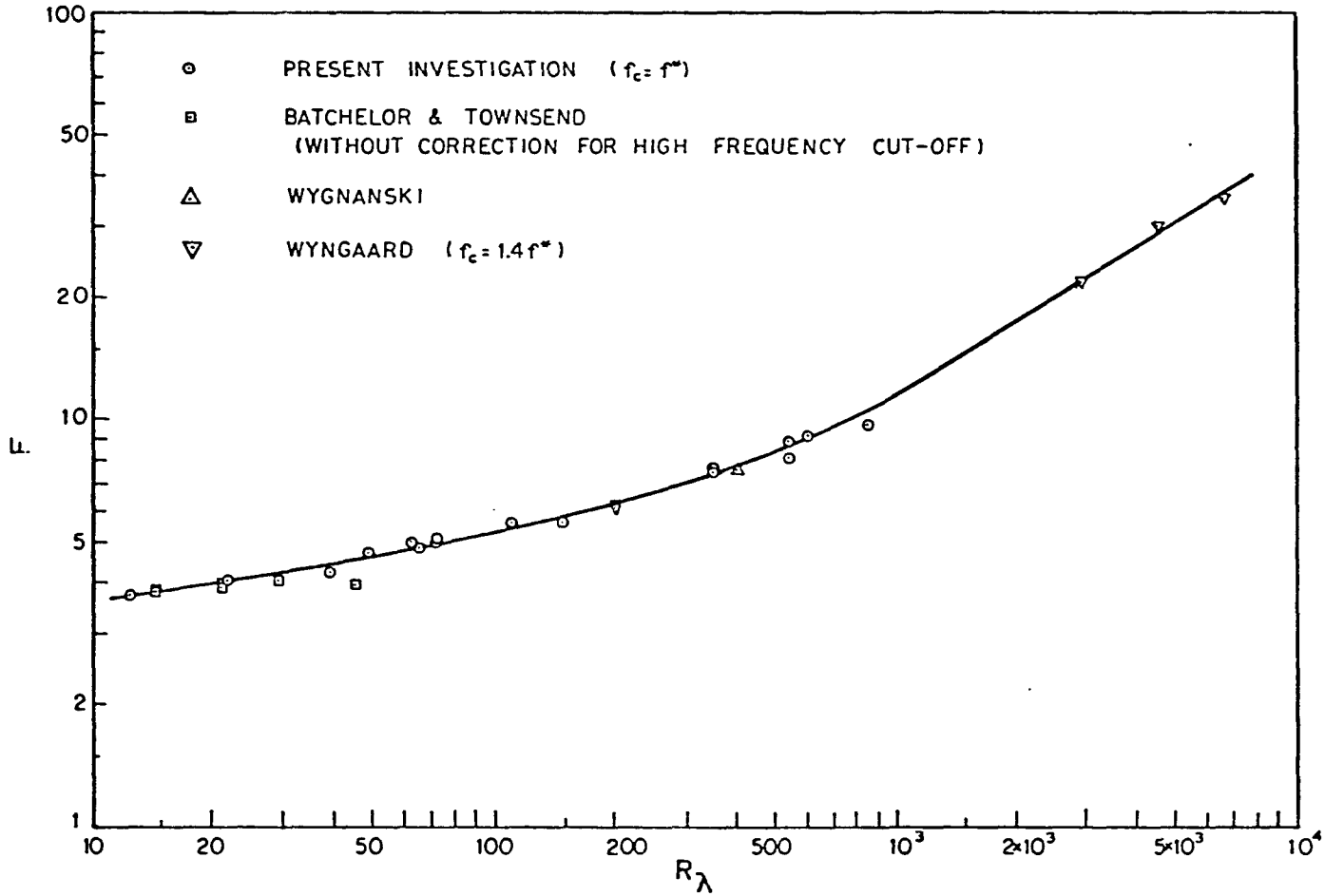

Figure 25. Flatness Factor of $\frac{\partial u}{\partial t}$ as a Function of Reynolds Number R_λ, with $f_c = f^*$.

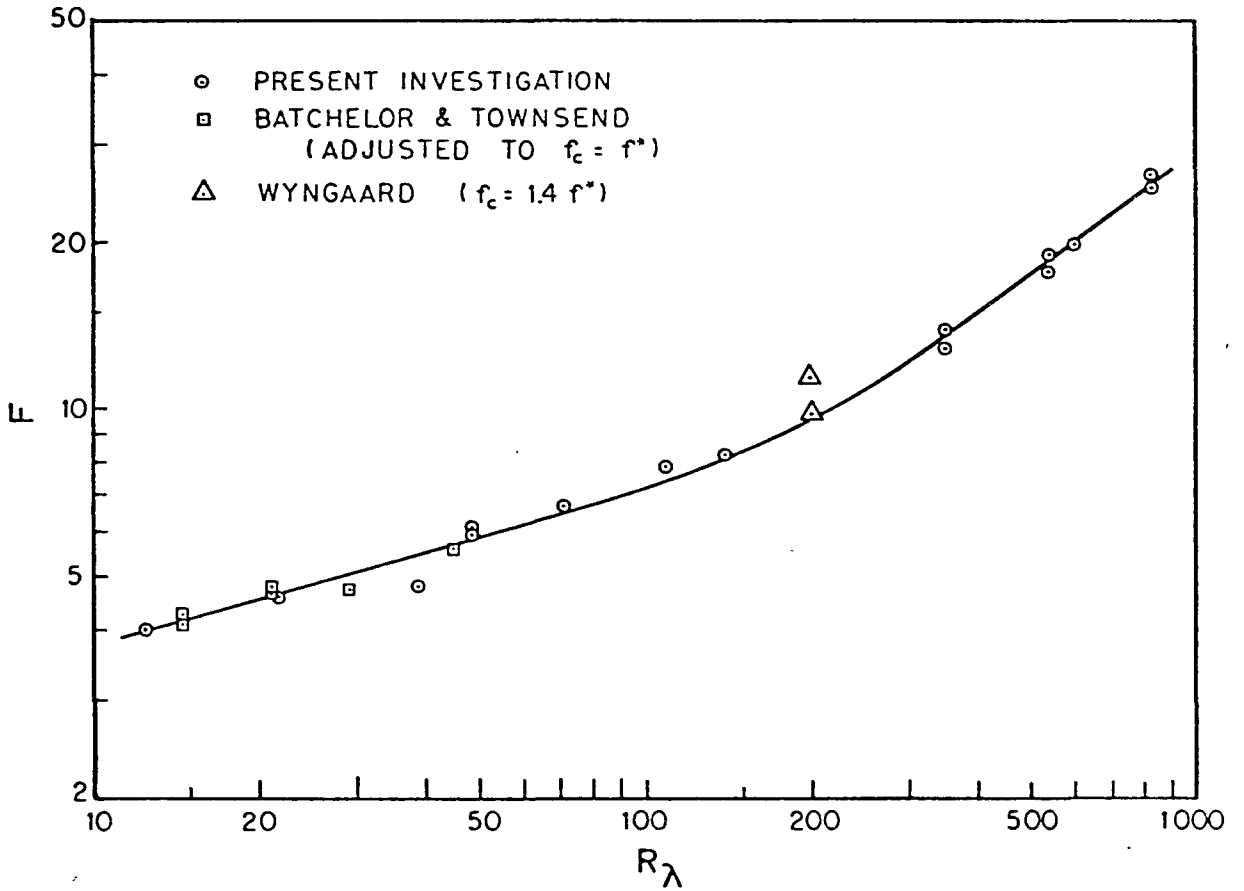

Figure 26. Flatness Factor of $\frac{\partial^2 u}{\partial t^2}$ as a Function of Reynolds Number R_λ, with $f_c = f^*$.

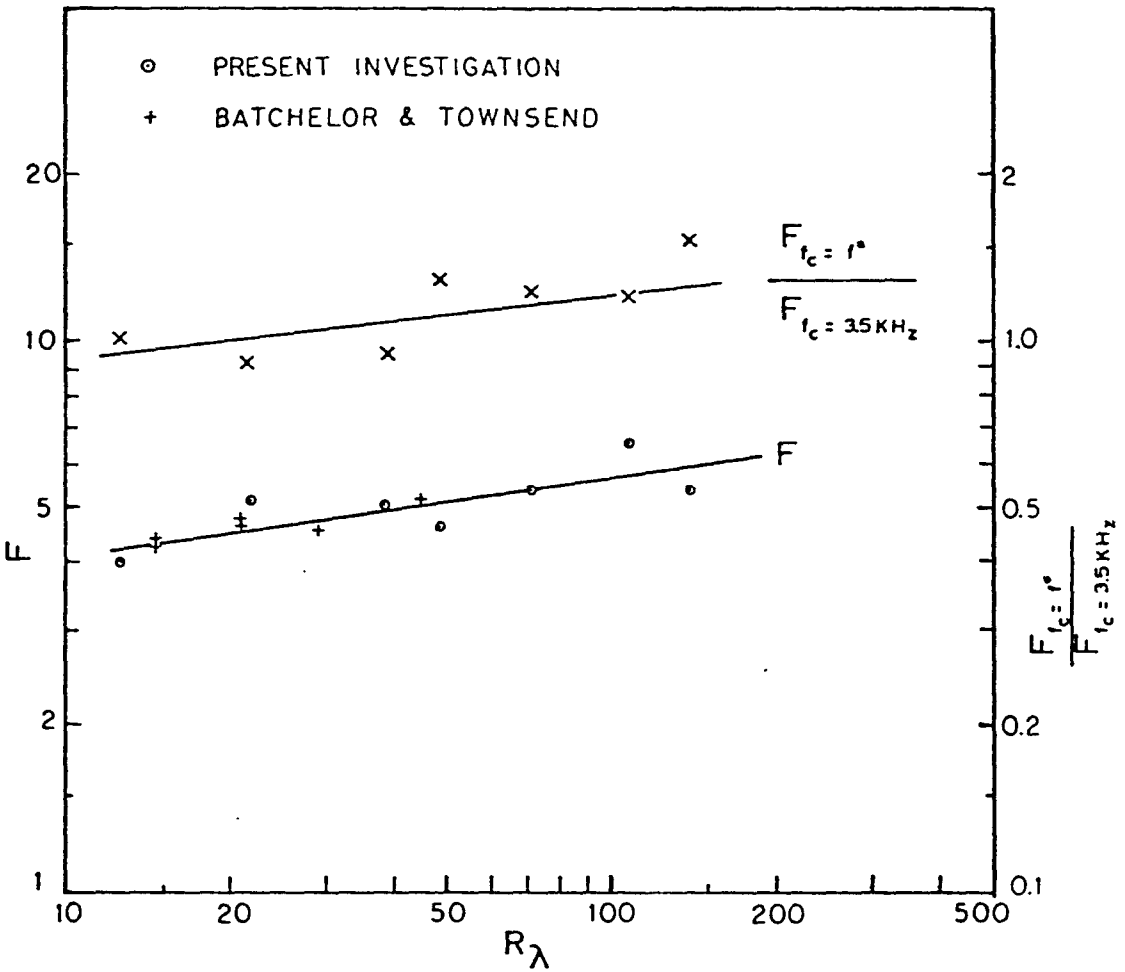

Figure 27. Flatness Factor of $\frac{\partial^2 u}{\partial t^2}$ as a Function of Reynolds Number R_λ, with $f_c = 3.5$ kHz.

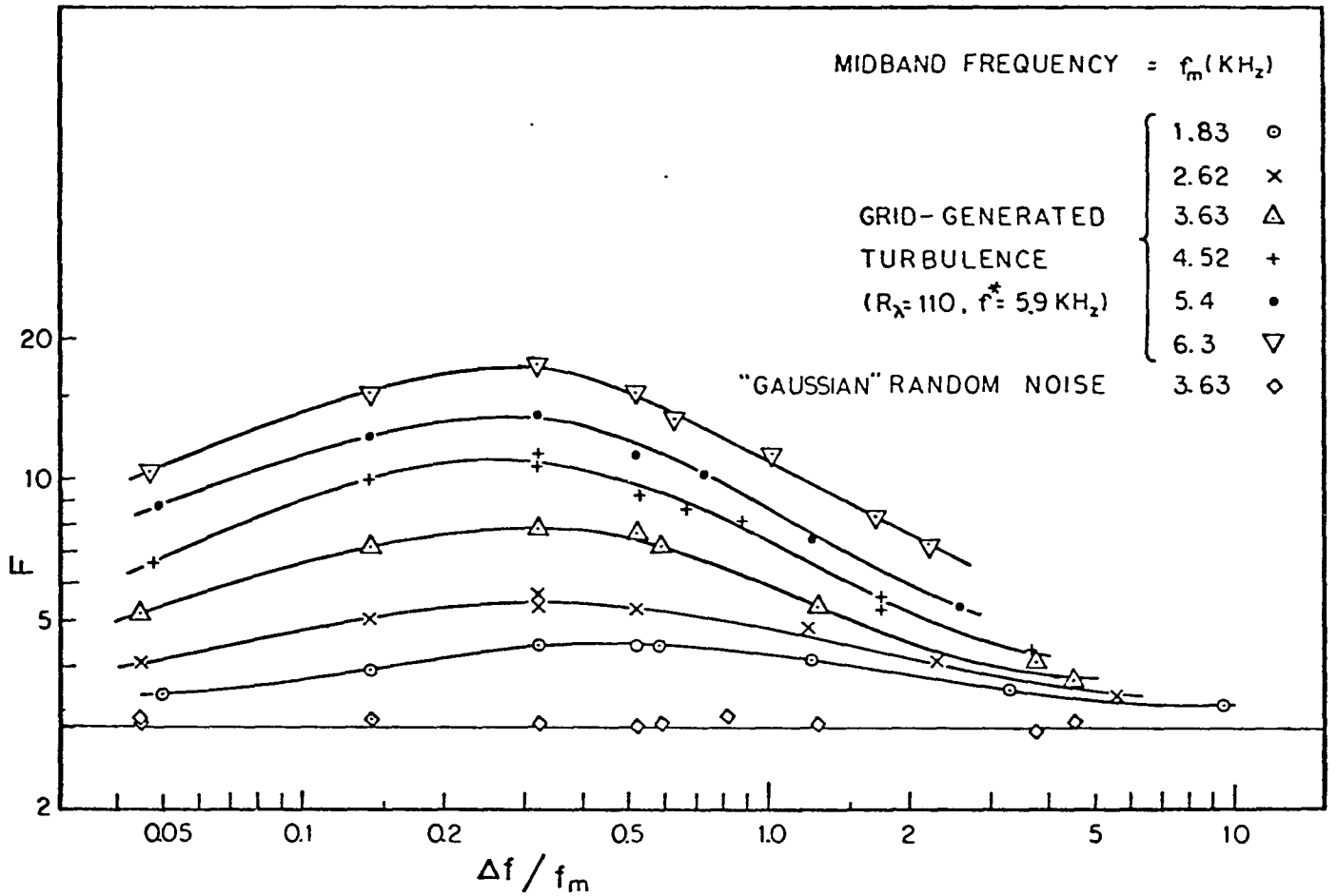

Figure 28. Flatness Factor of Band-pass Signal as a Function of Bandwidth. $\Delta f / f_m$, Log-log Scale

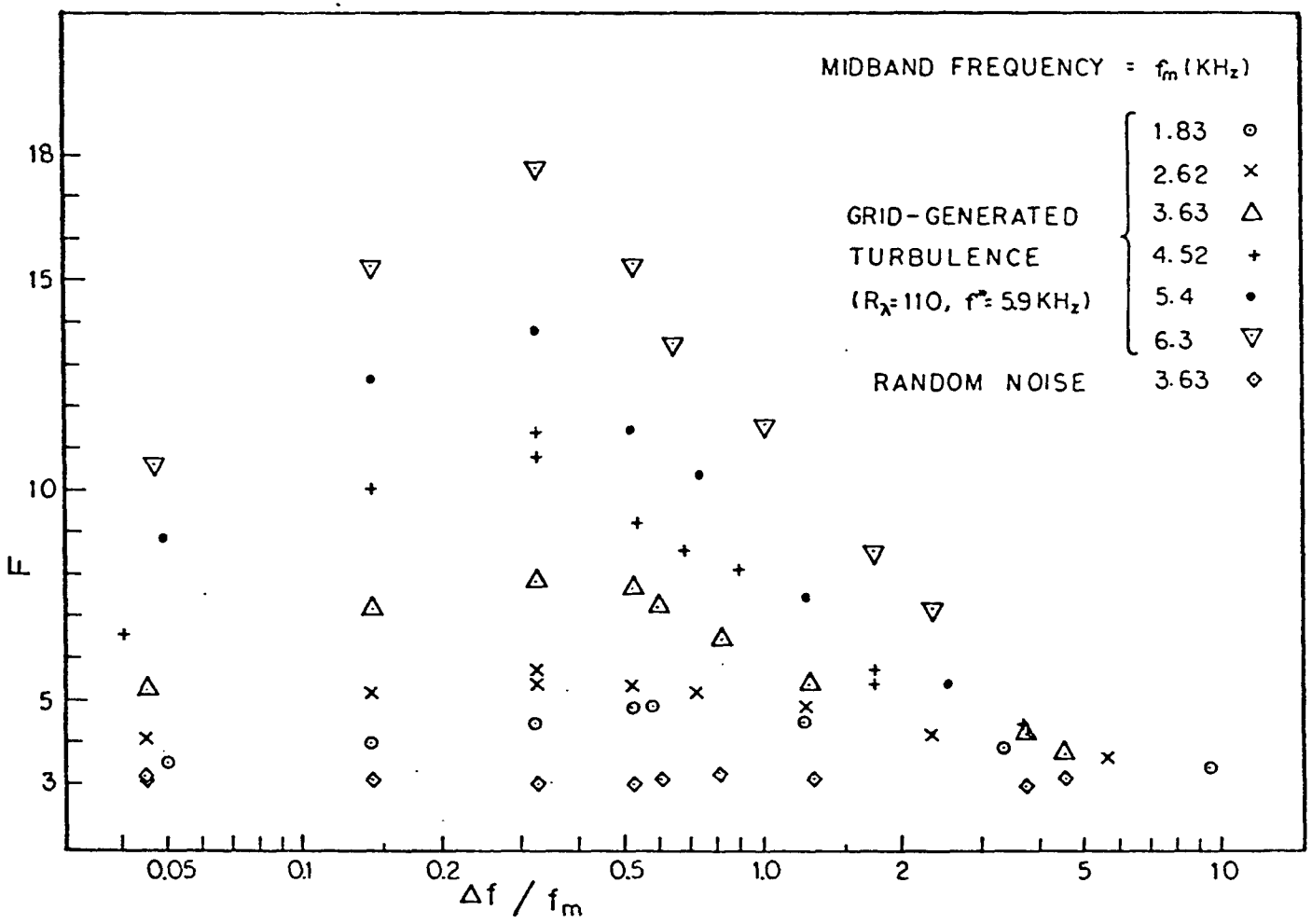

Figure 29. Flatness Factor of Band-pass Signal as a Function of Bandwidth $\Delta f / f_m$, Semi-log Scale

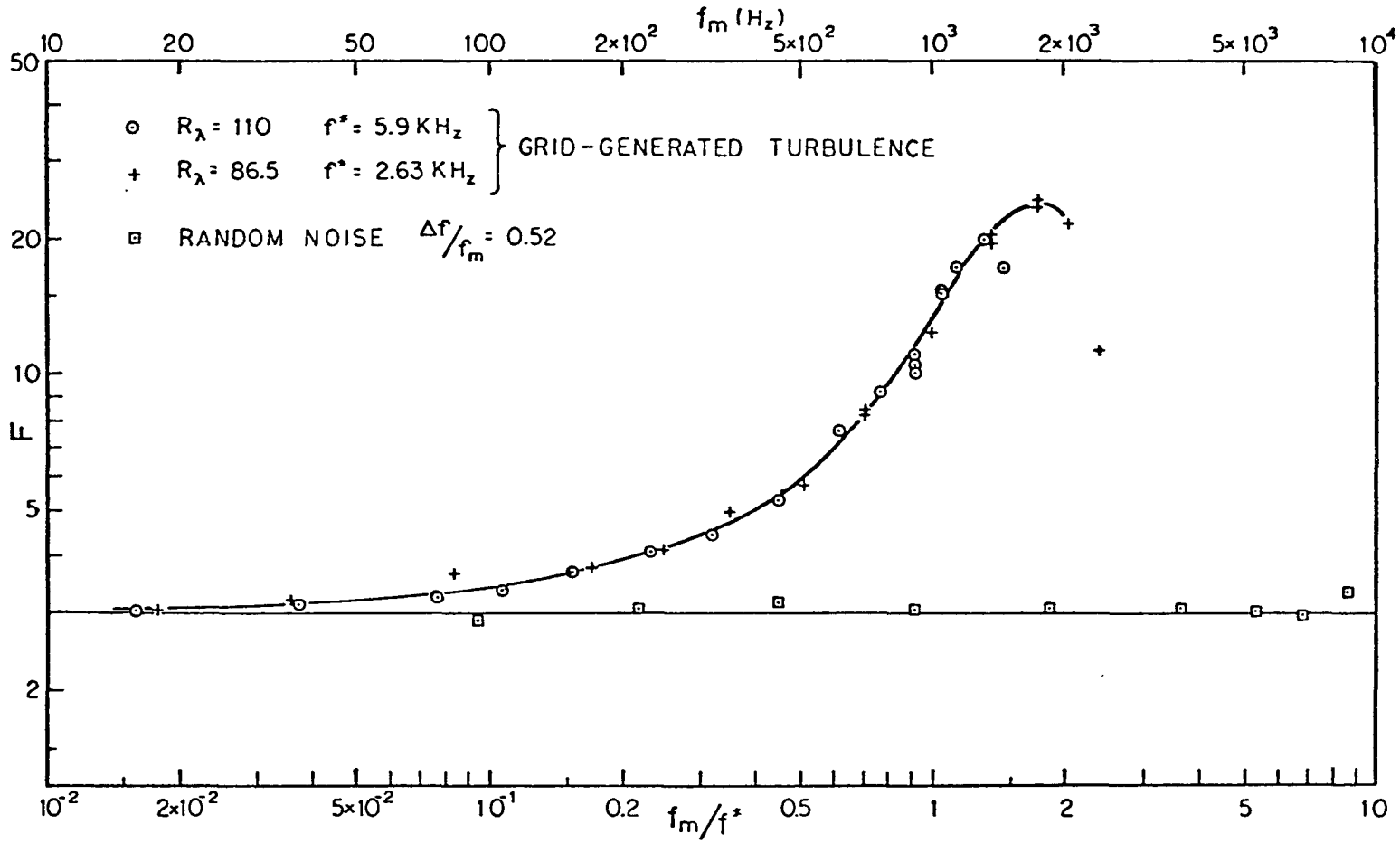

Figure 30. Flatness Factor of Band-pass Signal as a Function of Midband Frequency f_m/f^*.

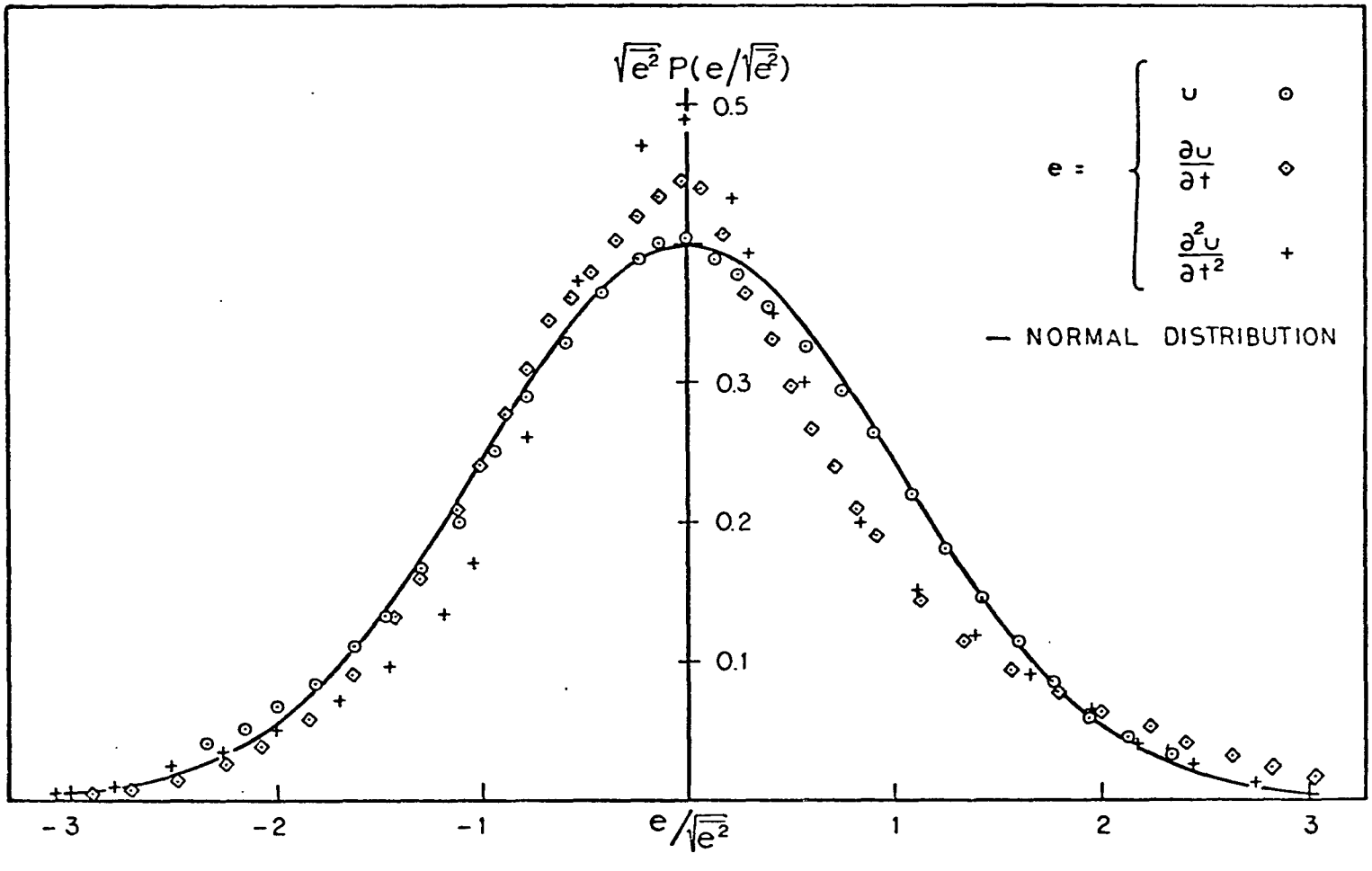

Figure 31. Probability Densities of u, $\partial u/\partial t$, and $\partial^2 u/\partial t^2$ in a Grid-generated Turbulence, $R_\lambda = 72$.

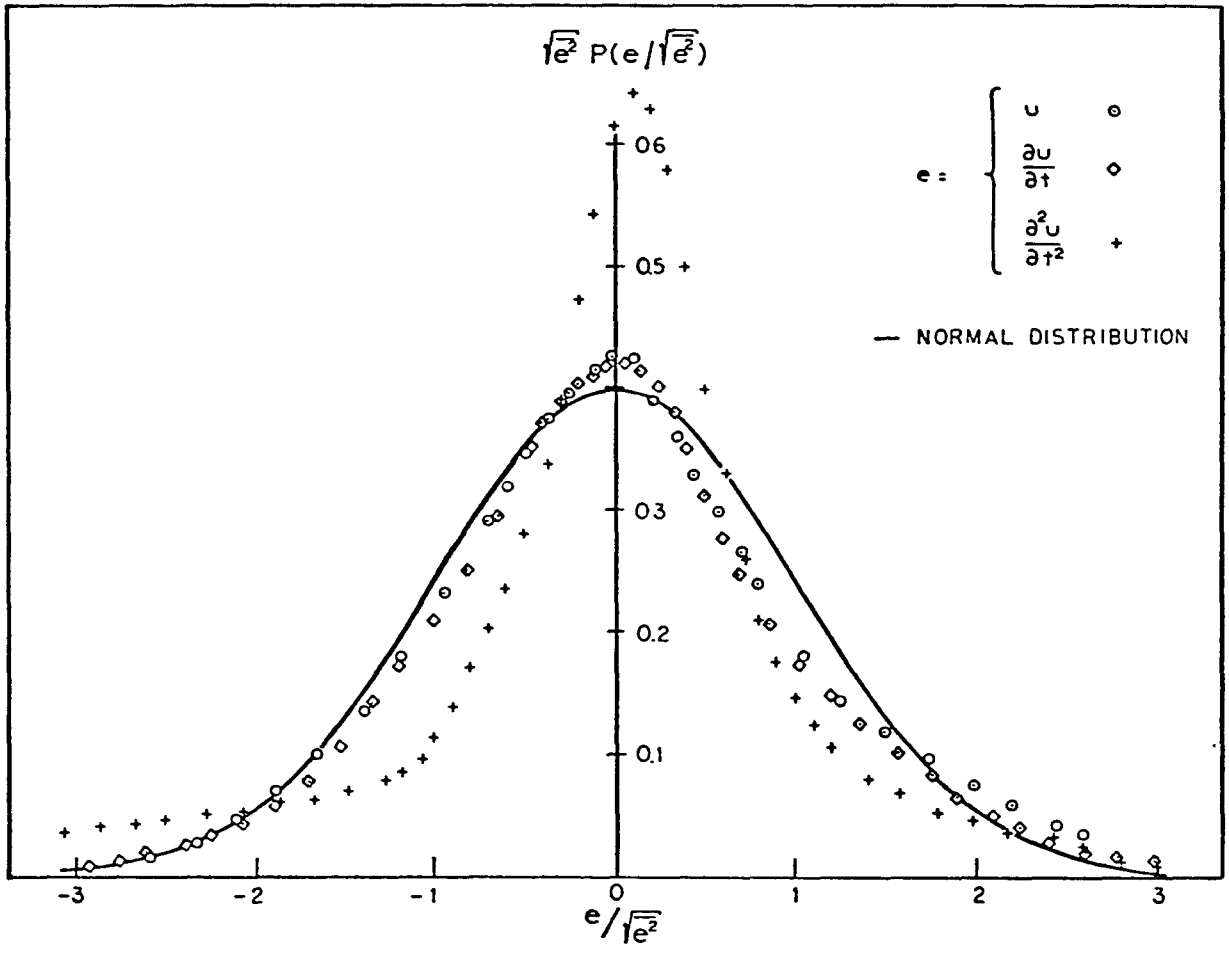

Figure 32. Probability Densities of u, $\partial u/\partial t$, and $\partial^2 u/\partial t^2$ on the Axis of a Round Jet, $R_\lambda = 830$.

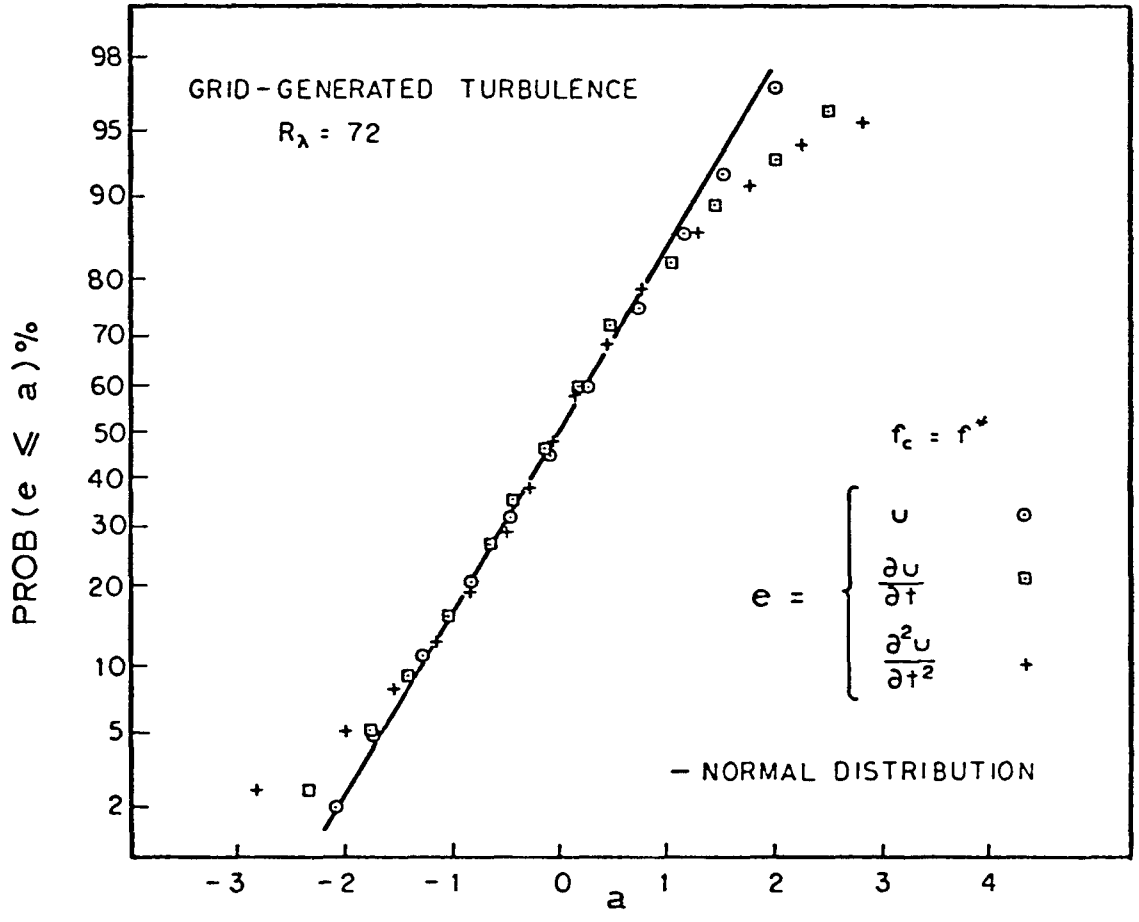

Figure 33. Probability Distributions of u, $\partial u/\partial t$ and $\partial^2 u/\partial t^2$ in a Grid-generated Turbulence, $R_\lambda = 72$.

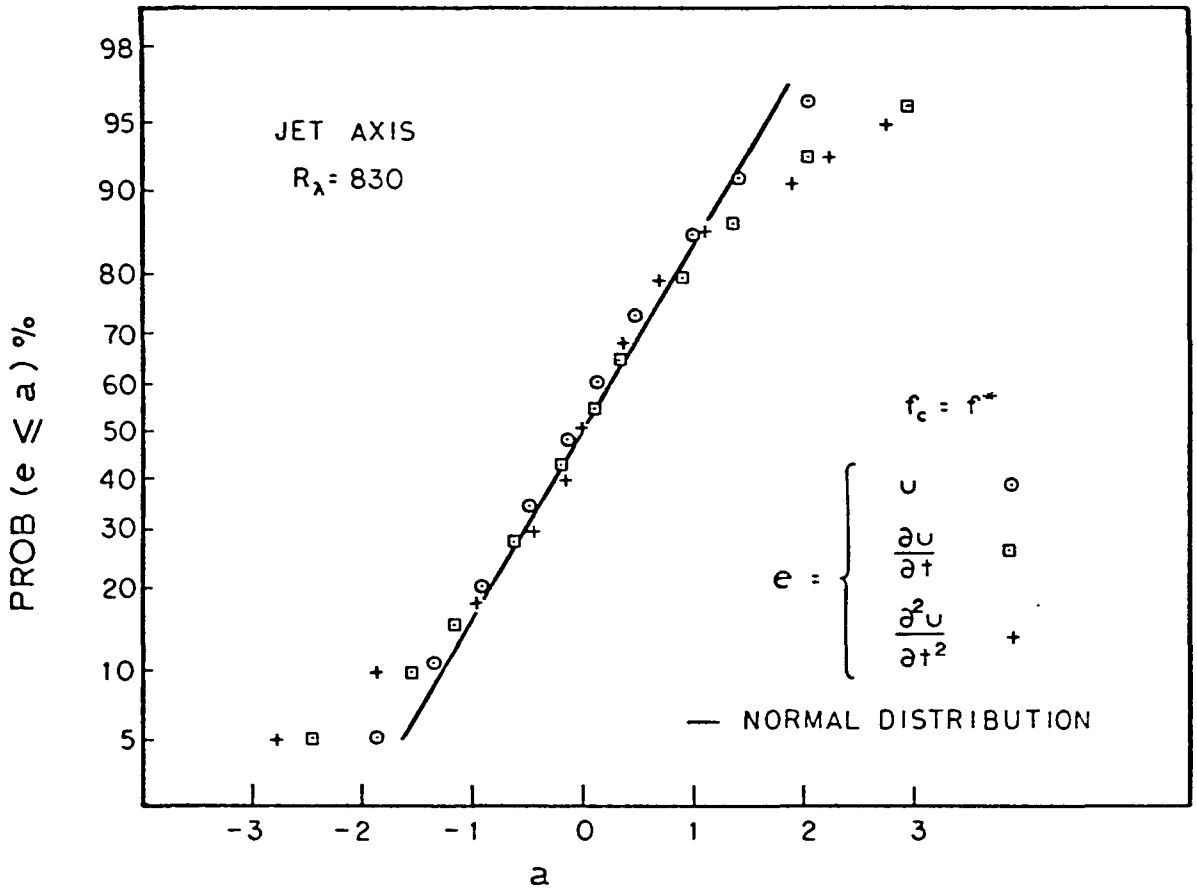

Figure 34. Probability Distributions of u, $\partial u/\partial t$, and $\partial^2 u/\partial t^2$ on the Axis of a Round Jet, $R_\lambda = 830$.

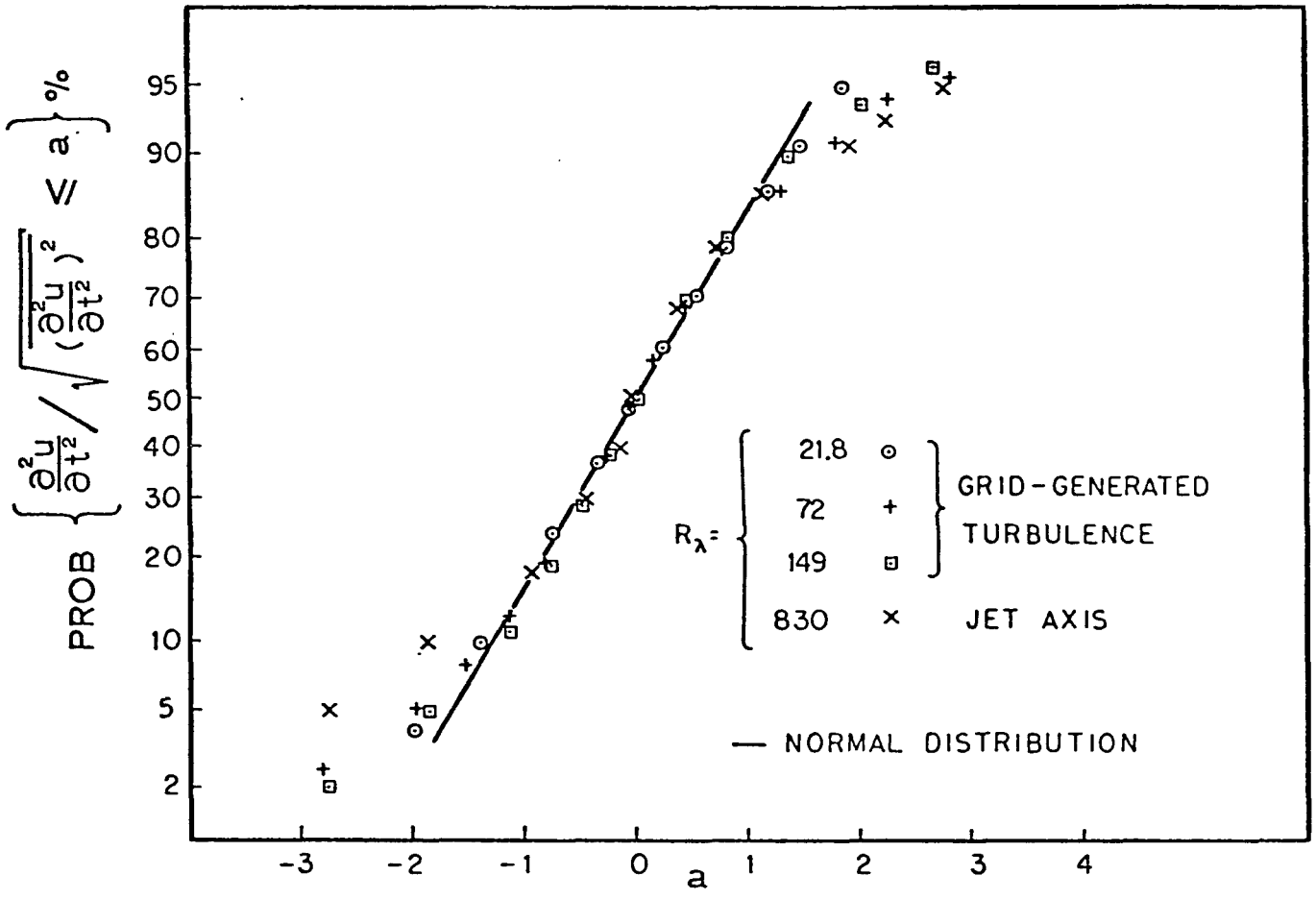

Figure 35. Probability Distributions of $\frac{\partial^2 u}{\partial t^2}$ at Various Reynolds Numbers.

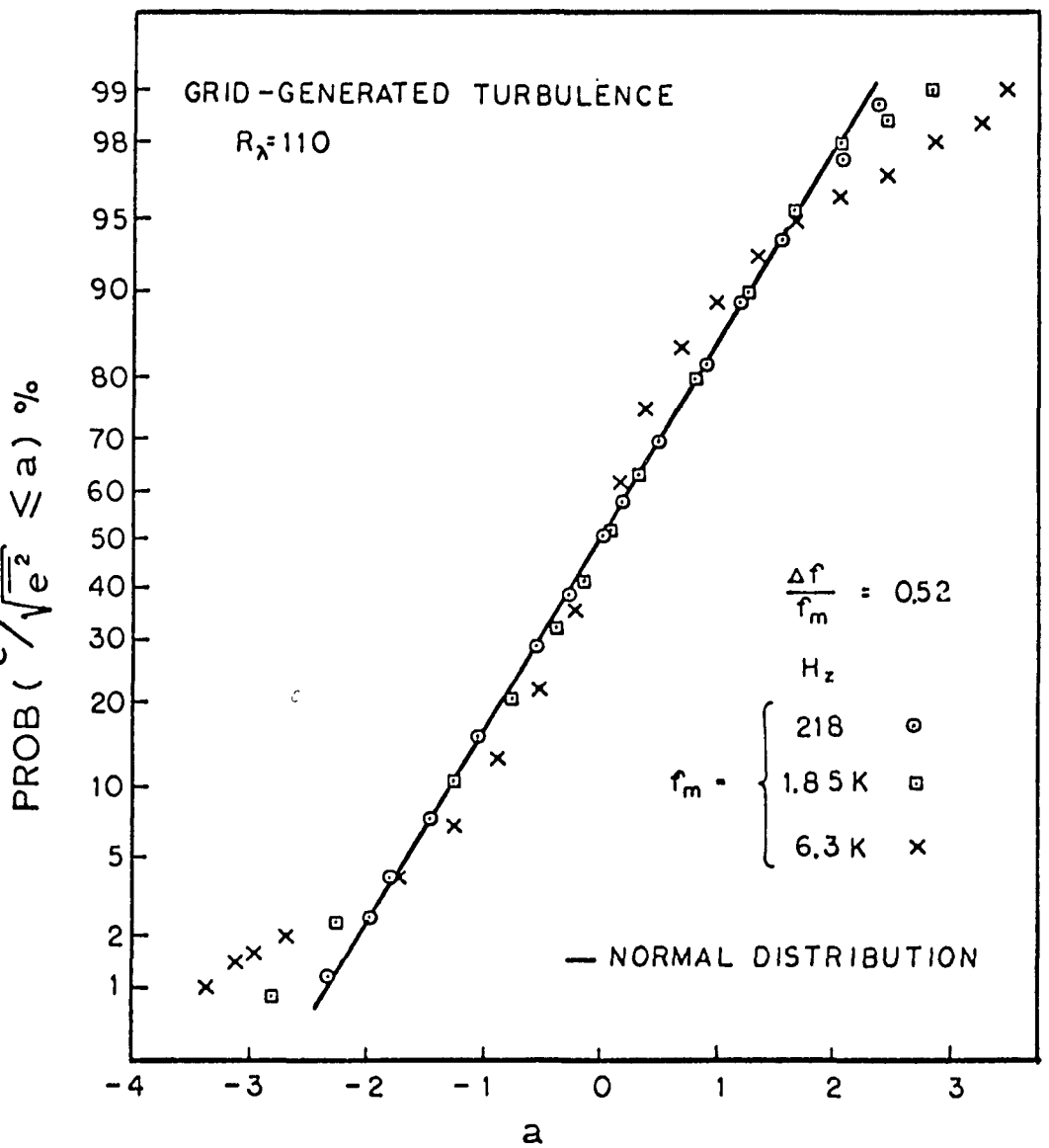

Figure 36. Probability Distribution of Band-pass Signal from a Grid-Generated Turbulence, R_λ = 110.

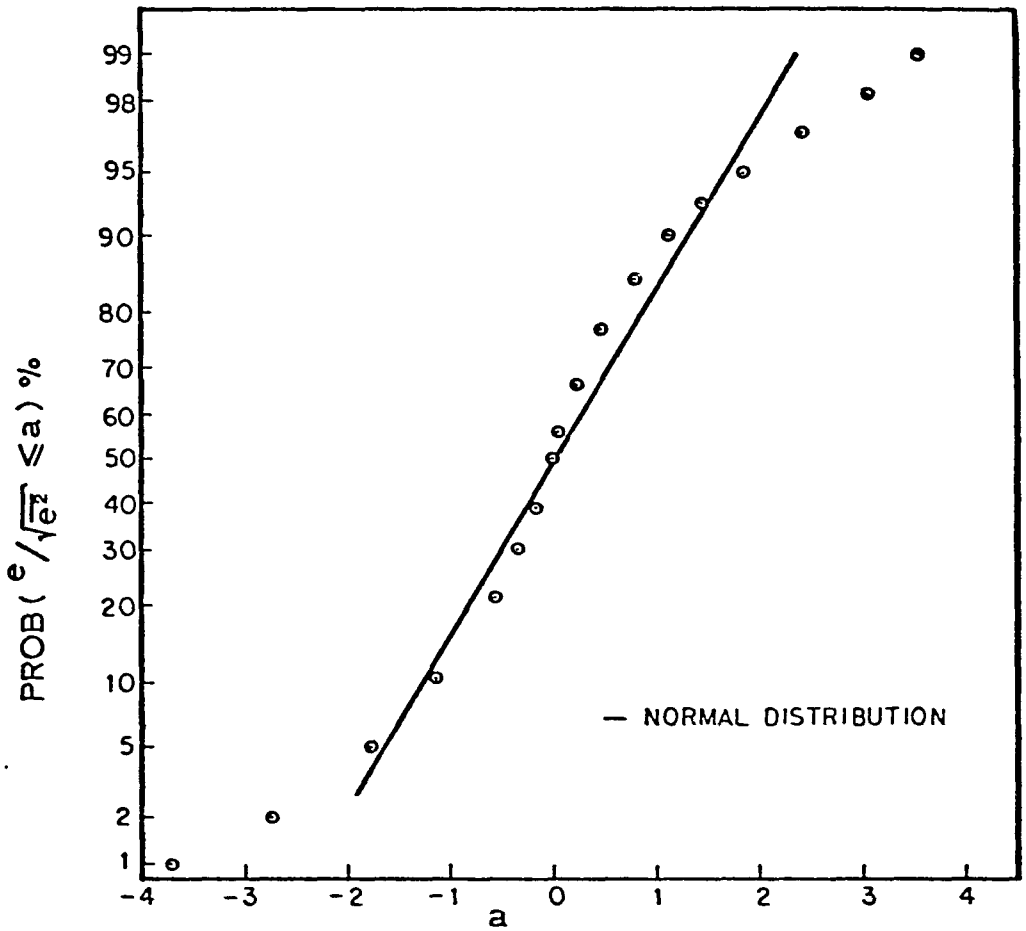

Figure 37. Probability Distribution of High-pass Signal from a Butterworth Filter, f_c = 5kHz

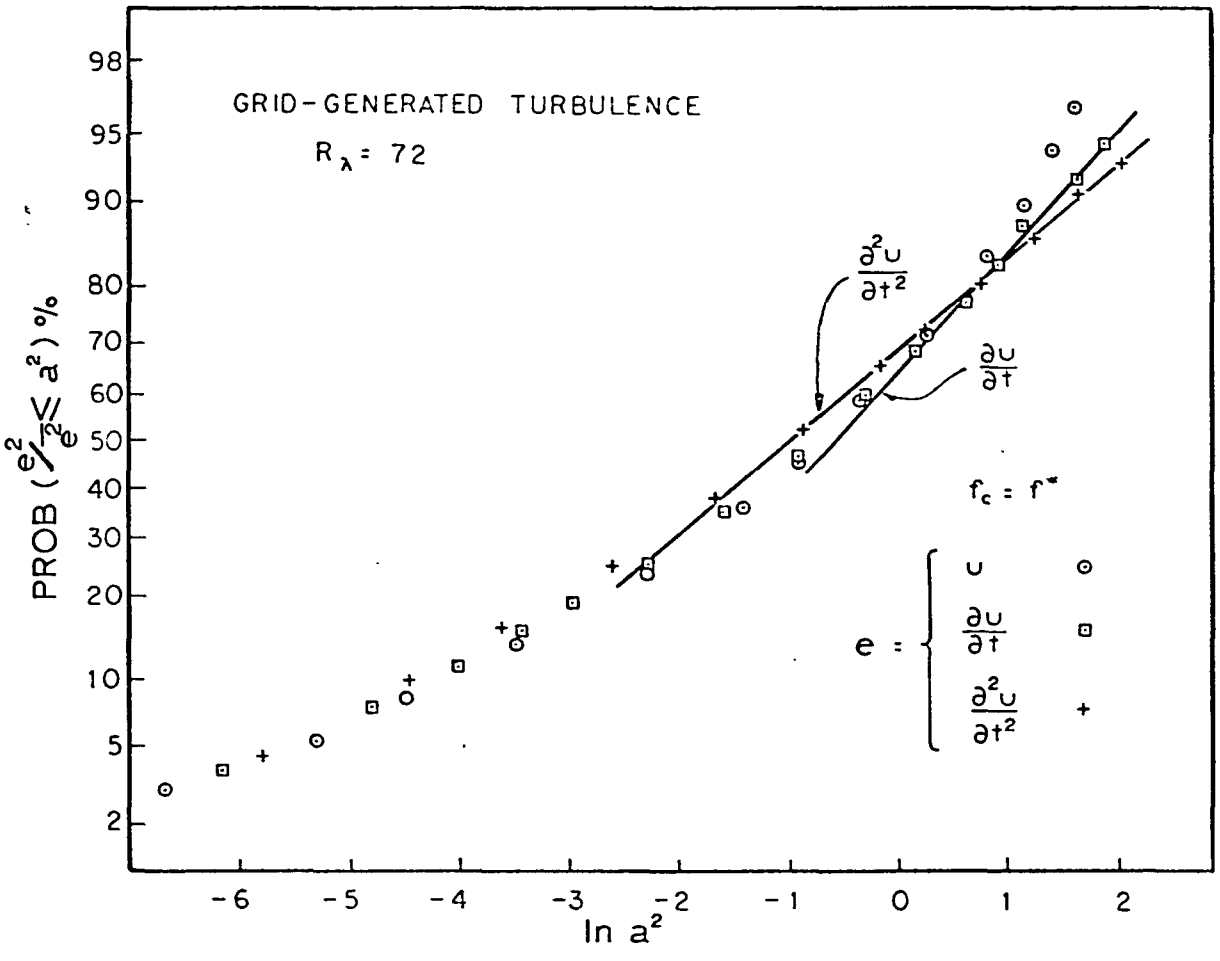

Figure 38. Probability Distributions of u^2, $(\partial u/\partial t)^2$, and $(\partial^2 u/\partial t^2)^2$ in a Grid-generated Turbulence, $R_\lambda = 72$ (straight lines correspond to Log-normal Distributions).

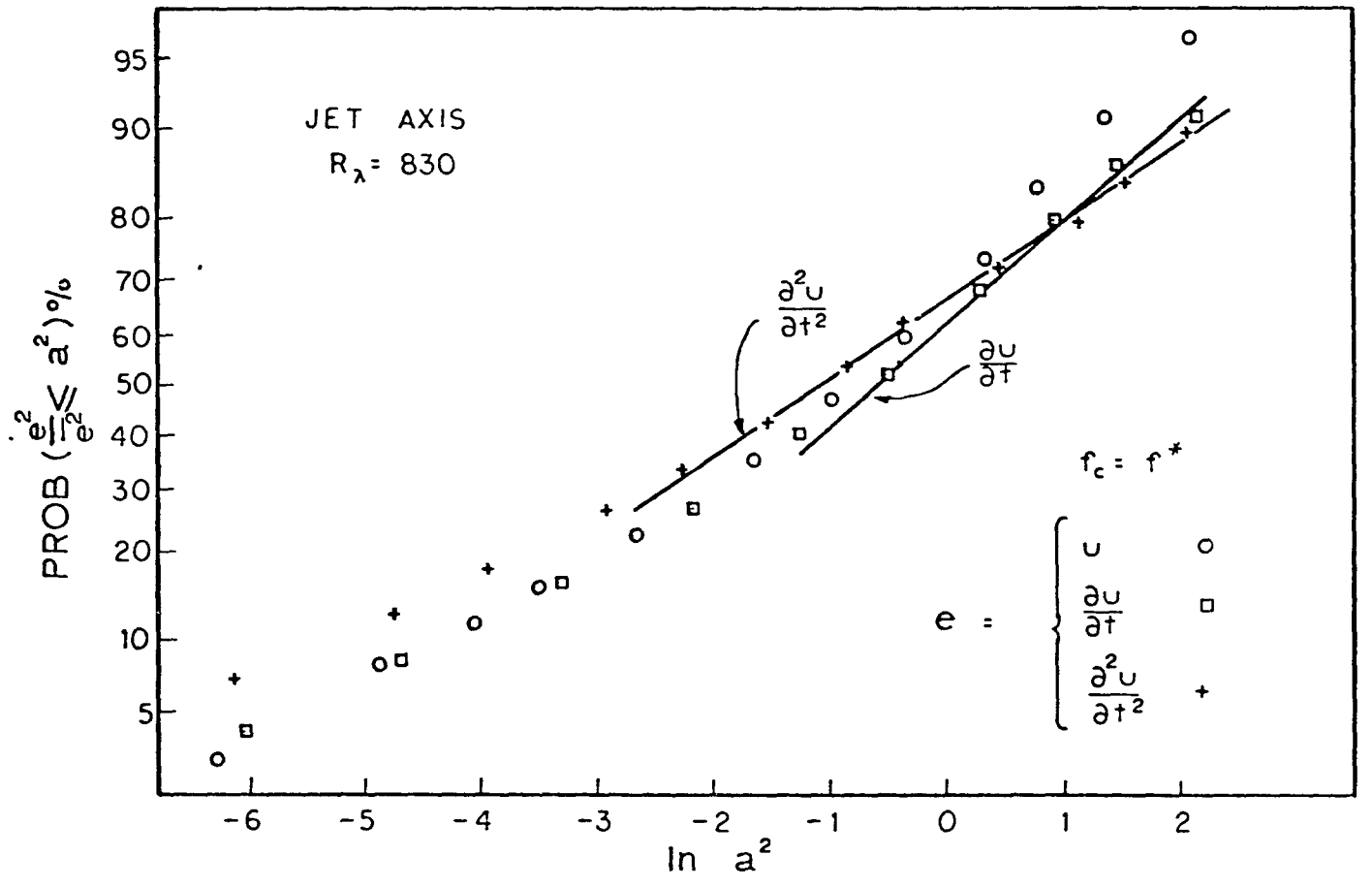

Figure 39. Probability Distributions of u^2, $(\partial u/\partial t)^2$, and $(\partial^2 u/\partial t^2)^2$ on the Axis of a Round Jet, R_λ = 830 (straight lines correspond to log-normal distributions).

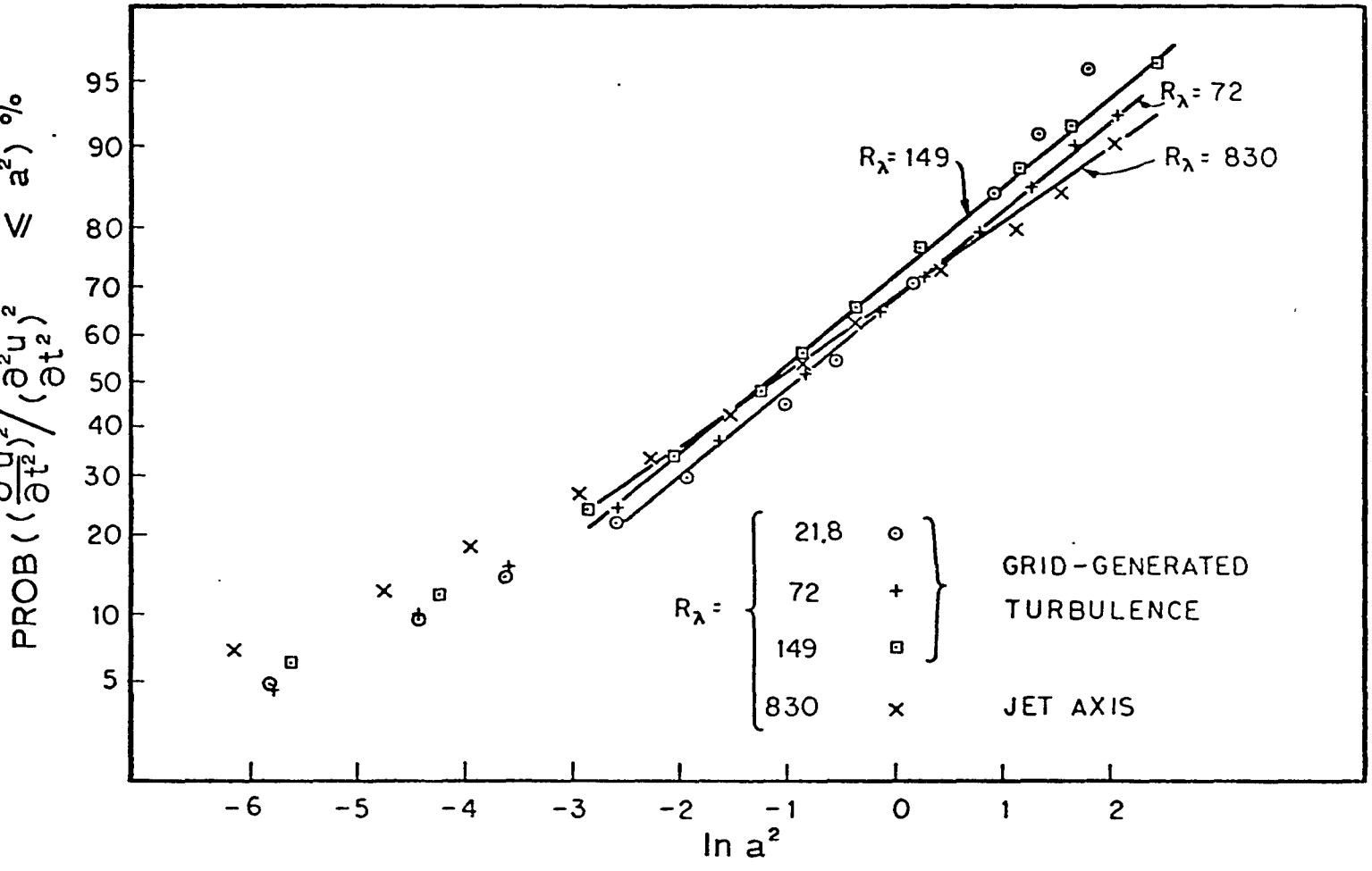

Figure 40. Probability Distributions of $\left(\partial^2 u/\partial t^2\right)^2$ at Various Reynolds Number.

(straight lines correspond to log-normal distributions)

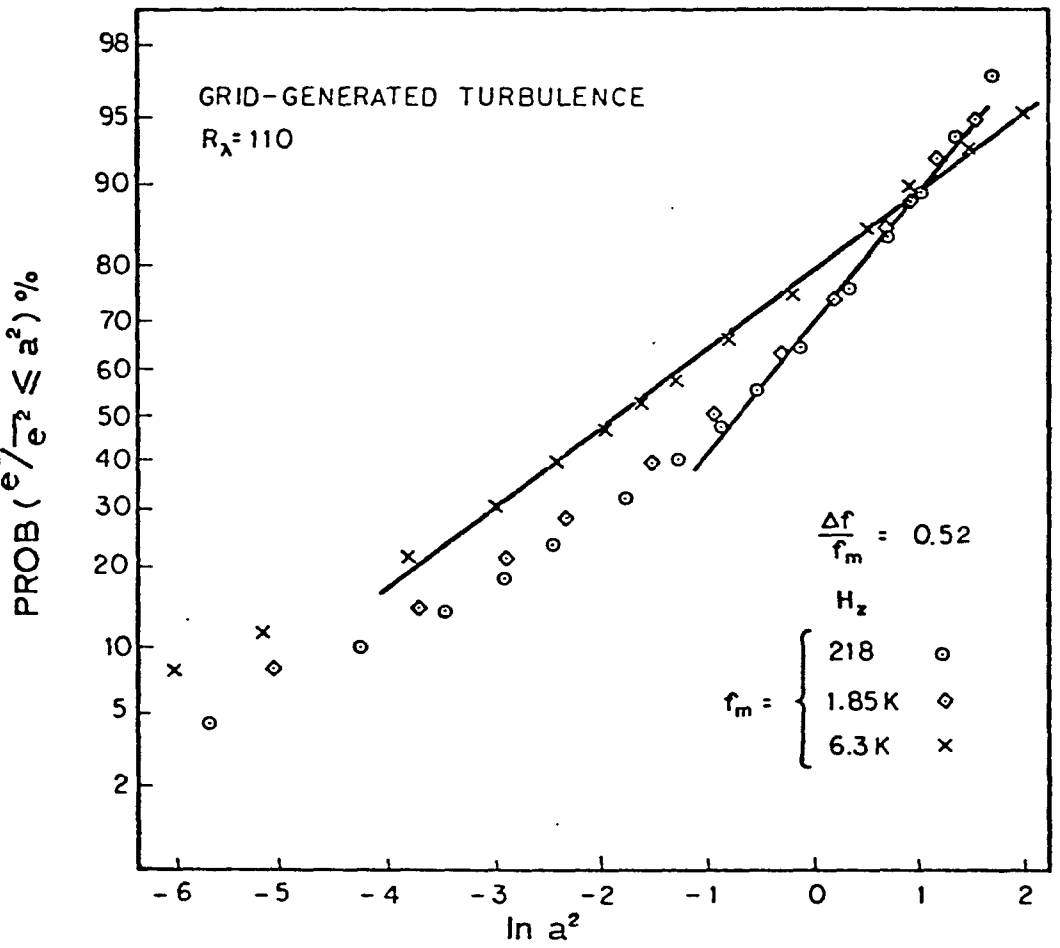

Figure 41. Probability Distributions of the Square of Band-pass Signal from a Grid-generated Turbulence, R_λ = 110.
(straight lines correspond to log-normal distributions)

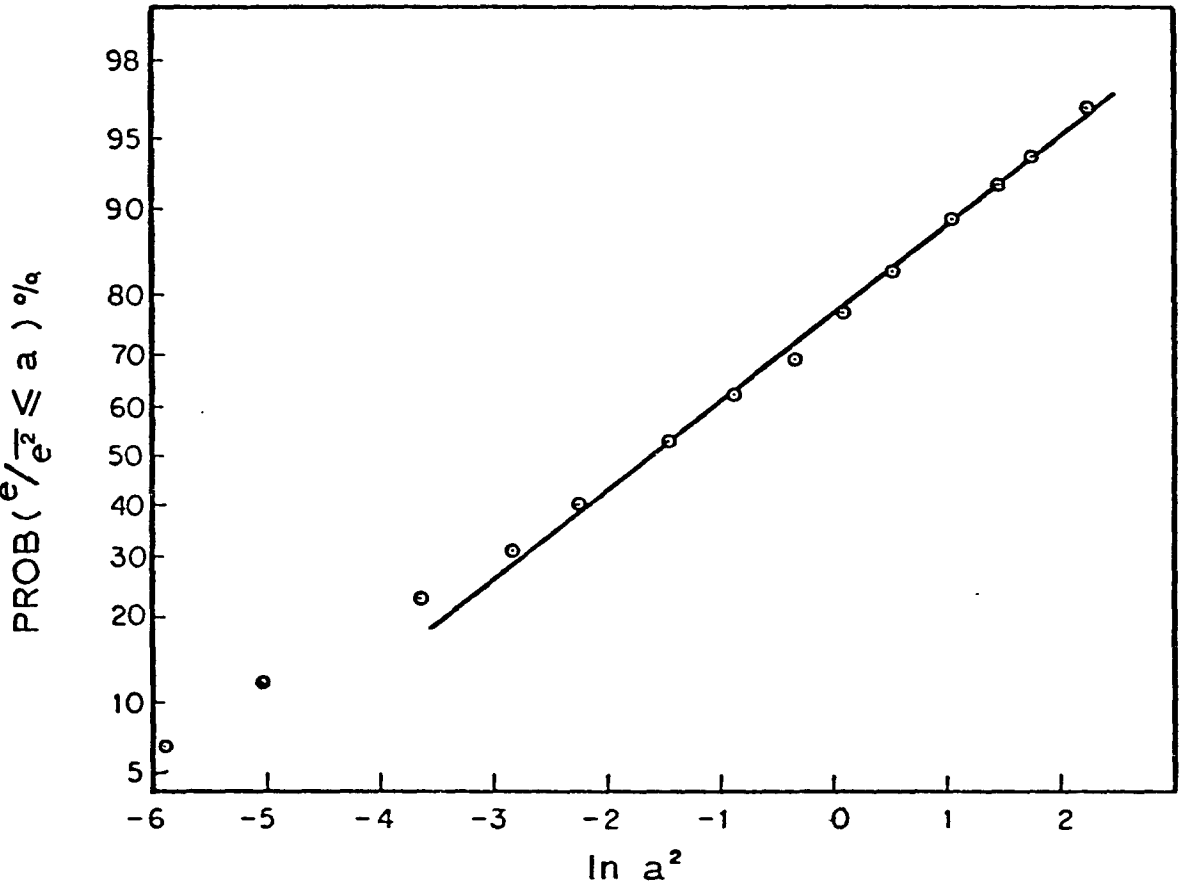

Figure 42. Probability Distribution of the Square of High-pass Signal from a Butterworth Filter, f_c = 5kHz. (straight lines correspond to log-normal distributions)

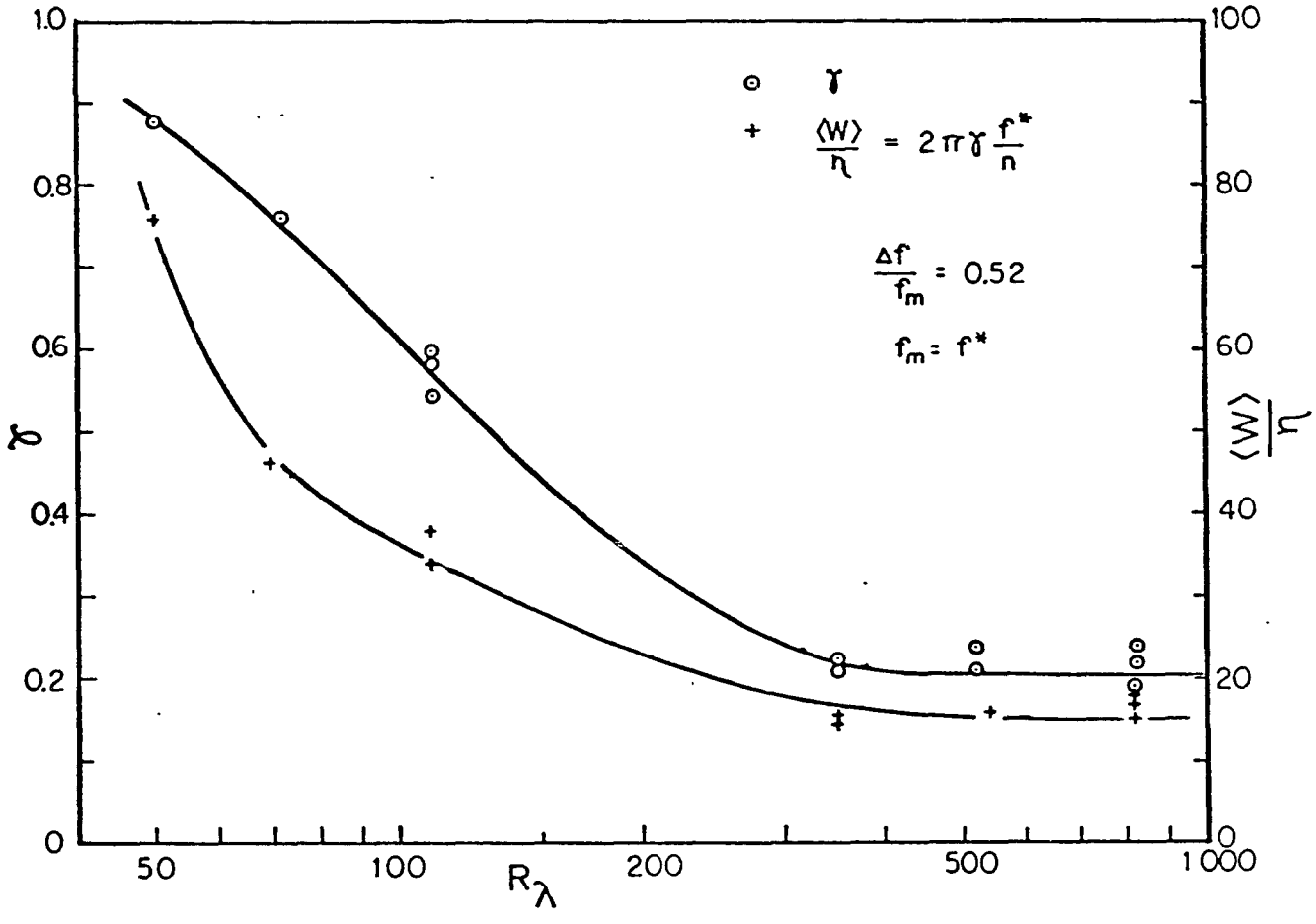

Figure 43. Intermittency Characteristics of Band-pass Signals as Functions of Reynolds Number, R_λ.

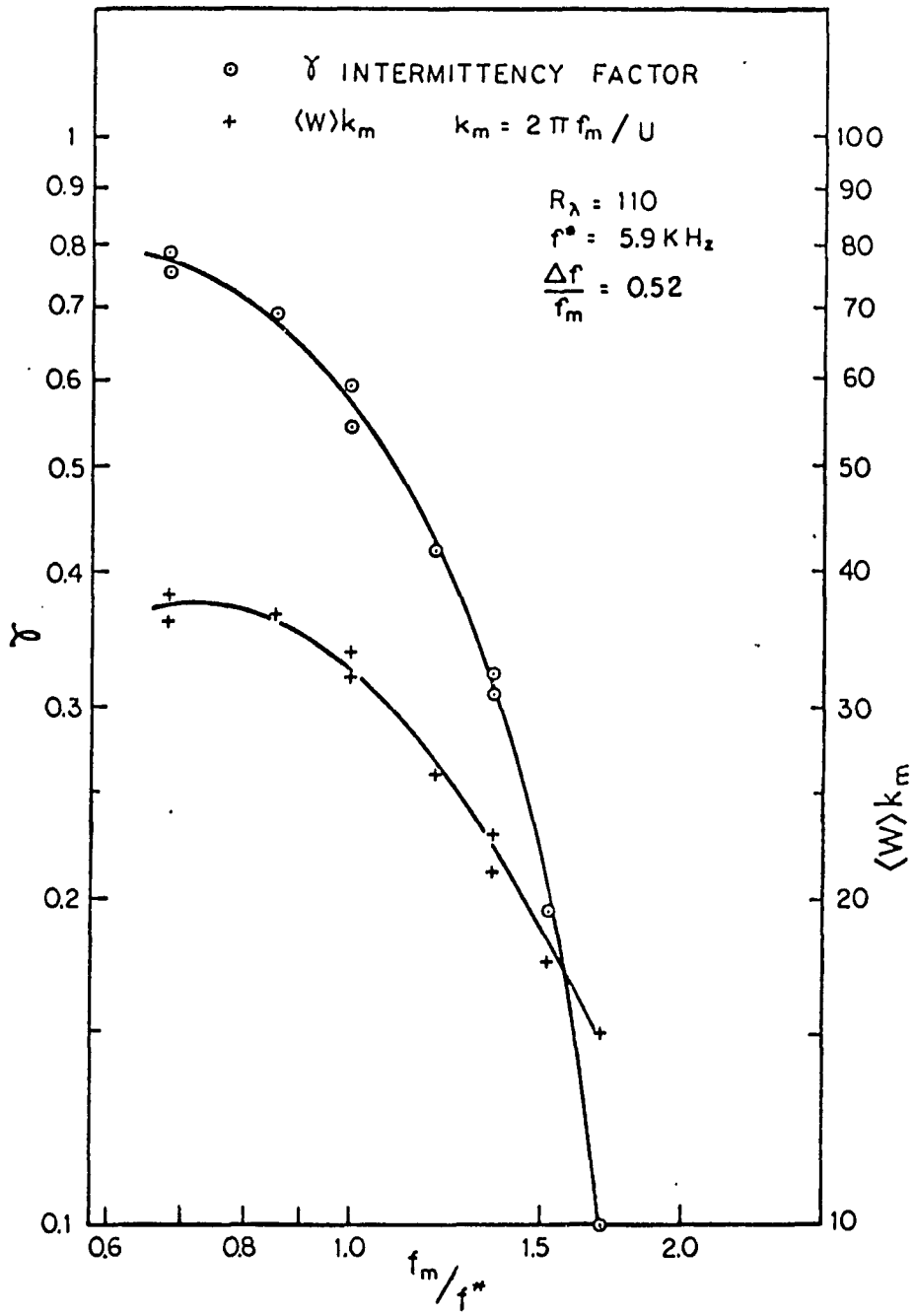

Figure 44(a). Intermittency Characteristics of Band-pass Signals as Functions of Midband Frequency f_m, in Log-log Scale, Grid-generated Turbulence, R_λ = 110.

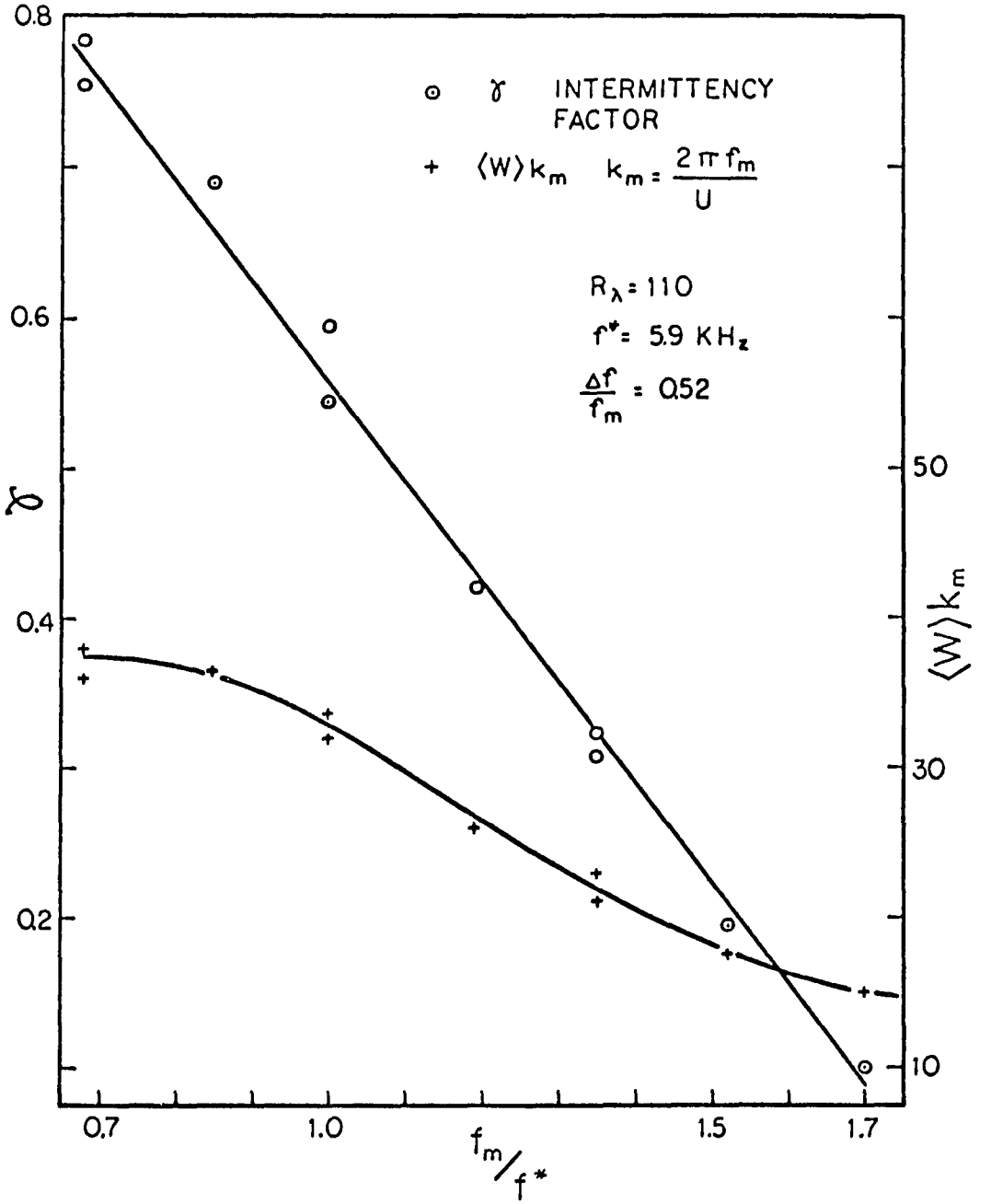

Figure 44(b). Intermittency Characteristics of Band-pass Signals as Functions of Midband Frequency f_m, in Linear Scale, Grid-generated Turbulence, $R_\lambda = 110$.

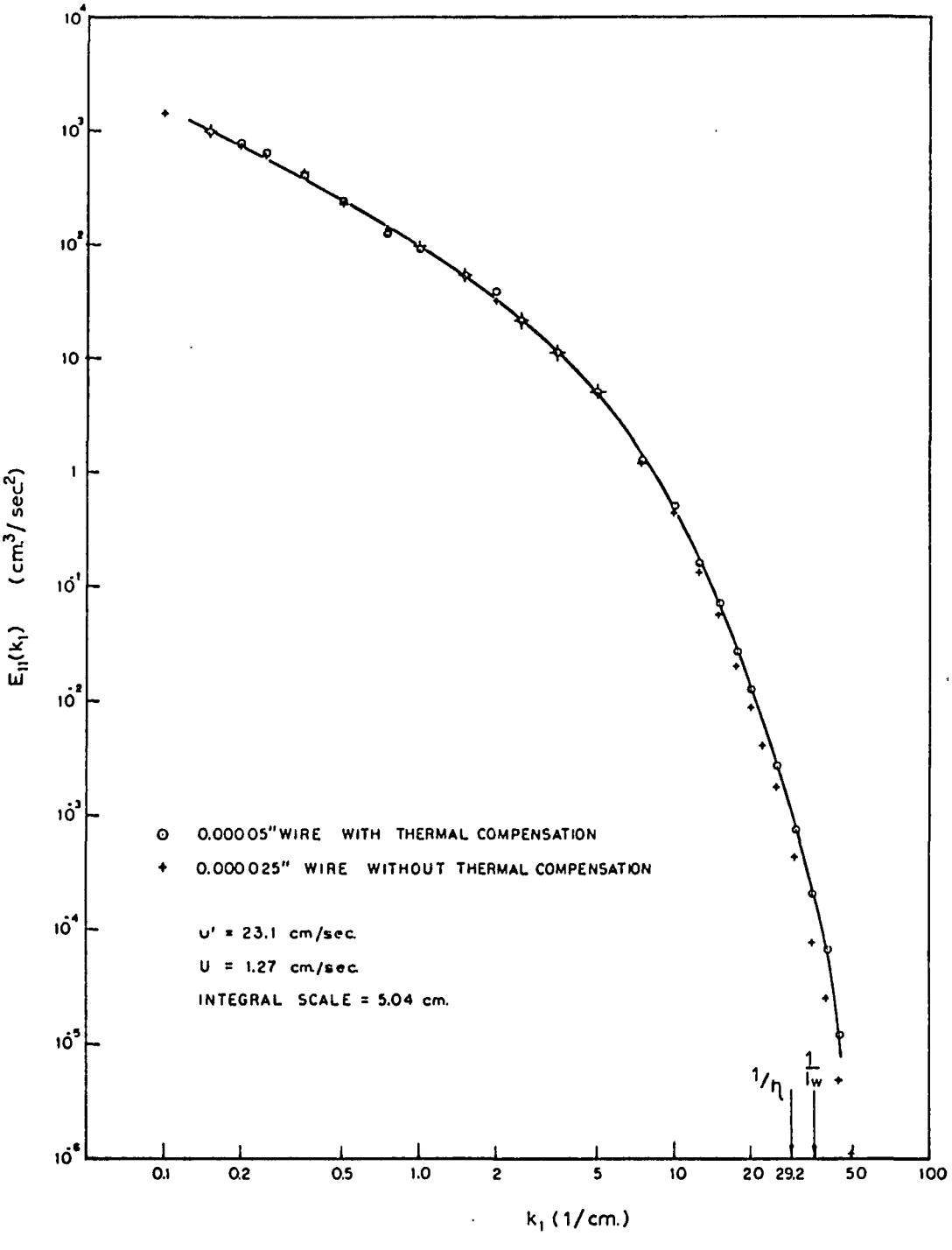

Figure 45. One-dimensional Energy Spectrum of a Grid-generated Turbulence, $R_\lambda = 110$.

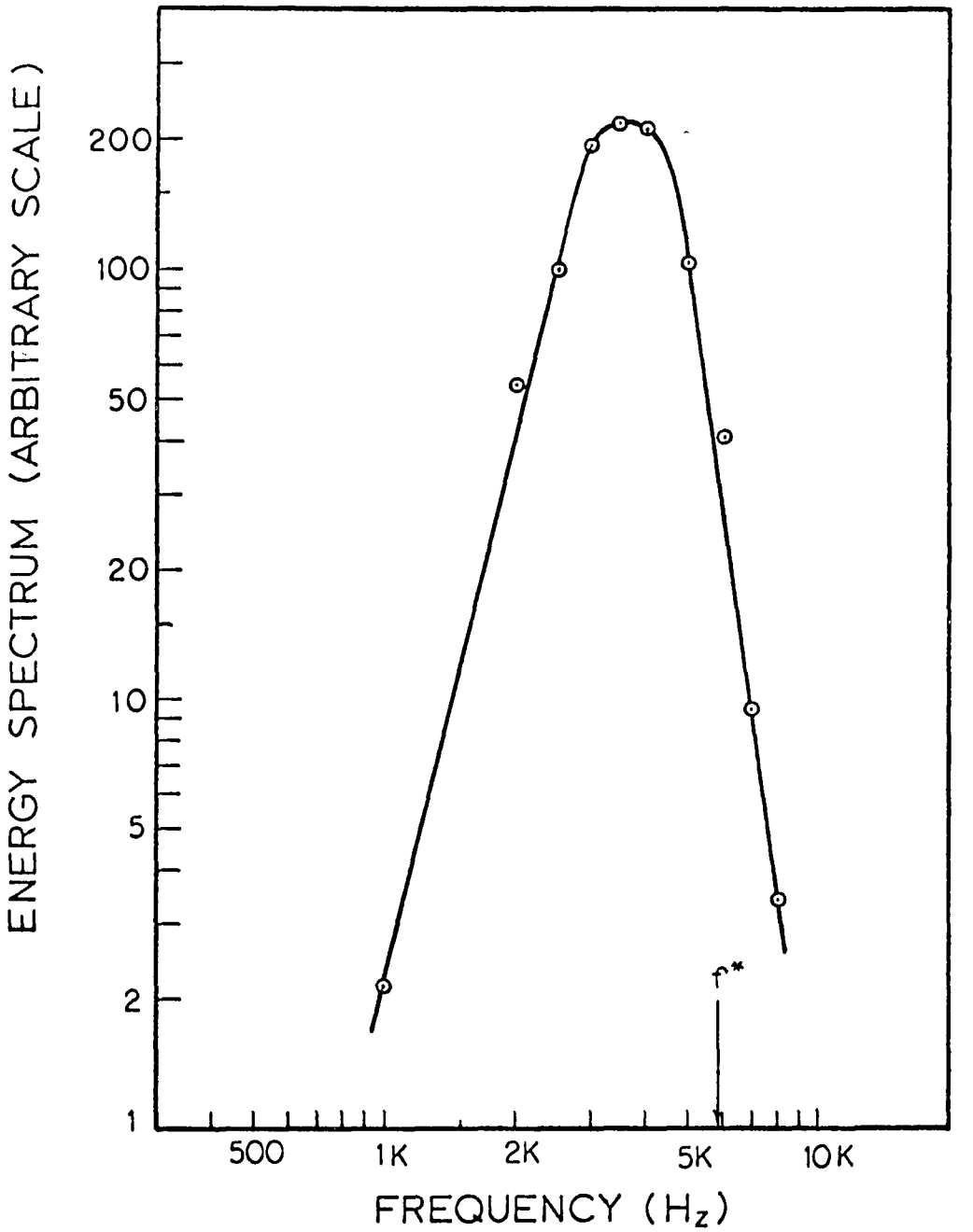

Figure 46. Energy Spectrum of the Signal from High-pass Butterworth Filter

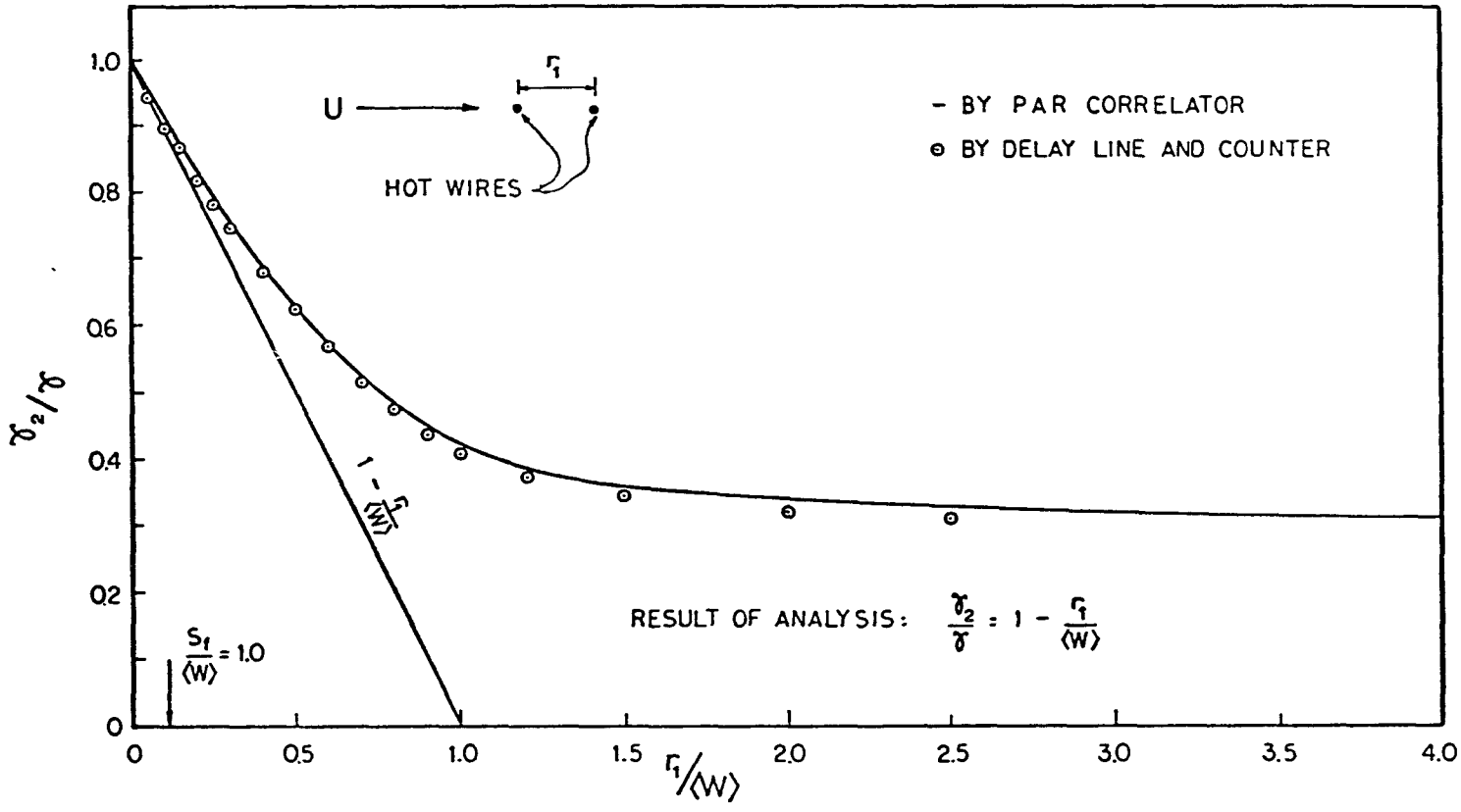

Figure 47. γ_2/γ AS A FUNCTION OF $r_1/\langle W \rangle$

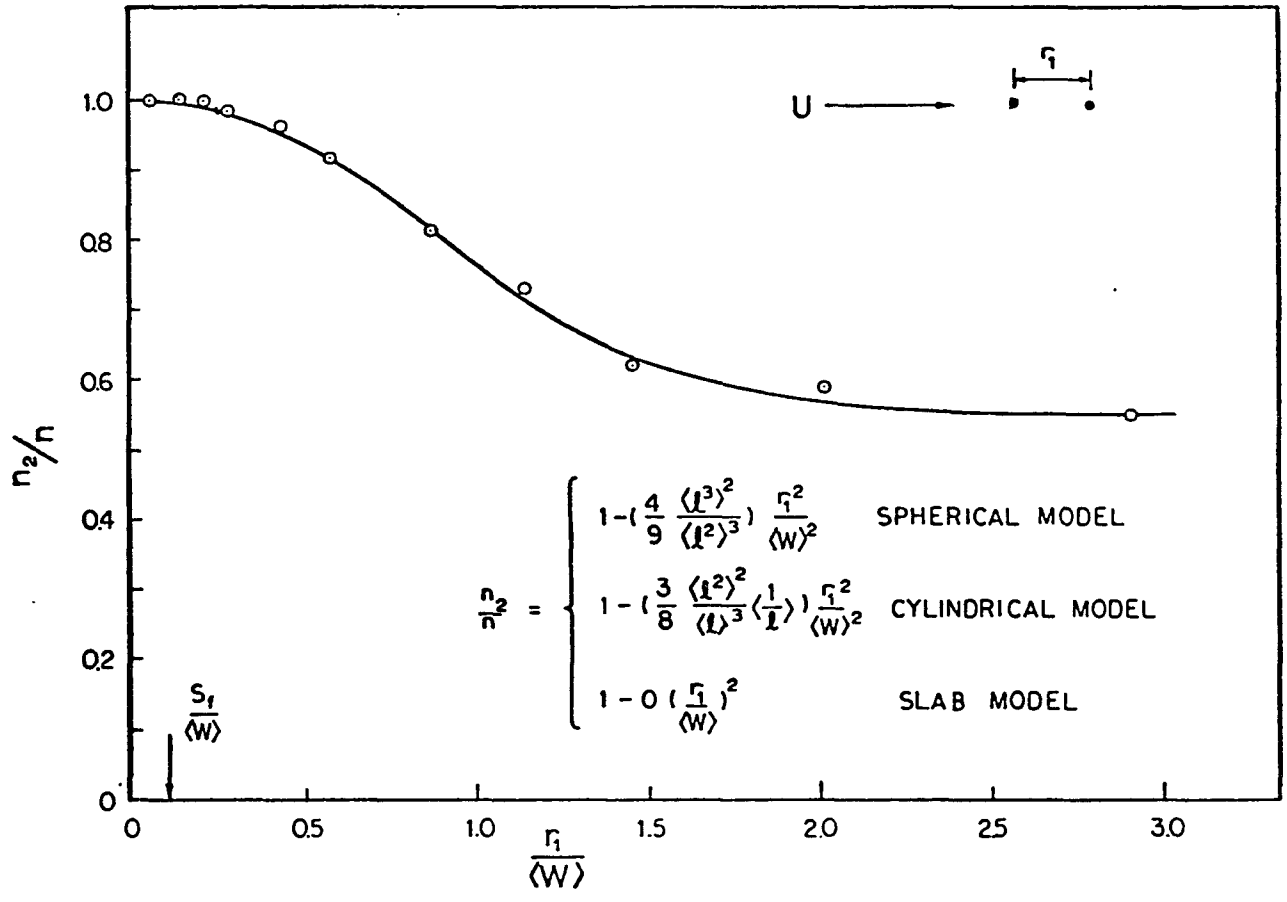

Figure 48. n_2/n AS A FUNCTION OF $r_1/\langle W\rangle$

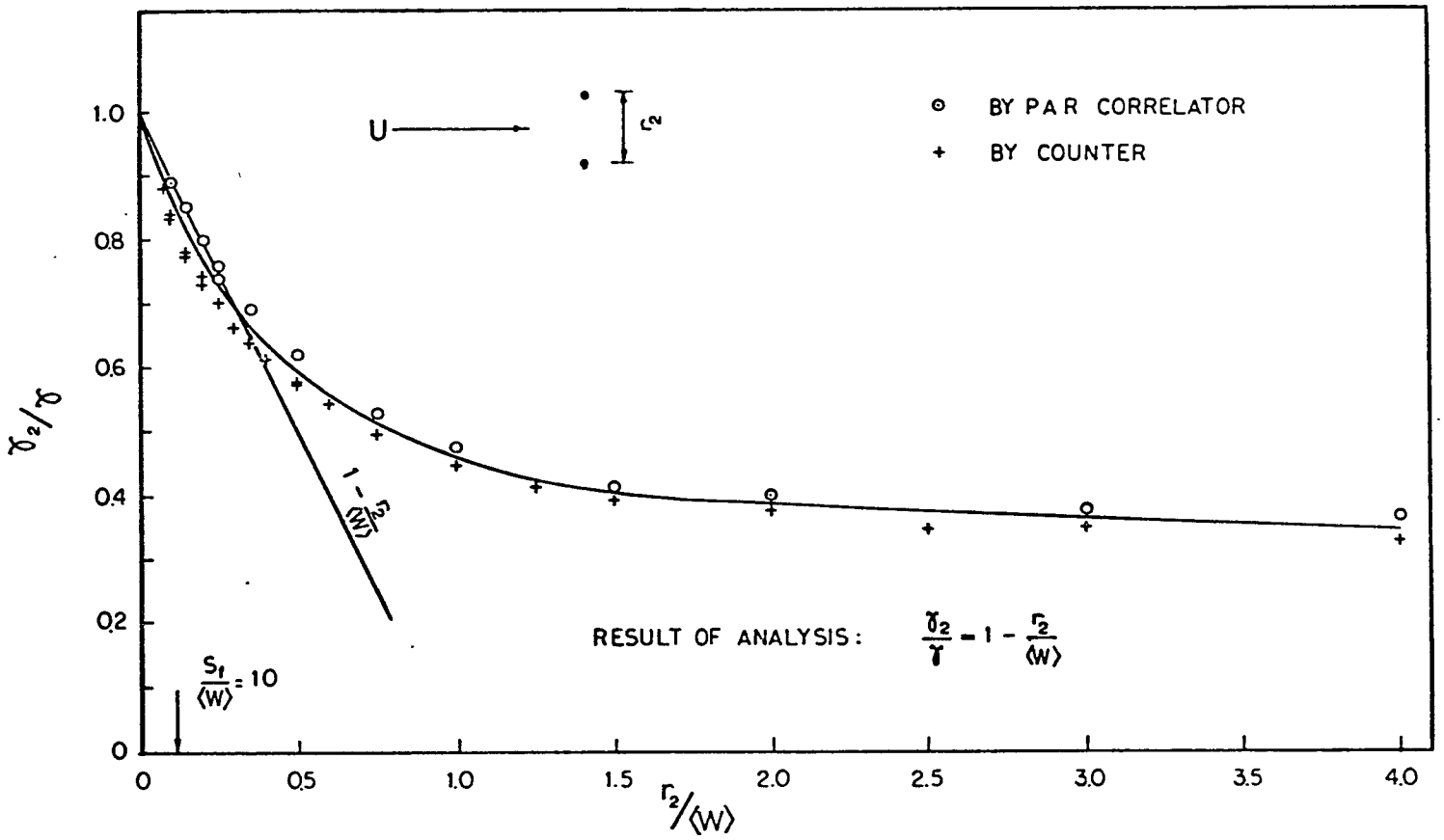

Figure 49. γ_2/γ AS A FUNCTION OF $r_2/\langle W \rangle$

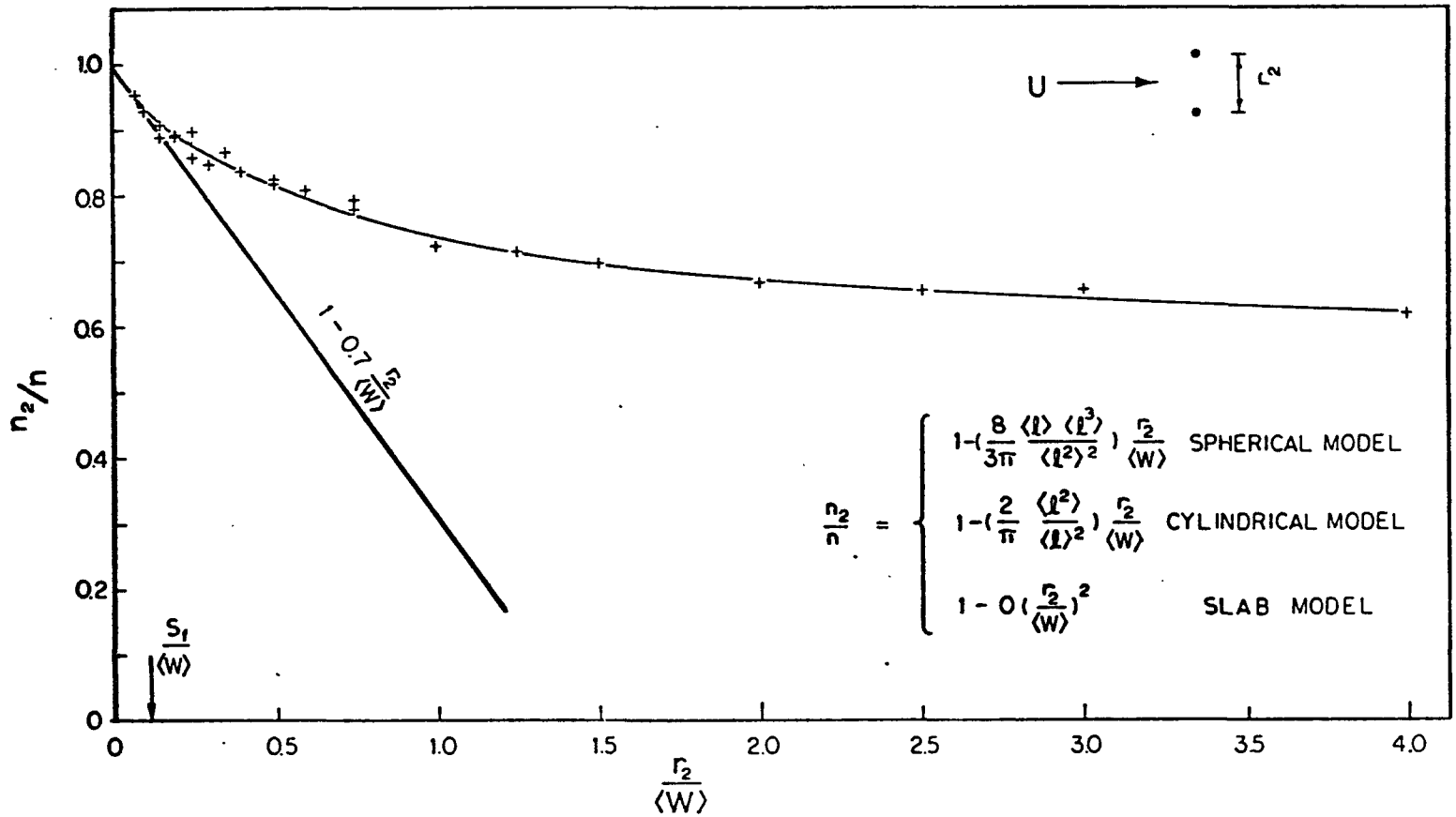

Figure 50. n_2/n AS A FUNCTION OF $r_2/\langle W\rangle$

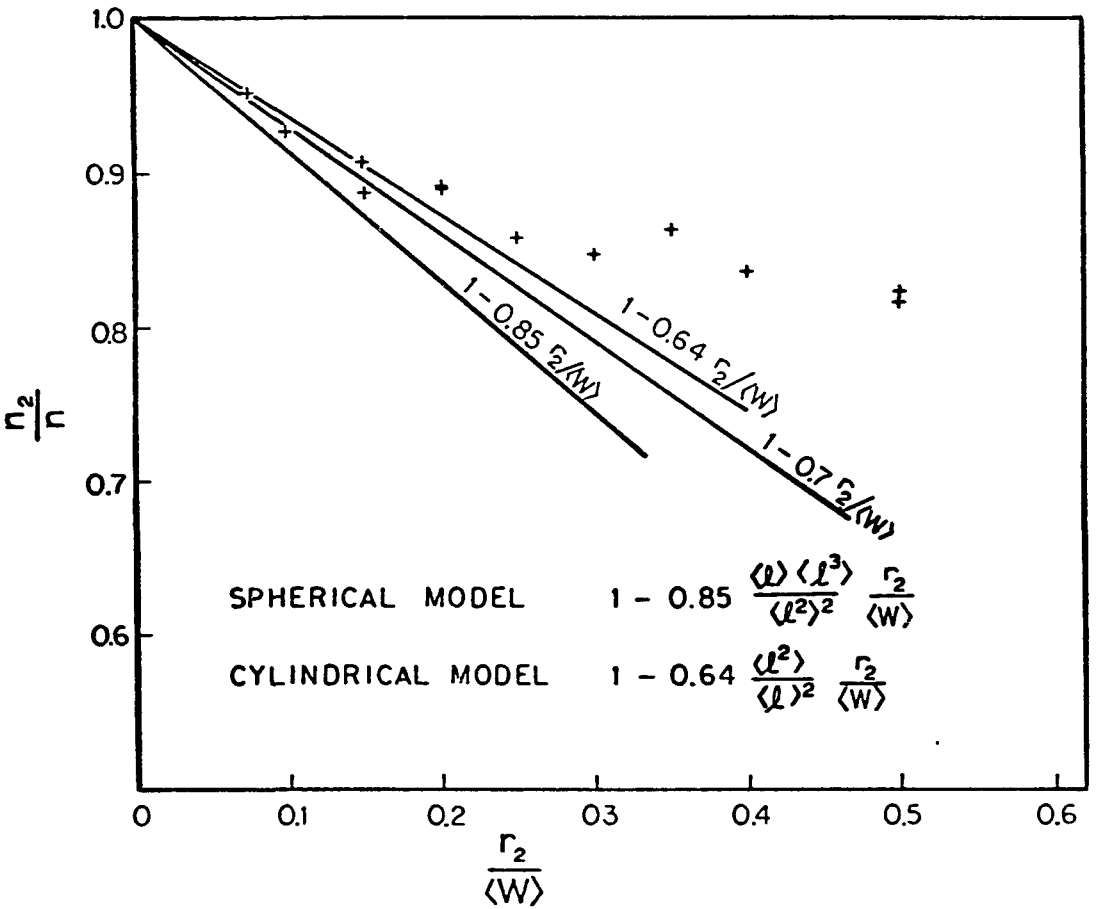

Figure 51. $\frac{n_2}{n}$ as a Function of $\frac{r_2}{\langle W\rangle}$, with amplified scale.

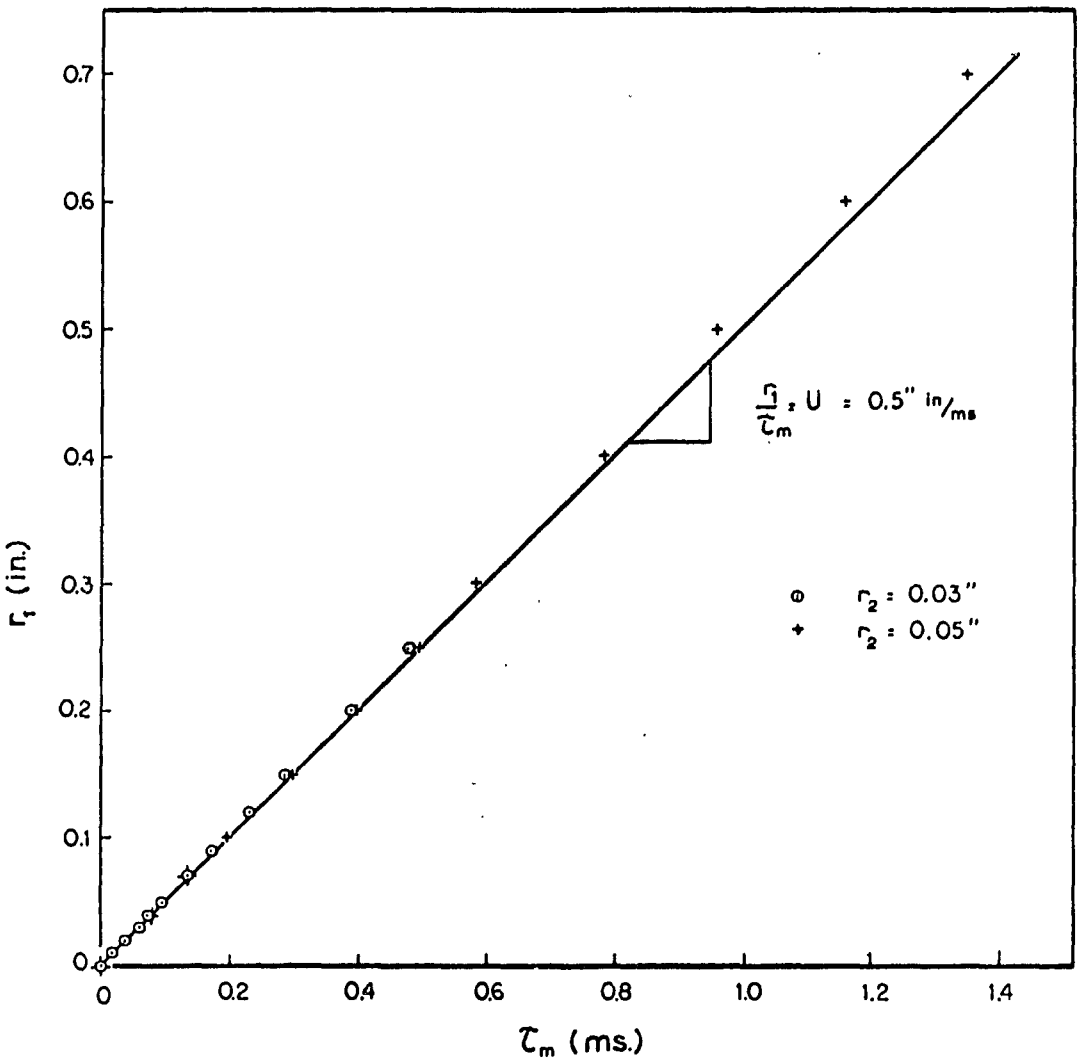

Figure 52. τ_m as Function of r_1 for Maximum $R_f(r_1, r_2, o, \tau)$.

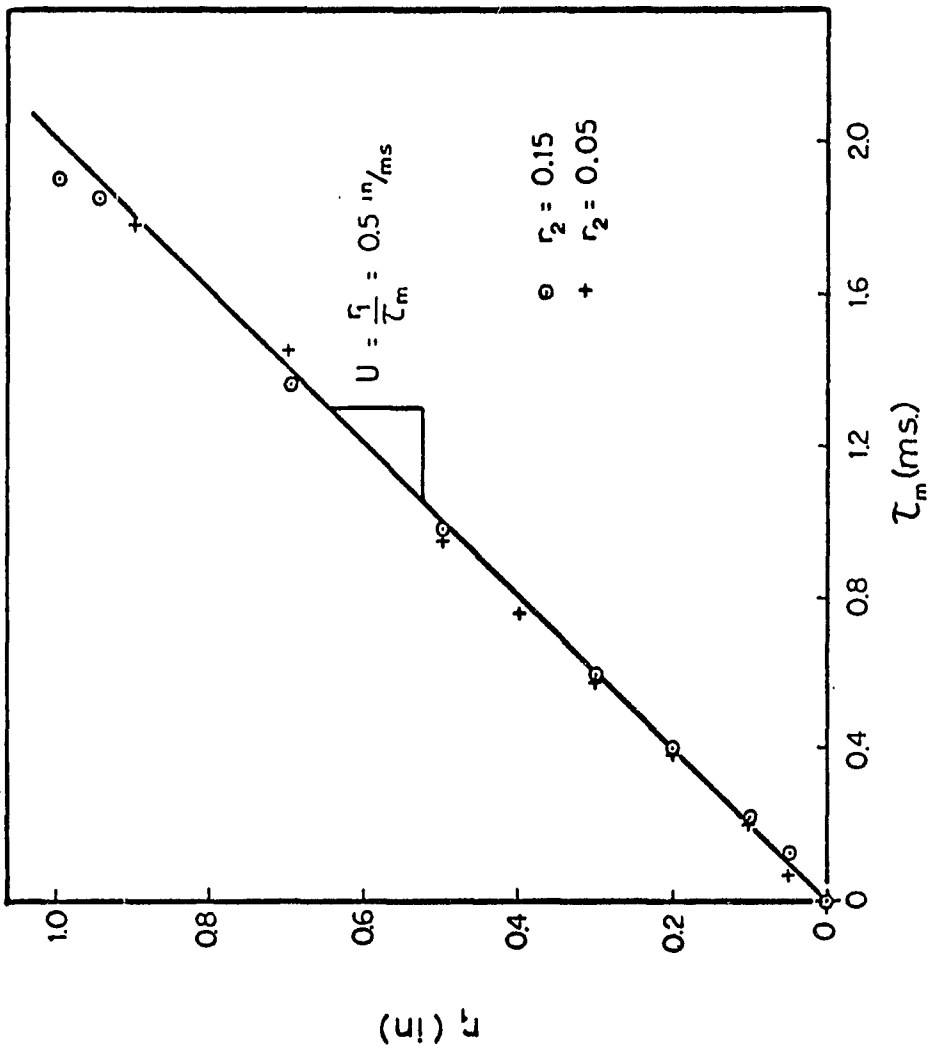

Figure 53. τ_m as Function of r_1 for Maximum $R_I(r_1, r_2, o, \tau)$.

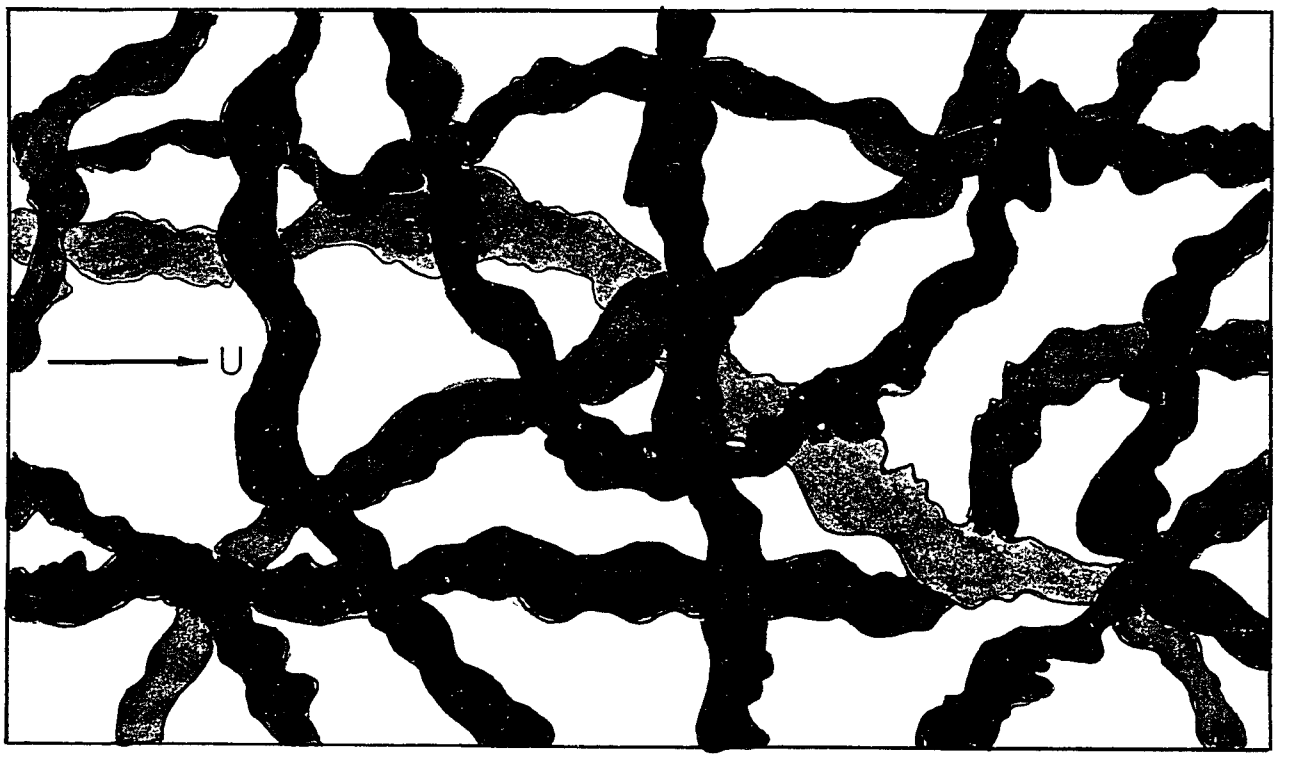

Figure 54. Qualitative Sketch of Fine-structure Regions

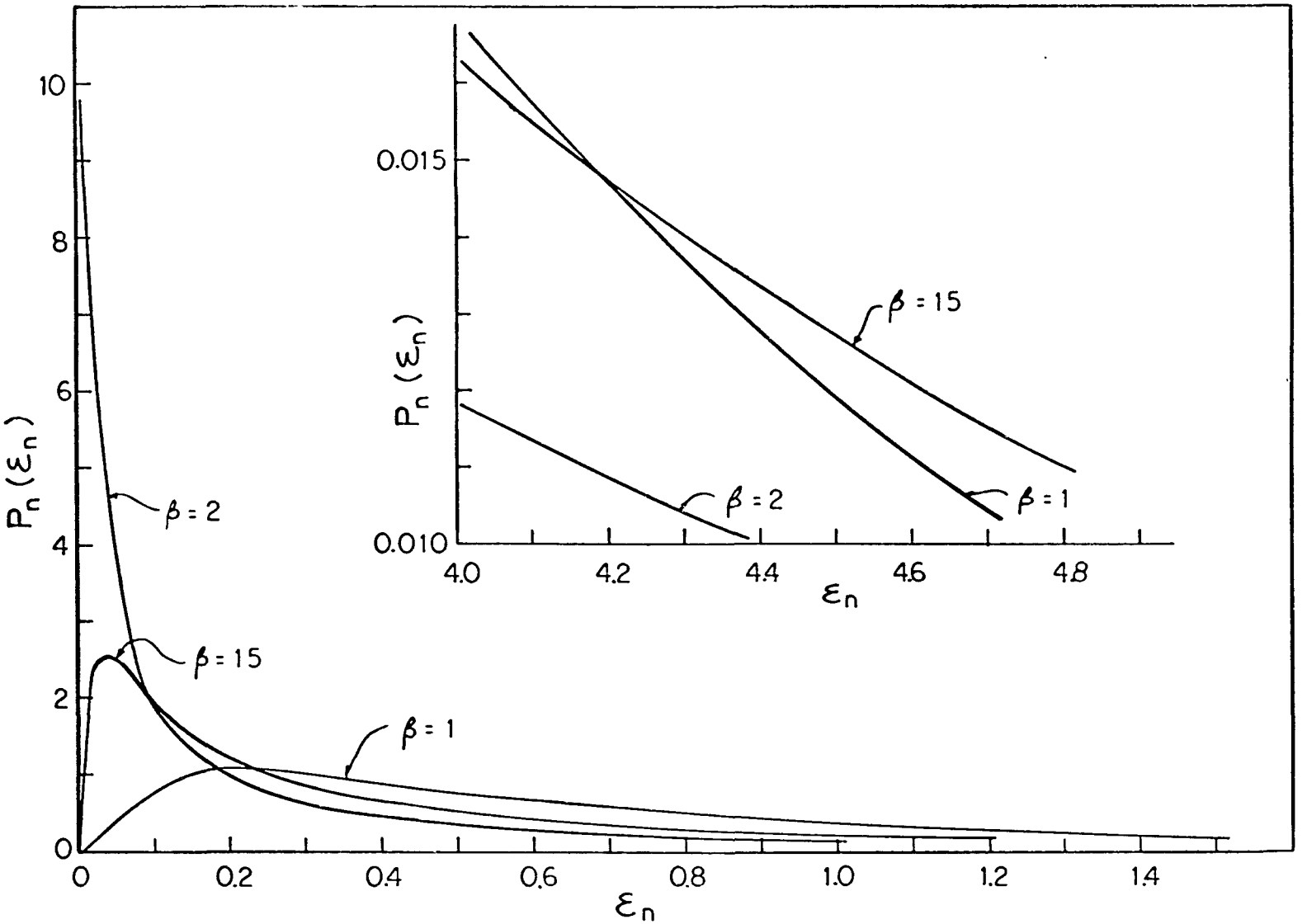

Figure 55. Log-normal Probability Density Curves

REFERENCES

1. Batchelor, G. K. and Townsend, A. A. "The Nature of Turbulent Motion at Large Wave-numbers." Proc. Roy. Soc., Ser. A, Vol. 199, p. 238, 1949.

2. Sandborn, V. A. "Measurements of Intermittency of Turbulent Motion in a Boundary Layer." J. Fluid Mech., Vol. 6, p. 221, 1959.

3. Kennedy, D. A. and Corrsin, S. "Spectra Flatness Factor and Intermittency in Turbulence and in Non-linear Noise." J. Fluid Mech., Vol. 10, p. 366, 1961.

4. Pond, S. and Stewart, R. W. "Measurements of the Statistical Characteristics of Small-scale Turbulent Motions." Izv., Acad. Sci. USSR, Atmo. and Oceanic Ser., Vol. 1, No. 9, P. 914, 1965.

5. Sheih, C. M. "Airborne Hot-wire Measurements of the Small-scale Structure of Atmospheric Turbulence." Ph.D. Thesis, The Penn. State Univ., 1969.

6. Stegn, G. R. and Gibson, C. H. "Lognormality of Turbulent Dissipation." Bull. of the Amer. Phy. Soc., p. 1101, Nov. 1969.

7. Townsend, A. A. "Local Isotropy in the Turbulent Wake of a Cylinder." Australian J. Sci. Res., Ser. A, Vol. 1, p. 161, 1948.

8. Kolmogorov, A. N. "The Local Structure of Turbulence in Incompressible Viscous Fluid for Very Large Reynolds Number." C. R. Acad. Sci. USSR, Vol. 30, p. 301, 1941.

9. Batchelor, G. K. "The Theory of Homogeneous Turbulence." Cambridge Univ. Press. Chap. 6, 1960.

10. Landau, L. D. and Lifshitz, E. "Fluid Mechanics." Addison-Wesley Pub. Co., p. 126, 1959.

11. Townsend, A. A. "On the Fine-scale Structure of Turbulence." Proc. Roy. Soc., Ser. A, Vol. 208, p. 534, 1951.

12. Batchelor, G. K. "Small-scale Variation of Convected Quantities Like Temperature in Turbulent Fluid." J. Fluid Mechanics, Vol. 5, p. 113, 1959.

13. Oboukhov, A. M. "Some Specific Features of Atmospheric Turbulence." J. Fluid Mech., Vol. 13, p. 77, 1962.

14. Kolmogorov, A. N." A Refinement of Previous Hypotheses Concerning the Local Structure of Turbulence in a Viscous Incompressible Fluid at High Reynolds Number." J. Fluid Mech., Vol. 13, p. 82, 1962.

15. Novikov, E. A. "Variation in the Dissipation of Energy in a Turbulent Flow and the Spectral Distribution of Energy." PMM, Vol. 27, No. 5, p. 944, 1963.

16. Nivokov, E. A. and Stewart, R. W." The Intermittency of Turbulence and the Spectrum of Energy Dissipation Fluctuations." Izv., Acad. Sci. USSR, Geophys. Ser. No. 3, p. 408, 1964.

17. Yaglom, A. M. "The Influence of Fluctuations in Energy Dissipation on the Shape of Turbulence Characteristics in the Inertial Interval." Soviet Physics - Doklady, Vol. 11, No. 1, p. 26, 1966.

18. Gurvich, A. S. and Zubkovskii, S. L. "On the Experimental Evaluation of the Fluctuations of Dissipation of Turbulent Energy." Izv., Acad. Sci. USSR, Geophys. Ser., No. 12, p. 1856, 1963.

19. Gurvich, A. S. and Yaglom, A. M. "Breakdown of Eddies and Probability Distributions for Small-scale Turbulence." The Physics of Fluids, Supplement, p. 59, 1967.

20. Corrsin, S. "Turbulent Dissipation Fluctuations." The Physics of Fluids, Vol. 5, No. 10, p. 1301, 1962.

21. Tennekes, H. "Simple Model for the Small-scale Structure of Turbulence." The Physics of Fluids, Vol. 11, No. 3, p. 669, 1968.

22. Bennett, J. C. "Decay of Isotropic Turbulence at Small Reynolds Numbers." Ph.D. Thesis, The Johns Hopkins University, 1970.

23. Comte-Bellot, G. and Corrsin, S. "The Use of a Contraction to Improve the Isotropy of Grid-generated Turbulence." J. Fluid Mech., Vol. 25, p. 657, 1966.

24. Gibson, M. M. "Spectra of Turbulence in a Round Jet." J. Fluid Mech., Vol. 15, p. 161, 1963.

25. Champagne, F. H., Harris, V. G. and Corrsin, S. "Experiments on Nearly Homogeneous Turbulent Shear Flow." J. Fluid Mech., Vol. 41, p. 81 , 1970.

26. Liepmann, H. W. "Aspects of the Turbulence Problem." J. of Appl. Math. and Phy., Vol. 3, p. 321, 1952.

27. Townsend, A. A. "The Fully Developed Turbulent Wake of a Circular Cylinder." Australian J. Sci. Res., Ser. A, Vol. 2, p. 451, 1949.

28. Kohan, S. M. "Some Studies in the Wall Region and the Intermittent Region of the Plane Two-dimensional Wall Jet." Ph.D. Thesis, Stanford Univ., 1969.

29. Philbrick Research, Inc. "Applications Manual for Computing Amplifiers." p. 59, 1968.

30. Batchelor, G. K. and Townsend, A. A. "Turbulent Diffusion." Survey in Mechanics, edited by G. K. Batchelor and R. M. Davies, Cambridge Univ. Press, p. 352, 1956.

31. Townsend, A. A. "The Diffusion of Heat Spots in Isotropic Turbulence." Proc. Roy. Soc., Ser. A, Vol. 209, p. 418, 1951.

32. Corrsin, S. "A Measure of the Area of a Homogeneous Random Surface in Space." Quart. of Appl. Math., p. 404, January 1955.

33. Corrsin, S. and Phillips, O. M. "Contour Length and Surface Area of Multiple-Valued Random Variables." J. Soc. Indust. Appl. Math., Vol. 9, No. 3, p. 395, 1961.

34. Pawula, R. F. "A Proof of Corrsin's Theorem Concerning Stationary Random Surfaces." IEEE Trans. on Information Theory, p. 770, Sept. 1968.

35. Grant, H. L., Stewart, R. W., Moilliet, A. "Turbulent Spectra from a Tidal Channel." J. Fluid Mech., Vol. 12, p. 241, 1962.

37. Taylor, G. I. "The Spectrum of Turbulence." Proc. Roy. Soc. of London, Ser. A, Vol. 164, p. 476, 1938.

38. Favre, A. J., Gaviglio, J. J., and Dumas, R. "Space-Time Double Correlations and Spectra in a Turbulent Boundary Layer." J. Fluid Mech., Vol. 2, p. 313, 1957.

39. Lin, C. C. "On Taylor's Hypothesis and the Acceleration Terms in the Navier-Stokes Equations." Quart. Appl. Math., Vol. 10, p. 295, 1953.

40. Fisher, M. J. and Davies, P. O. A. L. "Correlation Measurements in a Non-frozen Pattern of Turbulence." J. Fluid Mech., Vol. 18, p. 97, 1964.

41. Lumley, J. L. "Interpretation of Time Spectra Measured in High-Intensity Shear Flow." The Physics of Fluids, Vol. 8, No. 6, p. 1056, 1965.

42. Stewart, R. W., Wilson, J. R., and Burling, R. W. Paper presented at the Boeing Symposium on Turbulence, June 1969; also J. Fluid Mech., to be published.

43. Stewart, R. W., Wilson, J. R. and Burling, R. W. "Some Statistical Properties of Small-scale Turbulence in an Atmospheric Boundary Layer." J. Fluid Mech., Vol. 41, p. 141, 1970.

44. Gibson, C. H., Stegen, G. R., and Williams, R. B. "Statistics of the Fine Structure of Turbulent Velocity and Temperature Fields Measured at High Reynolds Number." J. Fluid Mechanics, Vol. 41, p. 153, 1970.

VITA

Albert Yi-shuong Kuo

Date of Birth: November 4, 1939

Place of Birth: Tayuan, Taiwan

Education: Primary education in Tayuan, a small village. In September, 1952, entered Provincial Chen-Kuo High School in Taipei, Taiwan. Enrolled in the National Taiwan University in September, 1958, received B.S. in Agricultural Engineering, June, 1962. Came to the United States in September, 1963 and studied hydraulics at the University of Iowa. Received the M.S. degree, January, 1965. September, 1964 to the present: Department of Mechanics, The Johns Hopkins University.

Experience: Served in Chinese Army as a psy-war officer from September, 1962 to August, 1963. Worked as a research assistant in the University of Iowa and The Johns Hopkins University from 1963 to present. Served as a Junior Instructor in Fluid Mechanics from November, 1967 to May, 1969 in the Department of Mechanics, The Johns Hopkins University.